



HAL
open science

Optimization of Drug-Eluting Stents

Franz Bozsak

► **To cite this version:**

Franz Bozsak. Optimization of Drug-Eluting Stents. Cardiology and cardiovascular system. Ecole Polytechnique X, 2013. English. NNT: . pastel-00858100

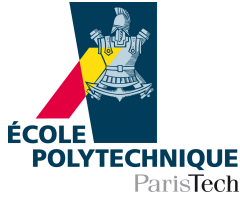
HAL Id: pastel-00858100

<https://pastel.hal.science/pastel-00858100>

Submitted on 4 Sep 2013

HAL is a multi-disciplinary open access archive for the deposit and dissemination of scientific research documents, whether they are published or not. The documents may come from teaching and research institutions in France or abroad, or from public or private research centers.

L'archive ouverte pluridisciplinaire **HAL**, est destinée au dépôt et à la diffusion de documents scientifiques de niveau recherche, publiés ou non, émanant des établissements d'enseignement et de recherche français ou étrangers, des laboratoires publics ou privés.



École Polytechnique
Laboratoire d'Hydrodynamique

Thèse présentée pour obtenir le grade de
DOCTEUR DE L'ÉCOLE POLYTECHNIQUE

Spécialité : Mécanique

par

Franz BOZSAK

Optimization of Drug-Eluting Stents*

*Optimisation de stents actifs

Thèse soutenue le 03 juin 2013 devant le jury composé de

Gabriele Dubini
James E. Moore, Jr.
Alexander I. J. Forrester
Antoine Lafont
Abdul I. Barakat
Jean-Marc Chomaz

rapporteur
rapporteur
examineur
examineur
directeur de thèse
directeur de thèse

Politecnico di Milano
Imperial College London
University of Southampton
INSERM, HEGP
CNRS, École Polytechnique
CNRS, École Polytechnique

Optimization of Drug-Eluting Stents

Franz Bozsak

Advisors:

Abdul I. Barakat

Jean-Marc Chomaz

Optimization of Drug-Eluting Stents

Laboratoire d'Hydrodynamique (LadHyX)
École Polytechnique, France

For my Princess

Contents

| | |
|--|-------------|
| Contents | v |
| Abstract | ix |
| Résumé | ix |
| Acknowledgments | xi |
| List of Figures | xiii |
| List of Tables | xv |
| Nomenclature | xvii |
| 1 Introduction | 1 |
| 1.1 Atherosclerosis: a human condition? | 1 |
| 1.2 Treatment of atherosclerosis: a brief history | 3 |
| 1.3 Anti-proliferative drugs: bliss and curse of drug-eluting stent design | 4 |
| 1.4 Modeling drug transport in the arterial wall | 5 |
| 1.5 Stent design optimization | 5 |
| 1.6 Scope and outline of the present dissertation | 6 |
| 2 Modeling the Transport of Drugs Eluted from Stents | 9 |
| 2.1 Introduction | 9 |
| 2.2 Materials and methods | 10 |
| 2.2.1 Model geometry | 10 |
| 2.2.2 Physical model | 10 |
| 2.2.3 Governing equations and boundary conditions | 11 |
| 2.2.4 Determination of physiological parameters | 15 |
| 2.2.5 Numerical methods | 20 |
| 2.3 Results | 21 |
| 2.3.1 Baseline model | 21 |
| 2.3.2 Sensitivity analysis of the model | 22 |
| 2.3.3 Effect of one-layer modeling | 25 |
| 2.3.4 Effect of reaction modeling | 26 |
| 2.3.5 Effect of the choice of drug | 27 |
| 2.4 Discussion | 30 |

| | | |
|----------|--|-----------|
| 2.4.1 | Drug release is coupled to the drug and its transport properties in the arterial wall | 30 |
| 2.4.2 | Multi-layer model offers improved accuracy for pathological situations | 31 |
| 2.4.3 | Reduction of the reaction model fails to capture important features of the transport dynamics | 32 |
| 3 | Optimized Drug Delivery for Drug-Eluting Stents | 33 |
| 3.1 | Introduction | 33 |
| 3.2 | Materials and methods | 35 |
| 3.2.1 | Computational model | 35 |
| 3.2.2 | Cost function | 35 |
| 3.2.3 | Optimization framework | 41 |
| 3.2.4 | Optimization cases | 42 |
| 3.3 | Results | 42 |
| 3.3.1 | Paclitaxel delivery optimization | 42 |
| 3.3.2 | Sirolimus delivery optimization | 47 |
| 3.4 | Discussion | 51 |
| 3.4.1 | Paclitaxel-eluting stents require quasi-bolus or zero-order drug release kinetics to avoid adverse concentration levels at the endothelium | 51 |
| 3.4.2 | Sirolimus-eluting stents require zero-order release kinetics due to sirolimus' weak retention capabilities | 52 |
| 3.4.3 | Low-dose P-DES and S-DES with zero-order release kinetics lead to a similar shape of the cost function | 53 |
| 3.4.4 | The cost function responds to drug kinetics in the arterial wall | 53 |
| 3.4.5 | Paclitaxel vs. sirolimus: a settled debate? | 53 |
| 4 | Optimizing the Strut Design of Paclitaxel- and Sirolimus-Eluting Stents | 55 |
| 4.1 | Introduction | 55 |
| 4.2 | Materials and methods | 57 |
| 4.2.1 | Computational model | 57 |
| 4.2.2 | Cost function | 58 |
| 4.2.3 | Optimization method | 59 |
| 4.2.4 | Sensitivity estimation of the cost function to design variables and model parameters | 69 |
| 4.3 | Results | 71 |
| 4.3.1 | Sensitivity estimation of the cost function | 71 |
| 4.3.2 | Optimization results | 74 |
| 4.4 | Discussion | 84 |
| 4.4.1 | Optimal DES strut designs are tailored to optimized transport dynamics in the arterial wall | 85 |
| 4.4.2 | Optimal two-layered DES polymer coatings are tailored to the eluted drug | 87 |
| 4.4.3 | Challenges of the FDI weight factor | 88 |
| 5 | Conclusions | 91 |
| 5.1 | Future work | 92 |
| 5.1.1 | Additional physiological considerations | 93 |
| 5.1.2 | Expanding the cost function | 95 |

| | | |
|----------|--|------------|
| 5.1.3 | Improved representation of the arterial wall | 96 |
| A | Appendix | 97 |
| A.1 | From the Brinkman equation to Darcy's Law | 97 |
| A.2 | Derivation of the weighted concentration | 97 |
| A.3 | Including reaction at the endothelial surface | 98 |
| A.4 | Governing equation for the equilibrium case | 98 |
| A.5 | Remaining drug-dependent parameters of the model | 98 |
| A.6 | Diffusivity of sirolimus | 99 |
| | Bibliography | 101 |

Abstract

Drug-eluting stents (DES), which release anti-proliferative drugs into the arterial wall in a controlled manner, have drastically reduced the rate of in-stent restenosis and revolutionized the treatment of atherosclerosis. However, late stent thrombosis remains a safety concern of DES, mainly due to delayed healing of the wound inflicted during DES implantation. We present a framework to optimize DES design such that restenosis is inhibited without affecting the healing process. To this end, we have developed a computational model of blood flow and drug transport in stented arteries which provides a metric for quantifying DES performance. The model takes into account the multi-layered structure of the arterial wall and incorporates a reversible binding model to describe drug interaction with the cells of the arterial wall. The model is coupled to a novel optimization algorithm that minimizes the DES performance metric to identify optimal DES designs. We show that optimizing the period of drug release from DES and the initial drug concentration within the coating has a drastic effect on DES performance. Optimal paclitaxel-eluting stents release the drug either within a few hours or slowly within a year at concentrations considerably lower than current DES. Optimal sirolimus-eluting stents require a slow drug release. Optimal strut shapes for DES are elongated and can be streamlined only if the drug release occurs quickly. The results offer explanations for the performance of recent DES designs, demonstrate the potential for large improvements in DES design relative to the current state of commercial devices, and define guidelines for implementing these improvements.

Résumé

L'utilisation de stents actifs (DES) a révolutionné le traitement de l'athérosclérose. Le relargage contrôlé de médicaments anti-prolifératifs dans la paroi artérielle (PA) a permis de réduire fortement le taux de resténose intra-stent. Mais le risque de thromboses intra-stents tardives demeure un enjeu majeur des DES en partie lié au retard de cicatrisation de la PA endommagée lors de l'implantation. Cette thèse présente une méthode d'optimisation du design des DES afin d'inhiber la resténose sans affecter la cicatrisation. Pour quantifier la performance des différents designs, un modèle numérique décrivant l'écoulement sanguin et le transport de médicaments dans les artères stentées a été développé. Il prend en compte la structure multi-couches de la PA et les interactions du médicament avec les cellules. Un algorithme d'optimisation est couplé au modèle afin d'identifier les DES optimaux. L'optimisation du temps de relargage ainsi que de la concentration initiale du médicament dans le revêtement du DES ont un effet significatif sur la performance. Lorsque le médicament utilisé est le paclitaxel, les solutions optimales consistent à relarguer le produit à des concentrations nettement inférieures à celles des DES actuels soit pendant quelques heures, soit pendant une durée d'un an. Pour le sirolimus, un relargage lent est nécessaire. Les formes optimales des spires du DES sont toujours allongées mais profilées seulement lorsque le relargage est rapide. Ces résultats permettent d'expliquer en partie les performances des différents DES récents et révèlent un fort potentiel d'amélioration dans la conception des DES par rapport aux dispositifs commerciaux actuels.

Acknowledgments

Do or do not. There is no try.
– Yoda

When somebody asks me whether or not he should start a PhD, I always tell him the same thing: “If you want to do it, you should do it! But be aware of one thing: You need to know why you are doing it. Take that reason, set it in stone and then put that stone aside. Now, whenever you are going through rough times during your PhD, and believe me you will, get that stone out again and look at the reason you wrote down. It will help you get through those times.” Well, I have followed my own advice and I have done it. The thesis is now complete. But I could not have made it without the support of many people who became part of this PhD journey. I would thus like to use this opportunity to thank this *Fellowship of the Thesis*:

I want to start by thanking my advisor *Abdul Barakat*. Without him the last 3.5 years would have been very different for me and none of this would have ever happened. It was him who introduced me to the field of Biomedical Engineering, a field I would have never ever considered to work in before I met him. The list of things I have to thank him for is endless, but I want to highlight the following of his greatest virtues: his never ending patience in the process of turning an Aerospace engineer into a Biomedical Researcher, his ability to keep me on track without restricting my activities and his supporting attitude for all my ventures.

Second, I want to thank my co-advisor *Jean-Marc Chomaz* who provided me with a very different and complimentary input throughout this PhD. He made me appreciate the more fundamental, physical side of this project. I will never forget the long, creative and stimulating discussions early on in the thesis focusing on the physics of drug-eluting stents in arteries. An hour of discussion typically corresponded to a week of work after decompression of all the content that was packed into his input. The other period I’ll never forget is the writing period. It sure was a painful process but a very fruitful one that made me understand what good scientific writing should be like.

I feel very lucky and grateful having had the opportunity to work with such a unique team of teachers, my Yoda and Obi-Wan Kenobi, who guided me on my path.

As the title of the dissertation suggests, a large part of this PhD was concerned with optimization. I would thus like to thank the “optimization team” that accompanied me throughout these years: First of all *Tom Bewley* and *Paul Belitz* who not only developed LabDOGS but also made their code available, familiarized me with the essential basics of the Surrogate Management Framework and the particularities of LabDOGS and gave support for their code. The second half of this team, on this side of the Ocean, consists of *Peter Schmid* and *Lutz Lesshafft* who were always available for discussions and advice.

Next I would like to thank the two Post-Docs (the Jedi Knights you might say) *Fulvio Martinelli* and *David Gonzalez-Rodriguez*: early on Fulvio helped getting that nasty reaction

equation to work and David helped design one of the core pieces of this thesis: the Bozsak-Gonzalez-Function or as it is referred to in this dissertation, the cost function. But David's support does not end there and I thus want to thank him in particular for the creative hours spent during our "Black Meetings"!

A very special thanks goes to the great magician Daniel "Dani" Guy. In the end, the successful completion of this thesis depended on computations and without him none would have happened. Dani is the most amazing system and network administrator I ever had the pleasure to meet. His wisdom, experience and dedication turned the impossible into the possible and just a click away.

I thank the external members of my thesis committee *Antoine Lafont*, *Gabriele Dubini*, *James Moore* and *Alexander Forrester* for taking the time to evaluate this thesis and improve it with their insightful and valuable comments. Moreover, I want to thank *Gabriele Dubini*, *James Moore* and *Alexander Forrester* for their scientific work which inspired parts of this thesis and *Antoine Lafont* for giving me the opportunity to follow him into the OR and experience PCI for real and not just in the literature and videos.

I thank *Philipp Schlatter* and *Ellen* at KTH who are responsible for the heaviest lifting in terms of computations that without them would not have been possible.

I also want to thank *Stephan Savarese* at COMSOL France for the continuous technical support throughout these years which more often than not went beyond what would be considered standard tech support.

I also would like to thank *Delphine Lhuillier* who eased the pain of administrative acts and always made sure I eventually got paid.

The LadHyX is a very unique lab and place to work. I am very grateful for having been welcomed into this family and I want to thank each and every member for their hospitality, kindness and support.

I also thank *John Williams* and *Richard Castle* for getting me through writer's block while writing this dissertation.

Even if one cannot really talk about an actual work/life balance during a PhD, there is a life outside of the lab and apart from work, and I would like to thank all the people who made the balance part of life so much more enjoyable even though I was far from home. In particular, I want to thank (in alphabetical order): *Anette*, *Christelle*, *Cristobal*, *Fabien*, *Miguel*, *Nerissa*, *Nicolas*, *Sonia*, *Olu*, *Xavier*; there's a special story attached to each one of you.

Last but certainly not least, I want to thank my family: my *Mum and Dad* for being the best parents one can wish for; my brother *Christian* for making the last half year in Paris a very special one and for helping me out with the basics of human physiology; my *grandfather*, the engineer in our family who inspired my own path and my *grandmother* who is responsible for laying the language foundations necessary to write a dissertation in English in France.

The final thanks go to my Princess *Gini*, the person who probably suffered most from my decision to go to Paris for my PhD. For almost a decade she has been at my side, being my source of inspiration and giving me the strength and support to accomplish whatever I desire and to always push further beyond my own limits.

List of Figures

| | | |
|------|---|----|
| 1.1 | Development of atherosclerosis | 2 |
| 1.2 | Stenting procedure | 4 |
| 2.1 | Model geometry and computational mesh | 11 |
| 2.2 | Baseline simulation (paclitaxel) | 21 |
| 2.3 | Sensitivity analysis (paclitaxel): dependence on SES Peclet number, radial medial Peclet number, axial medial Peclet number | 23 |
| 2.4 | Sensitivity analysis (paclitaxel): dependence on medial porosity | 24 |
| 2.5 | Sensitivity analysis (paclitaxel): dependence of maximum normalized mean concentration on Reynolds number in the lumen | 25 |
| 2.6 | One-layer vs. two-layer modeling (paclitaxel): normalized velocity and normalized concentration field | 25 |
| 2.7 | One-layer vs. two-layer modeling (paclitaxel): normalized mean concentration for two different SES thicknesses | 26 |
| 2.8 | Comparison of reversible binding reaction model (baseline model) to an equilibrium binding model | 27 |
| 2.9 | Paclitaxel vs. sirolimus: bound drug fraction | 27 |
| 2.10 | Paclitaxel vs. sirolimus: temporal evolution of the normalized mean concentration and integral Damköhler number | 29 |
| 3.1 | Two configurations of the computational model | 35 |
| 3.2 | Shape of the cost function and its contributing scores | 37 |
| 3.3 | Paclitaxel baseline optimization | 43 |
| 3.4 | Release kinetics and resulting normalized concentration distributions for representative designs of the <i>quasi-bolus</i> , <i>first-order</i> , and <i>zero-order</i> regions | 46 |
| 3.5 | Filled contour plot of the cost function over the design space for a paclitaxel-eluting stent | 48 |
| 3.6 | Sirolimus optimization | 49 |
| 3.7 | Normalized concentration distribution for optimal release from a sirolimus-eluting stent at one week post implantation | 50 |
| 4.1 | Different shapes generated with the Superformula | 57 |
| 4.2 | Flow diagram of the optimization algorithm and its coupling to the computational model. | 61 |
| 4.3 | One-dimensional example of Kriging | 62 |
| 4.4 | Polling the design space | 63 |
| 4.5 | Sensitivity estimation of J_{FDI} | 72 |

| | | |
|------|---|----|
| 4.6 | Sensitivity estimation of J_{ETH} | 73 |
| 4.7 | Optimization case 1: estimated global trends of the cost function of the P-DES (configuration E2) strut design optimization for a variation of semi-strut height a_s and semi-strut width b_s | 77 |
| 4.8 | Optimization case 1: optimal P-DES strut designs compared to sub-optimal strut designs similar to commercial strut designs for $w_{FDI} = 0.5$ and configuration E2 . . . | 77 |
| 4.9 | Optimization case 2: optimal P-DES strut design compared to sub-optimal strut design with smaller a_s for $w_{FDI} = 0.5$ and configuration E1 | 79 |
| 4.10 | Optimization case 3: optimal P-DES strut design for $w_{FDI} = 10$ and configuration E1 | 80 |
| 4.11 | Optimization case 4: estimated global trends of the cost function of the high-dose S-DES (configuration E2) strut design optimization for a variation of semi-strut height a_s and semi-strut width b_s | 80 |
| 4.12 | Optimization case 4: optimal high-dose S-DES strut design compared to sub-optimal strut designs similar to commercial strut designs for $w_{FDI} = 0.5$ and configuration E2 | 81 |
| 4.13 | Optimization case 5: optimal high-dose S-DES strut design for $w_{FDI} = 0.5$ and configuration E1 | 82 |
| 4.14 | Optimization case 6: optimal low-dose S-DES strut design for $w_{FDI} = 0.5$ and configuration E1 | 83 |
| 4.15 | Optimal two-layered polymer coating properties for $w_{FDI} = 0.5$ and configuration E1 | 84 |
| 5.1 | Optimal fast-release P-DES strut design | 94 |

List of Tables

| | | |
|-----|--|----|
| 2.1 | Reference values for the non-dimensional equations and reference non-dimensional quantities | 12 |
| 2.2 | Fluid model parameters | 15 |
| 2.3 | Transport model parameters for paclitaxel and sirolimus | 17 |
| 2.4 | Non-equilibrium reaction model parameters for paclitaxel and sirolimus | 17 |
| 2.5 | Time scales and dimensionless quantities for the stented part of the media for paclitaxel and sirolimus | 19 |
| 3.1 | Calibration parameters of the cost function | 39 |
| 3.2 | Detailed cost function score data of the points 1 - 4 in Fig. 3.3 and 5 - 7 in Fig. 3.5 | 44 |
| 4.1 | Model parameters and design variables of the computational model with respective design and sensitivity ranges | 70 |
| 4.2 | Group 1 optimization runs: strut design optimization | 75 |
| 4.3 | Group 2 optimization runs: two-layered polymer coating optimization | 83 |
| 4.4 | Summary of estimated global trends of the cost function of paclitaxel- and high-dose sirolimus eluting stent strut design optimizations with a FDI weight $w_{\text{FDI}} = 0.5$. . . | 86 |

Nomenclature

| | |
|------------------|--|
| a_s | semi-strut height |
| A_d | zero-sum lattice of dimension d |
| b | superficially averaged bound concentration |
| b_{\max} | maximum binding site density |
| b_s | semi-strut width |
| B_p | binding potential |
| c_0 | initial concentration in the stent polymer |
| c_{eff} | (minimum) efficacious concentration threshold |
| c_j | superficially averaged free concentration in layer j |
| c_{tol} | tolerable concentration threshold |
| c_{tox} | toxic concentration threshold |
| c_T | superficially averaged total concentration |
| d | dimension |
| d_s | strut diameter |
| d_h | hydrodynamic strut diameter |
| \mathbb{D} | design (hyper-)space |
| Da_1 | first Damköhler number in the media |
| Da_2 | second Damköhler number in the media |
| D_j^i | effective diffusion coefficient in layer j in direction i (isotropic diffusion assumed when no superscript) |
| D_d | checkerboard lattice of dimension d |
| e_l | elementary effect of design variable l |
| f_{cb} | ratio of initial concentration and maximum binding site density |
| FDI | flow disturbance index |
| $G^{(k)}$ | grid size after k grid refinements |
| H_j | homogeneity score in layer j |
| I_j | inefficacy score in layer j |
| $J_{s,j}$ | solute flux through membrane j |
| $J_{v,j}$ | fluid flux through membrane j |
| J_{ETH} | drug-related cost function |
| J_{FDI} | flow-related cost function |
| J | (total) cost function |
| k_p | concentration dependent partition coefficient |
| k_B | Boltzmann's constant |
| K_d | ratio of binding k_f and unbinding k_r reaction coefficient |
| L_j | thickness of layer j |

| | |
|------------------------------|--|
| $L_{p,j}$ | hydraulic conductivity of membrane j |
| m_s | parameter of the Superformula |
| M_i | molecular weight of drug i |
| n_i | exponents of the Superformula |
| n | strut shape exponent |
| N_A | Avogadro's number |
| p_j | pressure in layer j |
| p_l | tuning parameter of the Kriging model for design variable l |
| p_{st} | percentage of stent strut embedment |
| P_j | permeability of membrane j |
| $P_{D,j}$ | Darcy permeability in layer j |
| Pe_j^i | Peclet number in layer j in direction i (isotropic Peclet number assumed when no superscript) |
| Pe_j^* | membrane Peclet number in membrane j |
| r, z | radial and axial coordinates |
| r_{cor} | correlation coefficient |
| r_f | average radius of fibers of the extracellular matrix |
| r_{mol}^i | average molecular radius of drug i |
| Re | Reynolds number |
| Re_l | luminal Reynolds number |
| Re_d | Reynolds number based on the hydrodynamic strut diameter |
| Sc | Schmidt number |
| \mathbb{O} | cost function (hyper-)space |
| s | uncertainty |
| s_j | sieving coefficient in membrane j |
| S | surface |
| t | time |
| t_{end} | simulation time |
| t_E | emptying/release time |
| tpd_f | therapeutic domain factor |
| T | temperature |
| T_j | toxicity score in layer j |
| T_G | target of improvement |
| $\mathbf{u} = (u \ v \ w)^T$ | velocity |
| V_j | volume of layer j |
| w_{FDI} | FDI weight factor |
| x_l | design variable l |
| \tilde{Y} | dimensional form of quantity Y |
| α | tuning parameter of the target value of improvement |
| β | angle |
| γ_j | hindrance coefficient in layer j |
| γ_{thr} | scaling factor of the toxicity score |
| Γ_j | boundary j |
| δ_c | concentration boundary layer thickness |
| ε_j | porosity in layer j |

| | |
|---------------------|---|
| $\varepsilon_{f,j}$ | fiber matrix porosity in layer j |
| κ | total binding coefficient |
| λ_d | laminated lattice of dimension d |
| Λ_j | lag coefficient in layer j |
| μ | fluid dynamic viscosity |
| ρ | fluid density |
| $\sigma_{f,j}$ | Staverman reflection coefficient in membrane j |
| τ | wall shear stress |
| θ_l | tuning parameter of the Kriging model for design variable l |
| $\Phi_{f,j}$ | reduction coefficient |

Superscripts and subscripts

| | |
|----------|-------------------------|
| 0 | reference value |
| b | blood |
| COD | current optimal design |
| e | endothelium |
| eel | external elastic lamina |
| eval | evaluated |
| fail | failed |
| flt | filtering |
| FDI | flow disturbance index |
| iel | internal elastic lamina |
| imp | imputing |
| l | lumen |
| lim | limit |
| m | media |
| max | maximum |
| min | minimum |
| p | plasma |
| PAX | paclitaxel |
| ses | subendothelial space |
| SIR | sirolimus |
| SMC | smooth muscle cells |
| th | therapeutic domain |
| thr | threshold |
| w | arterial wall |
| α | liquid phase |

Abbreviations

| | |
|-----|----------------------------------|
| BDF | backward differentiation formula |
|-----|----------------------------------|

| | |
|-------|---|
| BLE | boundary layer elements |
| BMS | bare-metal stent |
| COD | current optimal design |
| DCB | drug-coated balloon |
| DES | drug-eluting stent |
| EEL | external elastic lamina |
| FDI | flow disturbance index |
| FEM | finite element method |
| IEL | internal elastic lamina |
| LST | late stent thrombosis |
| NC | normalized concentration |
| NMC | normalized mean concentration |
| NV | normalized velocity |
| OLM | one-layer model |
| RHS | right hand side |
| RMC | remaining mass percentage in the polymer coating |
| PCI | percutaneous coronary intervention |
| POBA | plain old balloon angioplasty |
| SCAAR | Swedish Coronary Angiography and Angioplasty Registry |
| SES | subendothelial space |
| SMC | smooth muscle cell |
| SMF | surrogate management framework |
| TLM | two-layer model |

Introduction

1.1 Atherosclerosis: a human condition?

Ischemic heart disease, stroke, and other cerebrovascular disease are the leading cause of mortality in the world accounting for one in four deaths [195]. In most cases, the development of these pathologies is attributed to the slow but steady process of narrowing and calcification of arteries, known as atherosclerosis.

Though sometimes referred to as a “disease of affluence” [46] or “lifestyle disease”, the factors contributing to the development of atherosclerosis go beyond a high cholesterol diet, a sedentary lifestyle, and smoking. Diabetes, reduced levels of high density lipoprotein (HDL) to low density lipoprotein (LDL) ratio in the bloodstream, male gender, family history of cardiovascular disease, and hypertension all point to an important involvement of genetics in the development of atherosclerosis. A recent investigation performed on 137 mummies from four different ancient cultures (including pre-agricultural hunter-gatherers) [176] shows that atherosclerosis has afflicted humans for at least four millennia and suggests the possibility that atherosclerosis may be a condition inherent to human aging.

The development of atherosclerosis is a complex process initiated, according to current understanding, by an inflammation of the endothelium [109]. The endothelium, the cellular monolayer lining the inner surfaces of blood vessels, usually acts as a selective permeability barrier that protects a healthy arterial wall from antagonistic substances in the bloodstream. Inflammation increases endothelial permeability, enabling the deposition and accumulation of plasma proteins, most prominently LDL, in the subendothelial space (SES) of the arterial wall [47, 117, 160]. Trapped in the SES, LDL is oxidized, which positively reinforces the inflammatory response of the endothelium. Simultaneously, monocytes are recruited to the site of inflammation and transmigrate through the endothelium, where they differentiate into macrophages and take up oxidized LDL. The rapid uptake of oxidized LDL transforms macrophages into foam cells. The debris created by apoptosis and necrosis of foam cells initiates the formation of plaque in the SES. Subsequent smooth muscle cell (SMC) proliferation into and migration from the medial layer of the arterial wall [110, 161] further advances the lesion and its protrusion into the lumen (Fig. 1.1).

This cascade of events results in the formation of a complex plaque in the arterial wall which, if sufficiently advanced, can result in restriction of blood supply to the surrounding

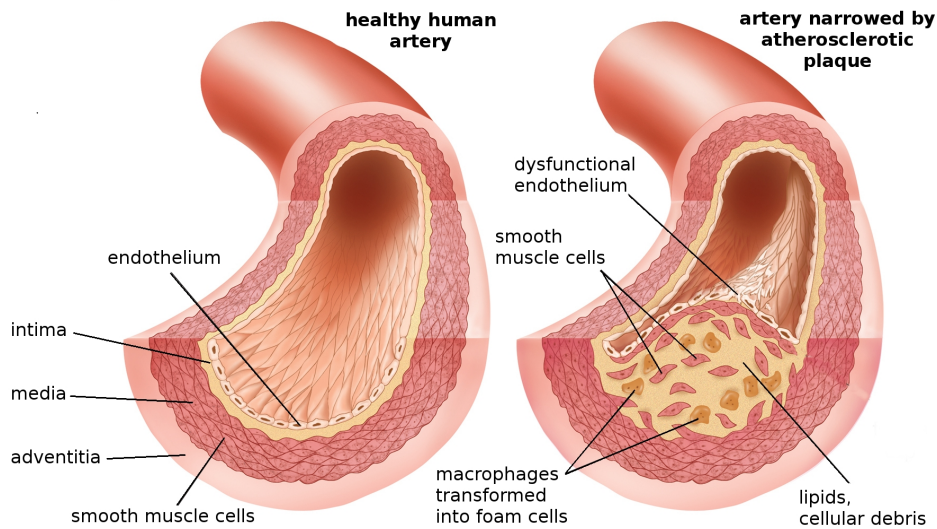


Figure 1.1: Development of atherosclerosis. *Left*: Healthy artery comprising the three arterial layers: intima (covered by endothelial cells), media (with smooth muscle cells), and adventitia. *Right*: Artery diseased by atherosclerosis – lipids, macrophages, and smooth muscle cells have penetrated the intima at a site of dysfunctional endothelium; foam cells and cellular debris form the atherosclerotic plaque. Adapted from Encyclopædia Britannica Online.

tissue. If the obstructed artery is a coronary artery, the reduced oxygenation, referred to as myocardial ischemia, leads to pathological consequences that range from chest pain under stress conditions (stable angina) to constant pain even at resting conditions (unstable angina). In the most severe cases, the blood supply to parts of the heart muscle is cut off entirely (acute coronary syndrome) resulting in a heart attack.

A central question in the study of atherosclerosis is to identify the mechanism that initiates the inflammation and subsequent dysfunction of the endothelium. Although this question has attracted tremendous scientific attention, it has yet to be conclusively answered. A critical observation in this regard, however, is that atherosclerosis is a focal disease with early lesions developing preferentially in regions of arterial branching and curvature [159, 169]. Within these regions of abrupt changes in arterial geometry, arterial blood flow is “disturbed”, strongly suggesting fluid mechanical implication in the initiation of atherosclerosis [8, 14, 28–30, 33, 58, 98, 133].

Understanding the role of arterial flow disturbance in the development of atherosclerosis requires elucidating the effect of flow on endothelial cell (EC) function and dysfunction. Over the past two decades, numerous studies have demonstrated that flow elicits humoral, metabolic, and structural responses in ECs [13, 32, 41]. The mechanisms by which ECs sense fluid mechanical forces and subsequently transduce these forces into biochemical signals that regulate cellular function remain incompletely understood and are under intense investigation. One of the most well documented flow responses in the literature is the effect of flow on EC morphology. ECs exposed to steady flow or to non-reversing pulsatile flow become highly elongated and aligned in the direction of flow [15, 43, 45, 75, 115, 134]. On the other hand, ECs subjected to “disturbed” flow in the form of very low or directionally oscillating flow maintain a cuboidal

morphology similar to that of cells in static culture [72, 75]. Interestingly, cuboidal ECs appear to exhibit significantly higher permeability to macromolecules than elongated ECs. Elucidating possible relationships between EC morphology and cell function and dysfunction promises to provide critical information regarding the role of flow in the development of atherosclerosis.

1.2 Treatment of atherosclerosis: a brief history

While treatment of stable angina typically involves administration of medication and specific recommendations for lifestyle changes [22], lesions leading to unstable angina or even acute coronary syndrome require surgical intervention. In 1977 Andreas Grüntzig opened an entirely new chapter in the treatment of obstructed coronary arteries by inflating a catheter-mounted balloon at the site of the stenosis to re-open the artery [130]; percutaneous coronary intervention (PCI) was thus born. The great benefit of catheter-based balloon angioplasty (today referred to as "plain old balloon angioplasty" or POBA) for the patient was that the treatment was minimally invasive and did not require open heart surgery leading to significantly reduced recovery times.

Despite representing a major advance in cardiovascular intervention, POBA was not without its problems. In more than 50% of the cases this treatment failed due either to immediate vessel recoil or arterial restenosis (re-occlusion of the blood vessel due to uncontrolled growth of smooth muscle cells (SMCs) in reaction to the injury inflicted by the balloon). Another major advance was made in 1986 when Jacques Puel performed the first PCI on a human with a Palmaz-Schatz stent mounted on the balloon. The *stent*¹, a tubular wire-mesh, remained in the artery after the intervention to serve as a permanent scaffold (Fig. 1.2). Although the use of a stent in PCI cut the rate of restenosis in half compared to POBA, restenosis remained a major complication in an unacceptably large fraction of the procedures. Restenosis occurs due to the uncontrolled proliferation of SMCs and their migration from the media into the intima (neointimal hyperplasia) and ultimately into the lumen where they form a new obstruction to blood flow.

The breakthrough that would eventually lead to almost complete elimination of restenosis [157] was the development of drug-eluting stents (DES) which involve the addition of an anti-proliferative drug to the metallic bare-metal stent (BMS). The drug, most commonly sirolimus (or one of its derivatives) or paclitaxel, is released into the arterial wall where it inhibits SMC proliferation and hence prevents neointimal hyperplasia. With more than 7 million stent implantations per year worldwide (most of which are DES), the stent has become the most successful medical device for the treatment of advanced coronary atherosclerosis today.

The drawback of using anti-proliferative drugs on stents is that these drugs also retard the healing process following the implantation process, mostly (but not exclusively) by delaying the recovery of the endothelium [54, 84, 85, 190]. Delayed endothelial recovery is associated with an elevated risk of late and very late stent thrombosis [53, 69, 84, 116, 131]. Stent thrombosis is the sudden formation of blood clots at the site of stent implantation. Depending on the time of occurrence relative to the intervention, stent thrombosis is classified in four types [170]: acute, within the first 24 hours; sub-acute, within the first 30 days; late, within the first year; and very late, after the first year.

Whereas acute and sub-acute stent thrombosis are inherent to the foreign body response following implantation of stents (BMS or DES) [150], late and very late stent thrombosis

¹named after English dentist Charles Thomas Stent (1807–1885) [21, 104, 154]

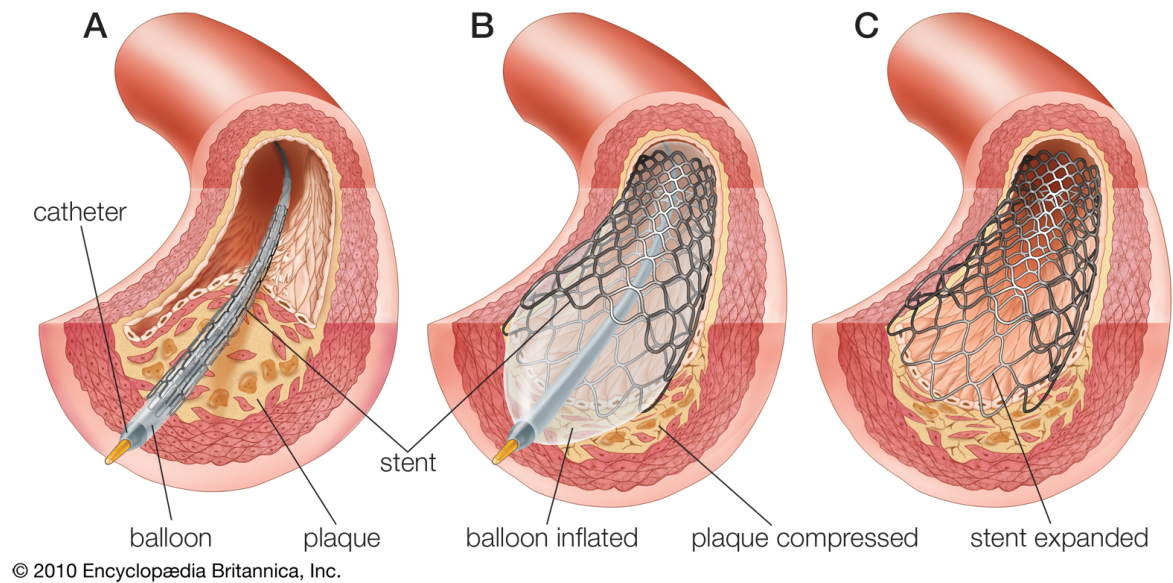


Figure 1.2: Stenting procedure. **A:** A balloon-mounted stent is introduced to the site of the occlusive atherosclerotic lesion via a catheter. **B:** The balloon is inflated at high pressure so that the balloon and stent compress the atherosclerotic plaque thereby re-opening the artery and restoring blood flow. **C:** The balloon is retracted and the stent remains as a permanent scaffold. Source: Encyclopædia Britannica Online.

are far more likely to occur with DES than BMS. The unpredictability and high mortality of stent thrombosis make this complication, though rare, particularly serious. Addressing this complication requires extending the duration of an anti-thrombotic treatment in the aftermath of the surgery. The optimal duration of anti-thrombotic treatment remains, however, unknown.

In light of these complications, questions have recently arisen on whether the scaffolding and drug elution characteristics of a stent are needed for longer than 6 months after the surgery. Proliferation of SMCs is significant for only the first few weeks [150], and complete remodeling of the arterial wall is achieved within approximately 3 months [137]. In recent years, the above considerations have resulted in the development of biodegradable stents [61, 137] and in the revival of balloon angioplasty but now using balloons coated with an anti-proliferative drug, usually paclitaxel [66]. While both treatment options show very promising results, their long-term efficacy are yet to be established.

1.3 Anti-proliferative drugs: bliss and curse of drug-eluting stent design

A DES is comprised of three components: a stent body which provides the structural support, the drug to be eluted, and the drug carrier in which the drug is loaded and through which it is delivered. Each of these components has its own requirements [27, 101, 142]. The stent body needs to supply sufficient radial and axial strength, it needs to be very flexible to be easily deliverable even to the most complicated lesion, and the struts need to have a low

profile to limit arterial damage at implantation and to minimize disturbance of the flow field in order to reduce the risk of thrombosis and facilitate re-endothelialization [33, 44, 96]. The geometry of the stent body also determines the release pattern for the drug into the arterial wall [11, 24, 51, 125, 127, 128, 162, 183, 201].

The drug carrier (typically a polymer) should be bio-compatible to prevent an inflammatory or rejection reaction. It should also enable controlled and sufficient release of drug, such that drug concentration in the arterial wall remains within the therapeutic window, i.e. sufficiently high to be effective and yet sufficiently low to avoid toxicity. The drug itself should effectively inhibit SMC proliferation within the first few weeks after the implantation [150] without causing secondary or long-term effects that compromise the integrity of the arterial wall. Finally, all of the stent's components need to be finely tuned for the treatment to be successful both in the short and long terms.

How crucial stent design is to the success of a stenting procedure was emphasized by the results of the Swedish Coronary Angiography and Angioplasty Registry (SCAAR) study [157] which demonstrated the superiority of second generation DES over both first generation DES and BMS. Second generation DES have undergone major design changes in their geometry, drug composition, and the composition of the drug carrier relative to the first generation devices [60]. Even among different second generation DES, significant differences in re-endothelialization outcomes have been observed with different stent designs [85, 132, 172].

The release kinetics of the drug from the drug carrier also play a crucial role for determining the therapeutic efficacy of a DES [7, 68, 102, 152, 165]. Moreover, the drug itself can be a design variable; interestingly, all drug-coated balloons currently under development use paclitaxel as the therapeutic agent of choice which is in contrast to developments in second generation DES, where manufacturers have for the most part opted for sirolimus (or its analogues) as the drug of choice.

1.4 Modeling drug transport in the arterial wall

The transport of an eluted drug within the arterial wall is governed by convection and diffusion through the tortuous pore space and to interactions with the cells of the arterial wall, most notably ECs and SMCs. If we want to understand and evaluate the therapeutic performance of DES, we need to first understand the processes occurring in the arterial wall, for which computational models would be particularly helpful. Consequently, significant scientific effort has been dedicated to study and model the transport of drugs [38, 81, 82, 105, 114, 179–181] in the arterial wall, resulting in a variety of different modeling approaches ranging from relatively simple models that assume either a low drug diffusivity in the arterial wall [128] or a constant partition of bound and free drug [200] to more sophisticated models where drug interactions with the arterial wall are described by a second-order reversible reaction [24, 179]. With very few exceptions [51], these models approximate the arterial wall as a single homogeneous layer and often neglect convective drug transport within the wall.

1.5 Stent design optimization

The broad variability in therapeutic success of DES in clinical use suggests that today's DES designs are not necessarily optimal. Recognizing the shortcomings of today's stents, pioneering studies of stent design optimization have been conducted over the past few years [9, 70, 71,

140, 141, 171]. These studies have so far been limited to optimizing geometrical features of stents.

Modeling the physiologically relevant phenomena associated with stenting leads to complex computational models (see Chapter 2, [24, 51, 139]) that are computationally expensive to evaluate. A very versatile optimization framework used in the case of expensive computational simulations is the surrogate management framework (SMF) [23], since the use of classical optimization methods is often rendered infeasible. The SMF algorithm is a derivative-free optimization method which explores the space of possible designs by repeatedly evaluating the computational model for different sets of design variables. The algorithm uses a succession of search and poll steps to identify a set of design variables that yields the most optimal design. This method has previously been applied to the optimization of various aerospace [118, 119] and bioengineering [120, 198] systems.

1.6 Scope and outline of the present dissertation: optimization of drug-eluting stents

The present dissertation applies computational modeling to derive guidelines for novel stent designs that optimize DES performance. Recovery of the endothelium is particularly important for the success of a DES. Thus, we will focus our attention on the phenomena that appear to have a crucial impact on the endothelium: transport of the anti-proliferative drug eluted from the stent drug carrier and disturbance of the flow field due to the geometric design of the stent.

In this work we will try to answer the following questions: What is an optimal stent? What design elements are crucial for obtaining an optimal stent? What should these design elements look like for an optimal stent? What is the role of the choice of drug in the optimization?

We propose the following strategy to answer these questions: 1) We develop a computational model of fluid flow and drug transport in stented arteries which serves to evaluate the performance of DES design. 2) We formulate a metric that quantifies DES performance. 3) We use a derivative-free optimization algorithm to minimize the cost function derived from the metric and hence identify optimal DES designs.

In Chapter 2 we develop a computational model of drug transport that takes into account the multi-layered structure of the arterial wall, includes both convective and diffusive transport in the arterial wall, and incorporates a reversible binding model to describe drug interactions with the cells of the arterial wall [179]. The computational model is applied to study the transport dynamics of the two hydrophobic drugs paclitaxel and sirolimus. The sensitivity of the model predictions to several modeling parameters is also presented. The results of the simulations indicate a strong coupling between the drug dynamics in the arterial wall and the release kinetics of the drug from the stent drug carrier. This finding motivates the optimization of the drug delivery strategy, which we perform in Chapter 3.

In Chapter 3 we introduce a cost function that serves as a quantitative measure of DES performance that assesses how well the applied drug delivery strategy maintains efficacious but sub-toxic drug concentration in the media while simultaneously minimizing drug concentration at the endothelial surface to facilitate re-endothelialization. We then minimize this cost function by coupling a novel SMF optimization algorithm [16, 17] with our physiologically-based computational model derived in the previous chapter. Applying this approach, we identify the different drug delivery strategies that are needed for paclitaxel and sirolimus to yield optimal DES performance.

Once drug delivery is optimized, Chapter 4 moves on to optimize DES strut shape. To this end, we extend our cost function to include a measure of the flow disturbance caused by the stent geometry. The particular SMF algorithm used here, which to our knowledge has never before been applied to engineering optimization, is particularly well suited to perform these more complex optimizations due to its regular and dense discretization of the design space and its novel poll step procedure. An analysis of the sensitivity of our cost function motivates the refinement of the optimization of the DES drug delivery strategies. The results of our investigation demonstrate that, to achieve optimal DES performance, strut shape and drug delivery need to be tailored to the drug dynamics in the arterial wall.

The concluding remarks at the end of the dissertation contain a comprehensive summary of the results of all three chapters and make specific recommendations for future investigations.

Modeling the Transport of Drugs Eluted from Stents

2.1 Introduction

Despite the recent data of the Swedish Coronary Angiography and Angioplasty Registry (SCAAR) study [157] that suggest that the overall performance of drug-eluting stents (DES) is superior to that of bare-metal stents (BMS), the long-term safety and efficacy of DES remain controversial. The primary concern stems from the risk of late and very late stent thrombosis, thought to be principally attributable to delayed endothelial healing at the site of stent implantation. In an attempt to avoid the complications associated with DES, an emerging technology is the use of drug-coated balloons (DCB), either with or without subsequent stent implantation [66]. Interestingly, all DCB devices currently under development use paclitaxel as the therapeutic agent of choice. This is in contrast to developments in the latest generation DES, where manufacturers have for the most part opted for sirolimus or its derivatives as the drug of choice. DCB and DES have fundamentally different strategies for delivering drugs to the arterial wall: DCB deliver a very high drug dose ($200 - 300 \mu\text{g}/\text{cm}^2$) in a very short time whereas DES deliver a considerably lower dose ($100 \mu\text{g}/\text{cm}^2$) over a period of several weeks.

Another important finding of the SCAAR study is that second-generation DES (such as Medtronic's Endeavor Resolute stent or Abbott's Xience V stent), which have undergone major design changes in their geometry, drug composition, and the composition of the polymeric coating within which the drug is embedded relative to first-generation DES, exhibit clearly superior performance. Most investigations to date of the effect of stent design on stent performance have focused on the role of detailed geometric features [11, 99, 163] or of DES polymeric coating [73]. The role of the drug elution process itself [12] and its coupling to the specific drug used [181] have received less attention and have thus far been limited to sirolimus.

Computational models of the transport of drugs eluted from DES or DCB within the arterial wall promise to significantly enhance our understanding of the performance of these devices. A number of different modeling approaches have been proposed ranging from relatively simple models that assume either a low drug diffusivity in the arterial wall [128] or a constant partition of bound and free drug [200] to more sophisticated models where drug interactions with the arterial wall are described by a second-order reversible reaction [179]. Multi-dimensional

models ([24, 128]), with the exception of the 3D model by Feenstra *et al.* ([51]), approximate the arterial wall as a single homogeneous layer and often neglect convective drug transport within the wall. Only 1D studies ([124, 146]) have thus far included the layered structure of the arterial wall into their models for describing the elution of drugs from stents. The diversity of modeling approaches, the different assumptions on which the models are based, and the limited experimental validation of the models render it difficult to compare the predictions of the different models and to make general conclusions. In some cases, different models can even lead to contradictory predictions: for example, the calculations by Vairo *et al.* [183] indicated insensitivity of the drug concentration profile in the arterial wall to luminal blood flow, while the work by Balakrishnan *et al.* [11] reached the opposite conclusion.

In an effort to better understand the validity and applicability of different model assumptions, the present work develops a computational model of the transport of the two drugs paclitaxel and sirolimus eluted from DES in the arterial wall. The model takes into account the multi-layered structure of the arterial wall and incorporates a reversible binding model to describe drug interactions with the constituents of the arterial wall. The effects of assuming a one-layer model for the arterial wall or equilibrium reaction conditions are explored. Finally, the model is used to study the coupling between the drug release kinetics from the stent and the drug dynamics in the arterial wall.

2.2 Materials and methods

2.2.1 Model geometry

A 2D axisymmetric geometry is used in all simulations. We consider a straight arterial segment within which a model DES represented by 10 circular struts is deployed (Fig. 2.1). Stent strut size, polymer thickness, and stent inter-strut spacing are adapted from the geometry introduced by Mongrain *et al.* [127] and recently also used by Vairo *et al.* [183]. Due to the reduction in the number of struts relative to those studies (10 struts instead of 15), our geometry is considered to represent a smaller lesion (7 mm). We have verified that this has no significant impact on the parameters of interest. Embedment of the stent struts in the arterial wall is assumed to be 50%. A sensitivity study investigating the effect of strut embedment in the 20% to 80% range revealed that while the magnitude of drug concentration in the arterial wall changes, the overall behavior and the conclusions drawn are not altered. We also define a therapeutic domain that extends three inter-strut spacings both upstream and downstream of the stent (Fig. 2.1) and that we consider to be the target zone for drug delivery. All computed variables are for this therapeutic domain.

2.2.2 Physical model

The mathematical framework for the description of the arterial wall is based on the two-layer model presented by Formaggia *et al.* [55]. We apply this model to the elution of the two small hydrophobic drugs paclitaxel and sirolimus from DES and complement it with a recently developed reaction model in the arterial wall [179]. Wherever possible, the model input parameters are derived from experimental data available in the literature.

The arterial wall is assumed to be rigid and is modeled as a two-layered structure with the subendothelial space (SES) and the media defined as distinct domains while the endothelium and internal elastic lamina (IEL) are treated as interfacial matching conditions. The adventitia

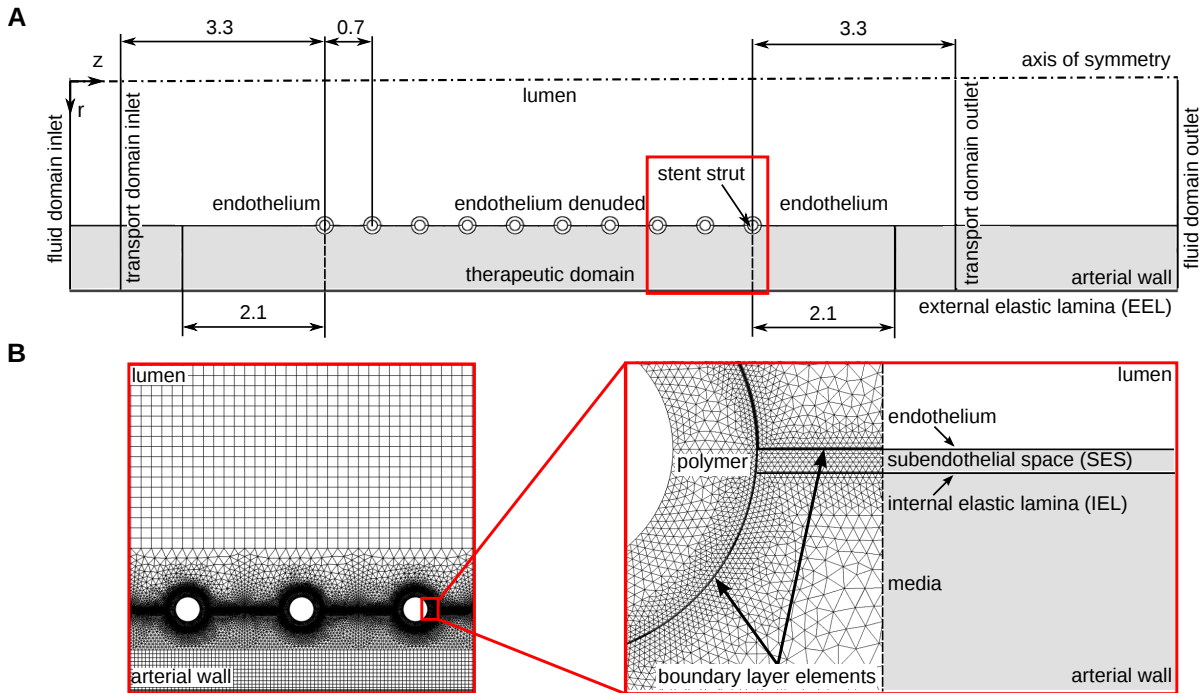


Figure 2.1: **A:** Model geometry with stent strut diameter $d_s = \text{metallic strut diameter} + 2 \cdot \text{polymer thickness} = 0.15 \text{ mm} + 2 \cdot 0.05 \text{ mm} = 0.25 \text{ mm}$. All scales are given in mm. Geometry not drawn to scale. **B:** Computational mesh: *Left:* Close-up on struts 4 through 6. *Right:* Detail of the intersection of polymer, lumen, SES and media with indication of boundary layer elements.

is not modeled as a distinct layer but rather as a boundary condition at the outer surface of the media. Because stent deployment is thought to lead to near complete denudation of the endothelium at the deployment site, we assume in the modeling a baseline configuration where the endothelium is absent within the stented portion of the vessel but is intact otherwise.

Drug transport is assumed to occur in the following four different domains: the arterial lumen, the stent polymer coating, the SES, and the media. Different physical phenomena dominate transport in each of these domains. In the polymer coating, we assume drug transport to be purely diffusive. In the lumen, drug is transported via both convection and diffusion. Each of the two layers of the arterial wall, i.e. the SES and the media, is modeled as a porous medium with its distinct homogenized (but in some cases anisotropic) properties. The SES is assumed to be devoid of all cells, so that drug transport within this layer occurs by convection and diffusion. In the media, three different processes govern drug concentration: convective and diffusive transport within the pore space, specific binding of the drug to smooth muscle cells (SMCs), and non-specific binding of the drug to the extracellular matrix accounted for through hindered diffusion.

2.2.3 Governing equations and boundary conditions

Unless stated otherwise, variables and equations are presented in non-dimensional form. Dimensional quantities are denoted by a tilde, and the reference values used in the non-dimensionalization

are provided in Table 2.1.

2.2.3.1 Momentum transport

In the arterial lumen, blood flow is assumed to be steady and is thus governed by the time-independent Navier-Stokes equations:

$$(\mathbf{u}_1 \nabla) \mathbf{u}_1 = -\nabla p_1 + \frac{1}{\text{Re}_0} \Delta \mathbf{u}_1, \quad (2.1)$$

$$\nabla \mathbf{u}_1 = 0, \quad (2.2)$$

where \mathbf{u}_1 and p_1 respectively denote the velocity and pressure in the lumen. Blood is assumed to be a Newtonian fluid, and a luminal Reynolds number of $\text{Re}_l = \tilde{u}_l \tilde{\rho} / \tilde{\mu}_b = 400$ is considered based on blood velocity magnitudes typically encountered in coronary arteries.

The SES and the media are considered as porous layers, and flow within these layers is assumed to be governed by Darcy's Law:

$$\nabla p_j = -\frac{\mu_{p,j}}{P_{D,j} \text{Re}_0} \mathbf{u}_j, \quad (2.3)$$

where the subscript j denotes either the SES or the media, \mathbf{u}_j is the average fluid velocity in the total volume (matrix plus pores), and $\mu_{p,j}$ and $P_{D,j}$ are the non-dimensional dynamic viscosity

Table 2.1: Reference values for the non-dimensional equations and reference non-dimensional quantities

| Quantity | Reference expression |
|---|---|
| (free and total) concentration c, c_T | initial drug concentration \tilde{c}_0 |
| (bound) concentration b | maximum binding site density \tilde{b}_{\max} |
| hydraulic conductivity L_p | $\rho_0^{-1} u_0^{-1}$ |
| second Damköhler number Da_2 | $\text{Da}_2^0 = \frac{\tilde{k}_f \tilde{b}_{\max} L_0^2}{(1-\varepsilon_j) D_0}$ |
| fluid density ρ | blood density $\rho_0 = \tilde{\rho}$ |
| diffusion D | diffusivity in blood $D_0 = \tilde{D}_b$ |
| length r, z | strut diameter $L_0 = \tilde{d}_s$ |
| Peclet number Pe | $\text{Pe}_0 = \frac{u_0 L_0}{D_0}$ |
| Darcy permeability P_D | L_0^2 |
| permeability P | diffusive velocity scale $\tilde{u}_D = \frac{D_0}{L_0}$ |
| pressure p | dynamic pressure $p_0 = \rho_0 u_0^2$ |
| Reynolds number Re | $\text{Re}_0 = \frac{u_0 L_0 \rho_0}{\mu_0}$ |
| time t | diffusive time scale $t_0 = \frac{L_0^2}{D_0}$ |
| fluid dynamic viscosity μ | blood dynamic viscosity $\mu_0 = \tilde{\mu}_b$ |
| velocity $\vec{u} = (u \ v \ w)^T$ | mean inlet velocity $u_0 = \tilde{u}_{\text{in}} = \frac{\tilde{u}_{\max, \text{in}}}{2}$ |

and Darcy permeability, respectively. In the polymeric coating of the stent, the flow is assumed absent and thus drug transport occurs solely by diffusion.

The following boundary conditions apply: at the inlet of the lumen region a laminar Poiseuille velocity profile is prescribed:

$$w_{1,\text{in}} = 2\bar{u} \left(1 - \left(\frac{2r}{d_1} \right)^2 \right), \quad (2.4)$$

while at the outlet the pressure is fixed at the physiological excess pressure value of $\tilde{p}_{\text{out}} = 100$ mmHg. The top boundary of the luminal domain is the symmetry axis of the problem. The endothelium and IEL are approximated as semi-permeable membranes with the endothelium coupling flow in the lumen to that in the SES and the IEL serving as an interfacial matching condition between the SES and the media. To describe these membranes, we use the Kedem-Katchalsky equation [91] governing the fluid flux J_v across these membranes. Due to the very small size of the drug molecules (≈ 1 nm ([76])) compared to the junction size of the endothelium (leaky junction size ≈ 20 nm) or the pore size of the IEL (≈ 150 nm), the osmotic reflection coefficient is very small ($\propto (r_{\text{mol}}/r_{\text{pore}})^2$), and the flux simplifies to ([55]):

$$J_{v,j} = \mathbf{n}_j \mathbf{u}_j = L_{p,j} \Delta p_j, \quad (2.5)$$

where $L_{p,j}$ is the hydraulic conductivity of the respective membrane. In the central region where endothelial cells do not hinder the fluid flow across the arterial wall, the matching condition simplifies to continuity of radial velocity ($u_1 = u_{\text{ses}}$). In all cases, the axial velocity at the lumen/arterial wall interface is set to zero ($w_1 = 0$). A zero axial pressure gradient is assumed normal to the upstream and downstream boundaries of the arterial wall layers resulting in no fluid flux across these boundaries and imposing a strictly radial flow field at these boundaries. This assumption is strictly valid in an axially homogeneous arterial wall; the upstream and downstream boundaries are sufficiently far from the therapeutic domain so that these boundary conditions have no effect on the results. On the adventitial boundary (outer boundary of the arterial wall), an excess pressure of $\tilde{p}_{\text{eel}} = 30$ mmHg is assumed.

2.2.3.2 Drug transport

Drug transport in the lumen is governed by the unsteady convection-diffusion equation:

$$\frac{\partial c_{\alpha,j}}{\partial t} + \text{Pe}_0 \mathbf{u}_{\alpha,j} \nabla c_{\alpha,j} = \nabla \cdot (D_{\alpha,j} \nabla c_{\alpha,j}). \quad (2.6)$$

Equation (2.6) describes the concentration $c_{\alpha,j}$ of a drug transported in the liquid phase (intrinsic drug concentration) with a non-dimensional diffusion coefficient $D_{\alpha,j}$ at a reference Peclet number Pe_0 (see Table 2.1). To describe mass transport in the porous arterial wall, averaging is required. Neglecting dispersion, superficial averaging (averaging over both phases of the porous medium containing the pore space and the solid tissue space) as described by Whitaker [193] yields the following macroscopic transport equation in the arterial wall (henceforth simply referred to as transport equation):

$$\frac{\partial c_j}{\partial t} + \Lambda_j \text{Pe}_0 \mathbf{u}_j \nabla c_j = \nabla \cdot (\mathbf{D}_j \nabla c_j) + R_j, \quad (2.7)$$

where the reaction term R_j accounts for drug flux to and from the tissue corresponding to the binding and unbinding of drug molecules to their binding sites in the arterial wall. The

two parameters that arise in the averaging process, the non-dimensional lag coefficient Λ_j and the effective non-dimensional diffusivity D_j , will be discussed later. For a pure fluid (porosity $\varepsilon = 1$), $\Lambda_j = 1$ and the effective diffusivity equals the diffusion coefficient $D_{\alpha,j}$ in the fluid (in our case, $D_{\alpha,1} = 1$ and $\mathbf{u}_{\alpha,1}$ is the velocity calculated from the Navier-Stokes equations in the lumen.) In this case the liquid concentration $c_{\alpha,j}$ equals the superficial average concentration c_j .

A general way of expressing the reaction term R_j is by:

$$R_j = -\frac{1}{f_{cb}} \frac{\partial b}{\partial t}, \quad (2.8)$$

which describes reaction as the negative of the rate of creation of bound drug concentration b as the drug binds to the porous material. The factor f_{cb} is defined as \tilde{c}_0/\tilde{b}_m , the ratio of the initial concentration \tilde{c}_0 in the stent polymer to the maximum binding site density \tilde{b}_{\max} . In recent literature two common ways of modeling drug uptake by arterial tissue can be found:

1. Equilibrium model: A simplified approach to model drug uptake assuming that the bound and free states are in a constant equilibrium [183, 200]. This assumption is valid when the binding and unbinding processes are fast compared to convection and diffusion and leads to:

$$R_j = (\kappa - 1) \frac{\partial c_j}{\partial t}, \quad (2.9)$$

where κ is the total binding coefficient.

2. Dynamic model: A second order model (discussed in detail in Section 2.2.4.1) that describes a saturating reversible binding process [179] treating bound drug as a dynamic variable:

$$\frac{1}{f_{cb}} \frac{\partial b}{\partial t} = \text{Da}_2^0 \left(c_j (1 - b) - \frac{1}{f_{cb} B_p} b \right) \quad (2.10)$$

with the reference Damköhler number Da_0 and the binding potential B_p . The baseline model in the present work uses this dynamic model to describe drug interaction with cells of the arterial wall; however, we also explore the ramifications of an equilibrium model assumption for the predictions of drug transport from DES.

The transport equations are subject to the following boundary conditions: zero drug concentration at the inlet boundary in the lumen. Because convection is dominant in the lumen, we set the outlet boundary condition to: $\Delta c = 0$. At the upstream and downstream boundaries of the arterial wall layers, a zero normal concentration gradient is prescribed. At the adventitial boundary, we investigated the following three different boundary conditions:

1. $c_m = 0$: considering the adventitia as a perfect sink.
2. $-\nabla (\mathbf{D}_m \nabla c_m) = 0$: assuming drug transport across the adventitia to be purely convective.
3. $J_{s,eel} = P_{eel} c_{\alpha,m} + \bar{c}_{\alpha,eel} J_{v,eel}$: modeling the external elastic lamina (EEL) as a Kedem-Katchalsky membrane assuming the drug concentration in the adventitia to be negligible.

We have verified that the choice of boundary condition has no significant effect on the parameters of interest. The baseline model uses the third option since it is considered the closest to the physiological situation.

At both the lumen-arterial wall interface and the SES-media interface, the Kedem-Katchalsky formulation is used to describe the concentration discontinuity across the thin endothelium and IEL:

$$J_{s,j} = -\mathbf{n}_j \left(\Lambda_j \text{Pe}_0 \mathbf{u}_j c_j - \mathbf{D}_j \nabla c_j \right) = P_j \Delta c_{\alpha,j} + s_j \bar{c}_{\alpha,j} J_{v,j}, \quad (2.11)$$

where P_j is the permeability of the respective interface and the local average liquid concentration $\bar{c}_{\alpha,j}$ is calculated as the weighted average concentration of the layer (for more details see Appendix A).

At the outer boundary of the stent polymer, drug flux continuity is prescribed:

$$J_{s,c} = -\mathbf{n}_c (\mathbf{D}_c \nabla c_c) = \mathbf{n}_j \left(\Lambda_j \text{Pe}_0 \mathbf{u}_j c_j - \mathbf{D}_j \nabla c_j \right). \quad (2.12)$$

Drug flux across the stent strut surface is zero, and the polymer is the only initial drug reservoir yielding the following initial condition:

- $\tilde{c}(\tilde{t} = 0) = \tilde{c}_0 = 100 \text{ mol m}^{-3}$ in the polymer.
- $c = 0$ elsewhere.

This initial concentration is representative for a high dose stent [152].

2.2.4 Determination of physiological parameters

Special attention was paid to the choice of the physiological parameters of the model. We use experimental data wherever available, complemented with values from fiber matrix and pore theory ([55] and references therein) when necessary. The solely tissue-dependent parameters, namely the hydraulic conductivity \tilde{L}_p , the porosity ε , the Darcy permeability \tilde{P}_D , and the properties of blood and plasma are well documented in the literature. All values with their respective sources are summarized in Table 2.2. Fluid density is assumed to be the same for plasma and whole blood with $\tilde{\rho} = 1060 \text{ kg m}^{-3}$. The hydraulic conductivities of the endothelium and IEL were calculated from $L_{p,j} = P_{D,j}/(\mu_p L_j)$ following the approach in [4] and [148]. In agreement with [55], the fiber matrix porosity and total porosity of the media were respectively set to

Table 2.2: Fluid model parameters

| Symbol | Unit | Lumen | ET | SES | IEL | Media |
|---------------|--------------------------------|------------------------------|---------------------------|---------------------------|---------------------------|---------------------------|
| $\tilde{\mu}$ | Pas | $3.5 \cdot 10^{-3}$ (a,b) | $7.2 \cdot 10^{-4}$ (a,b) | $7.2 \cdot 10^{-4}$ (a,b) | $7.2 \cdot 10^{-4}$ (a,b) | $7.2 \cdot 10^{-4}$ (a,b) |
| \tilde{P}_D | m^2 | N/A | $3.22 \cdot 10^{-21}$ (a) | $2.2 \cdot 10^{-16}$ (a) | $3.22 \cdot 10^{-19}$ (a) | $2.0 \cdot 10^{-18}$ (a) |
| \tilde{L}_p | $\text{m}^2 \text{ s kg}^{-1}$ | N/A | $2.2 \cdot 10^{-12}$ | N/A | $2.2 \cdot 10^{-9}$ | N/A |
| ε | – | 1 | $5 \cdot 10^{-4}$ (a) | 0.983 (d) | $4 \cdot 10^{-3}$ (a) | 0.25 (c) |
| \tilde{L} | μm | $\tilde{d}_1 = 3 \text{ mm}$ | 2 (a) | 10 (a) | 2 (a) | 500 (a) |

^a [4]

^b [148]

^c [55]

^d [79], [197], [92]

values without a reference are computed as presented in this section

$\varepsilon_{f,m} = 0.45$ and $\varepsilon_m = 0.25$, yielding a SMC fraction in the media of $\varepsilon_{SMC} = 1 - \varepsilon_m/\varepsilon_{f,m} = 0.44$, which agrees well with previous data [89].

The effective diffusivities for the different layers D_j , the lag coefficients Λ_j , the membrane permeabilities P_j and the sieving coefficients s_j depend on the interplay of the drug with the surrounding tissue. Here we will mainly focus on the diffusivities used in the model. The calculation of the remaining parameters can be found in Appendix A.

In the present study, we will consider the two DES drugs paclitaxel and sirolimus. Paclitaxel is a small hydrophobic agent with a molecular weight of $\tilde{M}_{PAX} = 853.9$ Da [105] and an average radius of $\tilde{r}_{mol}^{PAX} = 1.2$ nm [76]. Diffusion of paclitaxel in blood is reduced due to non-specific binding to blood proteins; therefore, the free diffusivity in plasma for paclitaxel is taken as the measured value in calf serum as determined in [114] $\tilde{D}_{free,p,PAX} = 20.3 \cdot 10^{-12} \text{ m}^2 \text{ s}^{-1}$. Using this value, the free diffusivity in whole blood is determined using the Stokes-Einstein equation as:

$$\tilde{D}_{free,b,PAX} = \frac{\tilde{\mu}_p}{\tilde{\mu}_b} \tilde{D}_{free,p,PAX} = 4.176 \cdot 10^{-12} \text{ m}^2 \text{ s}^{-1} . \quad (2.13)$$

The effective diffusivity D_j in Eq. (2.7) is a lumped parameter that arises from the averaging process of the diffusive term which accounts for the reduced transport of the solute on its tortuous path through the fibrous structure of the extracellular matrix. Apart from this passive effect, it can also account for an active reduction due to non-specific binding to the tissue of the arterial wall. No experimental work on the effective diffusivity in the SES is known to the authors. Given the assumptions of our model, we will consider the effective diffusion coefficient to be a simple scaling of the free diffusivity \tilde{D}_{free} by a factor that depends solely on material properties [192]. We will thus approximate the effective diffusivity as

$$\tilde{D}_{eff,f,j} = \tilde{D}_{free} \exp \left(- \left(1 - \varepsilon_{f,i} \right)^{\frac{1}{2}} \left(1 + \frac{\tilde{r}_{mol}}{\tilde{r}_f} \right) \right) , \quad (2.14)$$

where \tilde{r}_{mol} is the average radius of the drug molecule and \tilde{r}_f is the average radius of the fibers of the extracellular matrix. Levin *et al.* [105] determined experimentally anisotropic effective bulk diffusion coefficients for paclitaxel, corresponding to the diffusivities in the media of the arterial wall. These measurements suggest a very high anisotropy between radial and axial diffusivities with $D^z/D^r \approx 1000$. The work conducted in [81] suggests an anisotropy between radial and circumferential diffusivities in the media of $D^z/D^r \approx 10$. The structure of the media as investigated in [136] suggests that the circumferential and axial diffusion coefficients are of the same order of magnitude, whereas the diffusion coefficient in the radial direction is significantly smaller. Therefore, in our baseline model, we assume the axial and circumferential effective diffusivities to be of a comparable order of magnitude [188] and $D^z/D^r = 10$. Because the importance of anisotropic diffusion has been highlighted in [80], we will explicitly investigate the effect of different anisotropies. A summary of all coefficients for the transport of paclitaxel can be found in Table 2.3.

Similar to paclitaxel, sirolimus is a small hydrophobic drug that binds to the FKBP12 receptor of SMCs and endothelial cells. To calculate the transport properties of sirolimus, we applied the same procedure as described for paclitaxel. Due to the slightly larger molecular weight of $\tilde{M}_{SIR} = 914.2$ Da [105], the Stokes-Einstein radius and blood plasma diffusivity need to be adjusted (details in Appendix A). All transport coefficients for sirolimus are summarized in Table 2.3.

It can be readily seen that the diffusivities of paclitaxel and sirolimus are not very different. Rather, the primary difference between the two drugs stems from differences in their reaction

Table 2.3: Transport model parameters for paclitaxel (upper part) and sirolimus (lower part)

| Drug | Symbol | Unit | Lumen | ET | SES | IEL | Media |
|------------|---------------|----------------------------|----------------------|---------------------|-----------------------|---------------------|--------------------------------|
| Paclitaxel | Λ | – | 1 | N/A | 1.02 | N/A | 3.4 |
| | s | – | N/A | 0.86 | N/A | 1.0 | N/A |
| | \tilde{P} | m s^{-1} | N/A | $3 \cdot 10^{-6}$ | N/A | $9.8 \cdot 10^{-6}$ | N/A |
| | \tilde{D}^r | $\text{m}^2 \text{s}^{-1}$ | $4.2 \cdot 10^{-12}$ | N/A | $1.7 \cdot 10^{-11}$ | N/A | $2.0 \cdot 10^{-(11+n)}$ (a,b) |
| | \tilde{D}^z | $\text{m}^2 \text{s}^{-1}$ | $4.2 \cdot 10^{-12}$ | N/A | $1.7 \cdot 10^{-11}$ | N/A | $5.0 \cdot 10^{-11}$ (a) |
| Sirolimus | Λ | – | 1 | N/A | 1.02 | N/A | 3.4 |
| | s | – | N/A | 0.855 | N/A | 1.0 | N/A |
| | \tilde{P} | m s^{-1} | N/A | $3.6 \cdot 10^{-6}$ | N/A | $9.6 \cdot 10^{-6}$ | N/A |
| | \tilde{D}^r | $\text{m}^2 \text{s}^{-1}$ | $4.1 \cdot 10^{-12}$ | N/A | $1.67 \cdot 10^{-11}$ | N/A | $7.0 \cdot 10^{-(11+n)}$ (a,b) |
| | \tilde{D}^z | $\text{m}^2 \text{s}^{-1}$ | $4.1 \cdot 10^{-12}$ | N/A | $1.67 \cdot 10^{-11}$ | N/A | $4.0 \cdot 10^{-11}$ (a) |

^a [105]^b $n = 1, 2, 3$

values without a reference are computed as presented in this section

kinetics. More specifically, sirolimus binds and unbinds significantly more rapidly than paclitaxel as seen in Table 2.4 (discussed in more detail in Section 2.2.4.1). The diffusion coefficient in the stent polymer coating is the result of an interplay of several factors including the polymer matrix, the drug, and the stent platform release kinetics. Balakrishnan et al. [12] showed that simple diffusion is appropriate to model this complex process. Reported values for diffusion coefficients range from $\tilde{D}_c = 1 \cdot 10^{-13} \text{ m}^2 \text{ s}^{-1}$ [183] down to $\tilde{D}_c = 1.5 \cdot 10^{-17} \text{ m}^2 \text{ s}^{-1}$, representing the range from fast to slow release kinetics. The baseline configuration in this study assumes a drug diffusivity in the polymer at the fast release end of this range ($\tilde{D}_c = 1 \cdot 10^{-13} \text{ m}^2 \text{ s}^{-1}$).

2.2.4.1 Time scales and dimensionless quantities for drug transport

In order to better interpret the results, it is useful to analyze the time scales introduced by the full reaction model (Eq. (2.10)) and compare them to the other time scales in the transport equation (Eq. (2.7)). Considering the dimensional form of Equation (2.10):

$$\frac{\partial \tilde{b}}{\partial \tilde{t}} = (1 - \varepsilon_j)^{-1} \tilde{k}_f \tilde{c}_j (\tilde{b}_{\max} - \tilde{b}) - \tilde{k}_r \tilde{b}, \quad (2.15)$$

Table 2.4: Non-equilibrium reaction model parameters for paclitaxel and sirolimus [179]

| Drug | Da_2 | $B_p = \frac{\tilde{b}_{\max}}{(1 - \varepsilon_j) \tilde{K}_d}$ | $\tilde{K}_d = \frac{\tilde{k}_r}{\tilde{k}_f} (\text{mol m}^{-3})$ | $\tilde{b}_{\max} (\text{mol m}^{-3})$ |
|------------|----------------|--|---|--|
| Paclitaxel | 2700 | 41 | $3.1 \cdot 10^{-3}$ | 0.127 |
| Sirolimus | $5 \cdot 10^4$ | 139 | $2.6 \cdot 10^{-3}$ | 0.366 |

the first term on the right hand side (RHS) represents drug binding to sites in the arterial wall which requires the presence of both free drug and free binding sites. The binding rate is additionally controlled by the forward reaction coefficient \tilde{k}_f and the porosity ε_j of the tissue. Thus, the characteristic time scale for drug binding is:

$$\tilde{t}_f = \frac{(1 - \varepsilon_j)}{\tilde{k}_f \tilde{b}_{\max}}. \quad (2.16)$$

The second term on the RHS of Equation (2.15) describes the drug unbinding due to the assumed reversible nature of the reaction. The typical time scale characterizing this process is determined by the reverse reaction rate \tilde{k}_r :

$$\tilde{t}_r = \frac{1}{\tilde{k}_r}. \quad (2.17)$$

The ratio of the forward to reverse reaction coefficients $\tilde{K}_d = \tilde{k}_r/\tilde{k}_f$ is the equilibrium dissociation constant [179] and characterizes the overall affinity of the drug to its binding sites with low values corresponding to high affinity.

We would now like to compare the time scales of drug binding and unbinding to those of drug convection and diffusion. The typical flow velocity in the arterial wall is very different from that in the lumen. The characteristic (radial) convective flow velocity in the arterial wall can be written as:

$$\tilde{u}_w = \frac{\tilde{p}_{\text{out}} - \tilde{p}_{\text{eel}}}{\tilde{\mu}_p \tilde{H}_w} = 1.5 \cdot 10^{-8} \text{ m s}^{-1} \quad (2.18)$$

with

$$\tilde{H}_w = \sum_j \frac{\tilde{L}_j}{\tilde{p}_{D,j}}, \quad (2.19)$$

with j summed over the endothelium, SES, and media. With this we can now calculate the typical time scale for convection in the media as

$$\tilde{t}_C = \frac{\tilde{L}_m}{\Lambda_m \tilde{u}_w} \quad (2.20)$$

and for diffusion

$$\tilde{t}_D = \frac{\tilde{L}_m^2}{\tilde{D}_m^r}. \quad (2.21)$$

To weigh the relative importance of these various processes, we form the following three dimensionless quantities:

- Peclet number Pe : ratio of diffusion time scale to convection time scale,
- First Damköhler number Da_1 : ratio of convection time scale to forward reaction time scale,
- Second Damköhler number Da_2 : ratio of diffusion time scale to forward reaction time scale.

The resulting computed time scales and dimensionless quantities, summarized in Table 2.5 (the different magnitude of the second Damköhler number compared to [179] stems from the adapted length scale (\tilde{L}_m) and diffusivity (\tilde{D}_m^r) used), indicate that due to differences in their reaction properties, paclitaxel and sirolimus concentration profiles in the arterial wall may be very different despite the fact that both drugs have largely similar transport properties. For both drugs, convection and binding clearly dominate diffusion. The major difference in the two drugs lies in the relative importance of convection compared to reaction: sirolimus' binding rate is so high that it even dominates the convective transport ($Da_1 \gg 1$), whereas paclitaxel is more sensitive to convection ($Da_1 < 1$). This table reveals an additional important time scale for the transport problem, namely the release time from the stent, which approximates the time over which the stent effectively releases its drug load from the polymer coating. Thus, for the baseline stent, fresh drug supply only lasts for several hours.

The two Damköhler numbers defined above compare the initial maximum reaction rate to the rates of convection and diffusion. This is adequate when considering a first-order reaction process but is limited in its informative value when the reaction is second-order and is reversible. To get a more comprehensive view of the binding and unbinding process, we define an integral time-dependent first Damköhler number which compares the averaged magnitude of the reaction term to that of the convection term in the media at each time point:

$$Da_{\text{int}}(t) = Da_1 \frac{\int_{V_m} \left(c_m(1-b) + \frac{b}{f_{cb}B_p} \right) dV}{\int_{V_m} c_m dV}. \quad (2.22)$$

$Da_{\text{int}}(t)$ thus estimates the relative importance of reaction to convection in the media over time.

2.2.4.2 One-layer approximation

Due to the small thickness of the intima compared to the media, it is tempting to simplify the problem and represent the intima as a single Kedem-Katchalsky matching condition. Consequently, the arterial wall would consist of a single porous layer representing the media. We wanted to probe the validity of this assumption and to compare the results of the one-layer

Table 2.5: Time scales and dimensionless quantities for the stented part of the media for paclitaxel and sirolimus

| Drug | Convection time (h) | Diffusion time (h) | Binding time (h) | Unbinding time (h) | Stent emptying time ^(a) (h) | Peclet number | 1 st Damköhler number | 2 nd Damköhler number |
|------------|---|---|--|---------------------------------------|---|--|--|--|
| | $\tilde{t}_C = \frac{\tilde{L}_m}{\Lambda_m \tilde{u}_w}$ | $\tilde{t}_D = \frac{\tilde{L}_m^2}{\tilde{D}_m^r}$ | $\tilde{t}_f = \frac{(1-\varepsilon_j)}{\tilde{k}_f \tilde{b}_{\text{max}}}$ | $\tilde{t}_r = \frac{1}{\tilde{k}_r}$ | $\tilde{t}_E = \frac{\pi \tilde{L}_c^2}{4 \tilde{D}_c}$ | $Pe^r = \frac{\tilde{t}_D}{\tilde{t}_C}$ | $Da_1 = \frac{\tilde{t}_C}{\tilde{t}_f}$ | $Da_2 = \frac{\tilde{t}_D}{\tilde{t}_f}$ |
| Paclitaxel | 2.8 | 34.7 | 5.1 | 210.7 | 5.5 | 13.0 | 0.5 | 6.75 |
| Sirolimus | 2.8 | 9.9 | 0.08 | 11.2 | 5.5 | 3.7 | 34 | 125.0 |

^a [186]: assuming the stent elutes into a perfect sink surrounding

model to those of our baseline two-layer model. To generate the equivalent effective hydraulic conductivities for the matching boundary condition with and without endothelial coverage, we reinterpreted the different layers involved (endothelium, SES, and IEL) as flow resistances in series [148] and used the total resistance to obtain an effective hydraulic conductivity as:

$$L_{p,\text{eff}} = \left(\mu_p \sum_j \frac{L_j}{P_{D,j}} \right)^{-1}. \quad (2.23)$$

For the effective parameters for solute transport, we choose the same values as for the endothelium in the non-denuded case and those of the IEL in the denuded case, since these correspond to the largest resistance to transport.

2.2.5 Numerical methods

The governing equations are discretized by means of the finite element method (FEM) using the commercial software package COMSOL Multiphysics 4.3 (COMSOL AB, Burlington, MA, USA). The following types of elements are used:

- Momentum transport: third-order Lagrangian elements for the velocity and second-order Lagrangian for the pressure (P3-P2)
- Drug transport: second-order Lagrangian elements
- Reaction equation: second-order discontinuous Lagrangian elements

The tolerance threshold for the relative error of the solution (relative tolerance) of the momentum equations was set to 10^{-9} . An analysis of the transport problem showed no change of the solution below a combination of relative tolerance 10^{-3} and absolute tolerance 10^{-4} . The computational domain of the momentum equations was extended beyond that of the drug transport to ensure insensitivity of the results to the inflow and outflow boundary conditions. The time advancing scheme is a backward differentiation formula (BDF) with variable order and time step size [77]. The maximum time step size is restricted to 1 hour (h). Reducing the maximum time step to $1/8$ h did not change the solution, validating our choice for the maximum step size.

The minimum mesh element size is set to two times the concentration boundary layer thickness $\tilde{\delta}_c$ as estimated by $\tilde{\delta}_c \approx 2\sqrt{3}\tilde{d}_h\text{Re}_d^{-1/2}\text{Sc}_b^{-1/3}$ using the Reynolds number Re_d based on the hydrodynamic stent diameter \tilde{d}_h and the Schmidt number in blood Sc_b [183]. We note that $\text{Re}_d = \text{Re}_0$ in this particular case, since the reference length and velocity scales used to non-dimensionalize the governing equations are the same as the length and velocity scales used to compute Re_d . The mixed triangular and quadrilateral mesh (Fig. 2.1) is enhanced with boundary layer elements (BLE) at the interface between luminal flow and arterial wall and at the interface of the stent polymer coating with the arterial wall. To smoothen the sharp initial condition from the stent polymer to the surrounding domain, the inner boundary of the triangular polymer mesh is enhanced with BLEs and the initial condition itself transitions from $c(t=0) = 1$ to $c(t=0) = 0$ using an infinitely differentiable step function. The classical approach of a mesh independence study [5] determined the number of elements in the lumen, the SES and in the polymer. We consecutively increased the number of mesh elements in each of these layers by a factor of 1.5 to 2 until the time evolution of the average concentration

in the SES and the polymer showed a relative difference of less than 1% from one mesh iteration to another. Similarly, we used the average wall shear stress along the lumen-wall interface and the flow profile downstream of the stent as the test quantities to verify grid independence in the lumen. In the media, however, the maximum cell size was limited by the occurrence of spurious oscillations in the solution. This resulted in an overall very fine mesh with approximately 290 000 elements. Computation time for the baseline simulation performed on 4 cores of an Intel[®] Xeon[®] CPU X5680 @ 3.33GHz processor is about 1 h.

2.3 Results

2.3.1 Baseline model

To capture the global predictions of the baseline model, we compute the spatially averaged normalized mean concentration (NMC) of the eluted drug in each of the layers (j) of the arterial wall. The NMC at any instant in time is defined as follows:

$$\text{NMC}_j(t) = \frac{1}{V_j} \int_{V_j} \left(c_j(\mathbf{x}, t) + \frac{b_j(\mathbf{x}, t)}{f_{cb}} \right) dV . \quad (2.24)$$

In the case of the one-layer model (OLM), the theoretical subendothelial space (SES) NMC can be calculated from:

$$\text{NMC}_{\text{ses}}(t) = \frac{1}{\Gamma_{\text{ses}}} \int_{\Gamma_{\text{ses}}} \varepsilon_{\text{ses}} \bar{c}_{\alpha, \text{ses}}(s, t) d\Gamma . \quad (2.25)$$

Figure 2.2 shows simulation results for the baseline model eluting paclitaxel from the stent coating at the fastest rate of the presented range. Representative for the entire stent, Fig. 2.2 A compares the total drug concentration (i.e. bound drug b plus free drug c) distribution in the upstream region of the therapeutic domain up to the first two stent struts. The three time points after stent implantation shown are: $\tilde{t} = 50$ min, which corresponds to the time of maximum NMC in the media; $\tilde{t} = 1$ day(d); and $\tilde{t} = 7$ d post implantation. At $\tilde{t} = 50$ min,

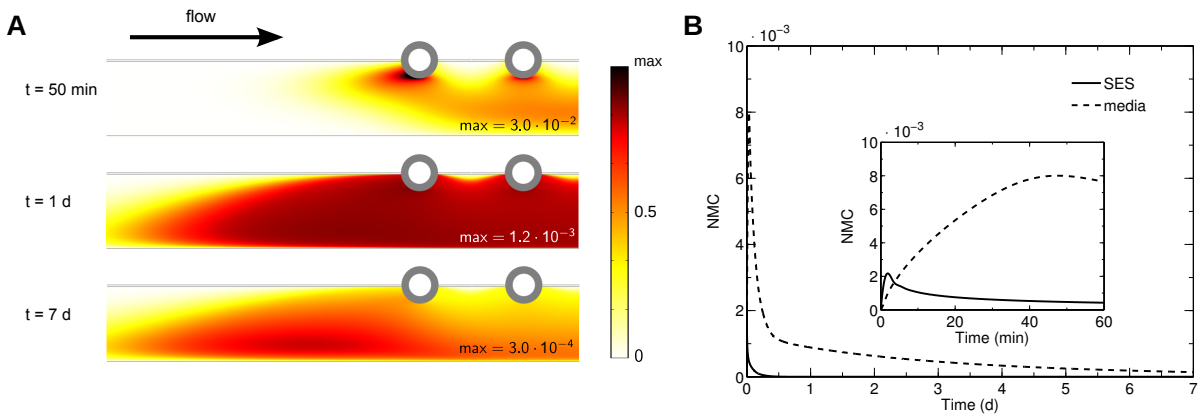


Figure 2.2: Baseline simulation (paclitaxel). **A:** Normalized concentration (NC) distribution in the media and the SES at three different time points: $\tilde{t} = 50$ min, $\tilde{t} = 1$ d, and $\tilde{t} = 7$ d post stenting. **B:** Temporal evolution of the normalized mean concentration (NMC) in the SES and the media.

the drug has already completely invaded the arterial wall. From the second strut onwards, a symmetric drug distribution pattern surrounds the struts. The concentration is highest close to the struts and is relatively low close to the lumen between the stent struts. The concentration field around the first strut is asymmetric and skewed upstream. This is due to the fact that the endothelium is denuded between the stent struts but intact upstream of the stent. Crossing the intact endothelium the pressure drops by more than 50% from the lumen to the arterial wall while in between struts, the pressure drop is virtually negligible. Thus, convection is higher in between struts than at the upstream and downstream end of the stent, creating a recirculation zone around the strut that distorts the symmetry in the concentration distribution.

Over the course of the next few days, the concentration distribution pattern homogenizes in the media while the SES rapidly empties of drug. After one day, the concentration level in the media has already dropped by an order of magnitude compared to the maximum concentration. This is due to the fact that the fast-release kinetics of the baseline stent has already emptied the entire drug supply at this point. After a week, the maximum concentration in the therapeutic domain has dropped by two orders of magnitude. The radial concentration distribution is now skewed towards the adventitia (rather than the intima) while a small concentration reservoir has formed upstream of the stent where convective transport forces are not as strong because the endothelium is not denuded.

Figure 2.2 B depicts the temporal evolution of the spatially averaged NMC in the SES and media. Peak concentration in the SES occurs minutes after stent implantation and attains only a quarter of the peak concentration in the media. Within the first day, the drug vanishes from the SES. The high concentration in the media ($\approx 8 \cdot 10^{-3}$) is followed by a rapid drop within the following 12 h to an NMC of $1 \cdot 10^{-3}$, which corresponds well to the value of the maximum binding site density of paclitaxel ($b_{\max} = 0.127$). The decrease then slows down considerably for the remainder of the week.

2.3.2 Sensitivity analysis of the model

In light of the uncertainty in some of the transport model parameters, we studied the sensitivity of the baseline results to the drug diffusivity coefficients in the SES and the media while maintaining the first Damköhler number constant. Given that all equations are non-dimensional, the analysis is presented in terms of the sensitivity of the NMC to the Peclet number in the different layers:

$$\text{Pe}_j^i = \frac{\tilde{u}_w L_0}{\tilde{D}_j^i} . \quad (2.26)$$

Figure 2.3 illustrates the sensitivity of the model results to the Peclet number in the SES as well as to the radial and axial Peclet number in the media. We have selected two different parameters to measure the sensitivity of the model: 1) the magnitude of the peak NMC in the SES and in the media (Fig. 2.3 A, C, E) and 2) the ratio of the NMC after one day, 5 days and 7 days compared to the maximum value (Fig. 2.3 B, D, F); this retention coefficient quantifies the drop following maximum concentration in the media.

Varying the Peclet number in the SES over several orders of magnitude has a fairly small effect on the concentration levels in the SES and media (Fig. 2.3 A). More specifically, varying the SES Peclet number over 4 orders of magnitude leads to an increase in the maximum NMC of $\approx 55\%$ in the SES and only $\approx 10\%$ in the media. The retention coefficient at one day changes only by 6% (Fig. 2.3 B). The NMC in the wall is more sensitive to a variation of the radial

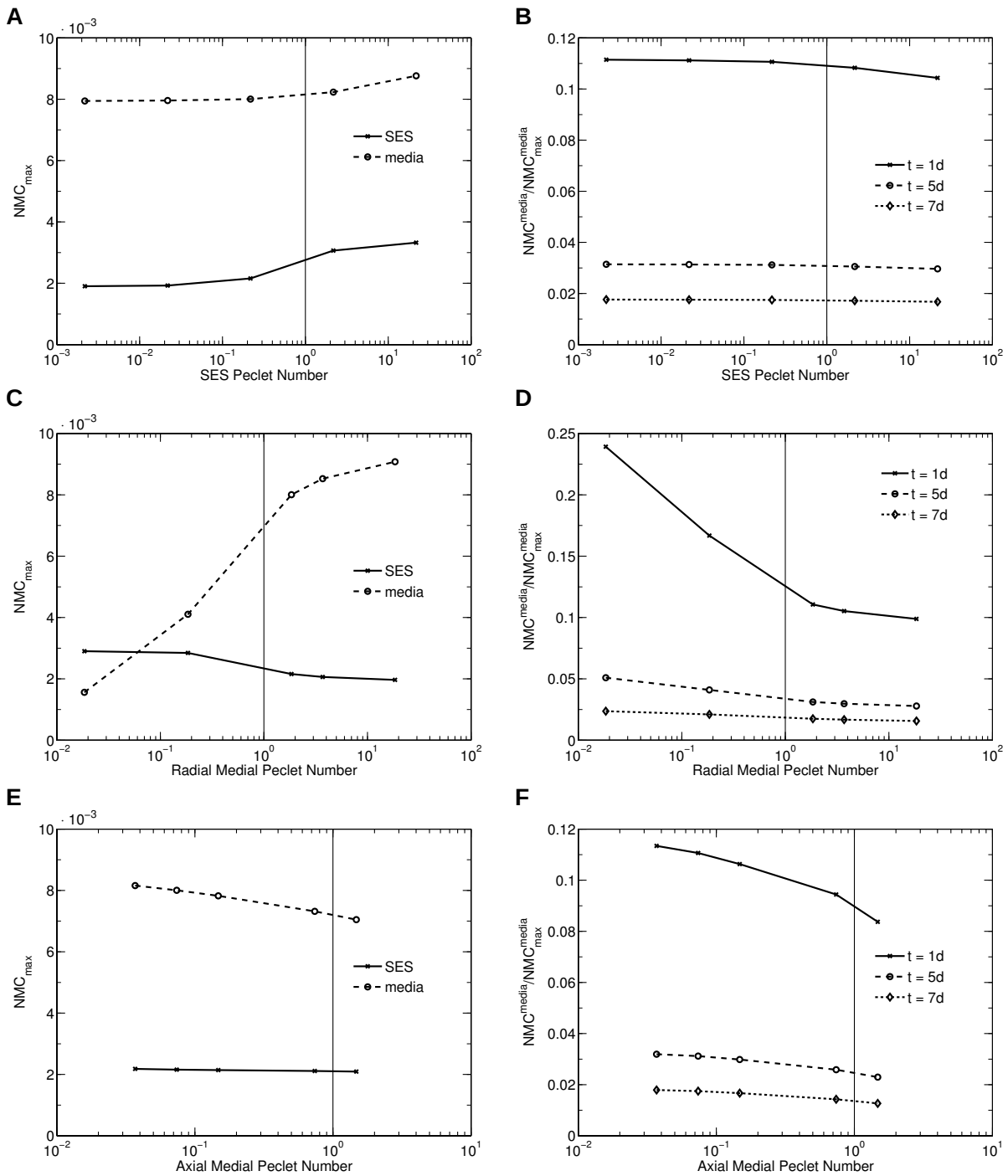


Figure 2.3: Sensitivity analysis (paclitaxel). Dependence of maximum NMC in the SES and media on **A**: SES Pecllet number, **C**: radial medial Pecllet number, and **E**: axial medial Pecllet number. Dependence of retention coefficient at three different time points ($\tilde{t} = 1$ d, $\tilde{t} = 5$ d, and $\tilde{t} = 7$ d post stenting) on **B**: SES Pecllet number, **D**: radial medial Pecllet number, and **F**: axial medial Pecllet number.

Peclet number in the media (Fig. 2.3 C and D). While the peak NMC in the SES changes by only a moderate 32%, the peak concentration in the media changes by $\approx 300\%$. The highest sensitivity is observed as one goes from $Pe_m^r = 0.02$ to $Pe_m^r = 0.2$. With the peak concentration increasing, the retention coefficient at one day decreases by 75% over the entire Pe_m^r range. Here, too, the majority of the variation occurs in the $Pe_m^r < 1$ domain. The retention coefficients at 5 and 7 days decrease by more moderate values of $\approx 45\%$ and $\approx 34\%$, respectively.

The NMC in the SES appears to be largely insensitive to the axial Peclet number in the media (Fig. 2.3 E), whereas the medial NMC is weakly affected, with a $\approx 14\%$ total decrease over a two order-of-magnitude change in Pe_m^z . The retention coefficients for all three time points decrease by $\approx 30\%$. Interestingly, in all cases the retention coefficients at 5 and 7 days (Fig. 2.3 B, D, F) are less sensitive to Peclet number variations than the day one retention values, implying that the long term evolution is affected differently than the short term.

A value commonly used in computational models for the medial porosity is $\varepsilon_m = 0.25$. However, the porosity of the media largely depends on its state of health. With the fiber matrix porosity of the media fixed at $\varepsilon_{f,m} = 0.45$, we varied the ε_m in the range of 0.1 – 0.4 so that the model remains consistent with its definition of the fraction of SMCs (ε_{SMC}). Fig. 2.4 depicts the sensitivity of the peak concentrations in the SES and the media (Fig. 2.4 A) and the retention coefficient in the media (Fig. 2.4 B) to ε_m . The SES concentration is unaffected by the medial porosity; however, the maximum NMC in the media more than doubles in the considered ε_m interval. Accordingly the magnitude of the drop at one day increases by 38%. Drug retention at 5 and 7 days is largely unaffected by the porosity variations.

Changing the luminal Reynolds number in the physiological range ($Re_l \in [100, 800]$) reveals a significant dependence of the concentration evolution in the SES on blood flow in the lumen (Fig. 2.5). The maximum NMC in the SES decreases significantly (more than 85%) with increasing Reynolds number; however, consistent with previous results [128], the maximum total NMC in the media is only weakly affected.

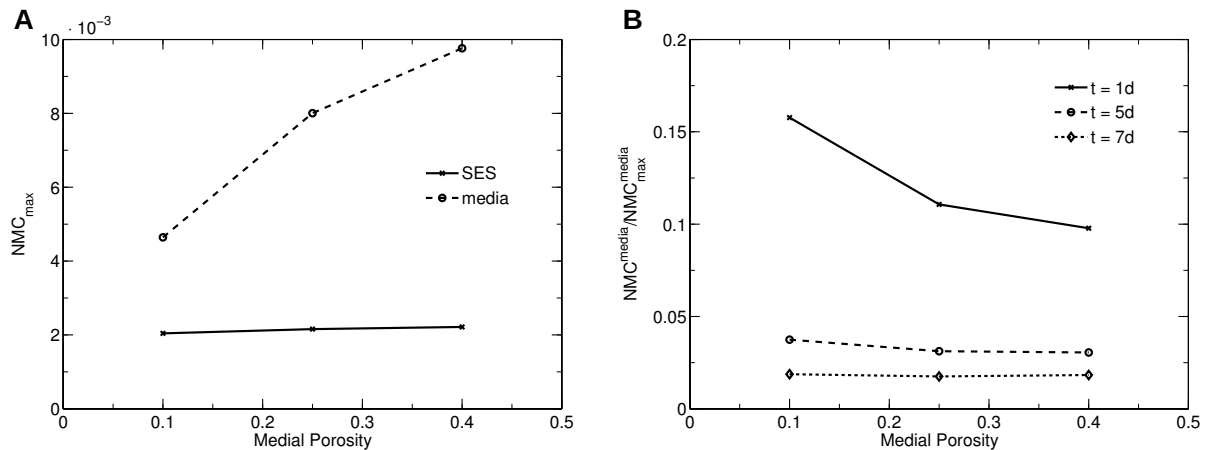


Figure 2.4: Sensitivity analysis (paclitaxel). **A:** Dependence of maximum normalized mean concentration (NMC) in the subendothelial space (SES) and media on medial porosity. **B:** Dependence of the retention coefficient at three different time points: $\tilde{t} = 1$ d, $\tilde{t} = 2$ d, and $\tilde{t} = 7$ d post stenting on medial porosity.

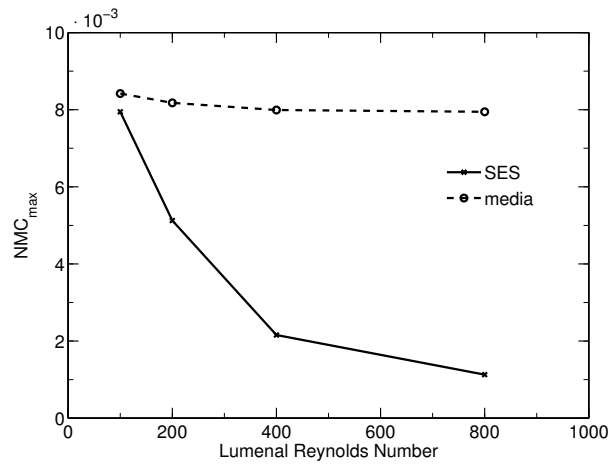


Figure 2.5: Sensitivity analysis (paclitaxel). Dependence of the maximum NMC in the SES and media on Reynolds number in the lumen.

2.3.3 Effect of one-layer modeling

It is currently common in DES modeling to treat the arterial wall as a single layer with homogenized transport properties mostly representing the media. However, it was shown in [80] that the layered structure of the arterial wall can affect the deposition and distribution of drugs. Figure 2.6 illustrates the differences in the concentration distribution occurring when a one-layer model (OLM) is used instead of the two-layer model (TLM). To amplify the effects, we have reduced the total strut size of the baseline with a diameter of $d_s = 250 \mu\text{m}$ to a diameter of $d_s = 150 \mu\text{m}$ (representing a second generation DES strut) and considered a case where the SES is thickened by a factor of three compared to the baseline situation due to the development of atherosclerosis. Figure 2.6 shows the superimposed flow and drug concentration field around the first strut of the stent. Both the TLM and OLM predict a back flow pattern around the first strut; however, the TLM predicts a more pronounced back flow whereby the back flowing fluid

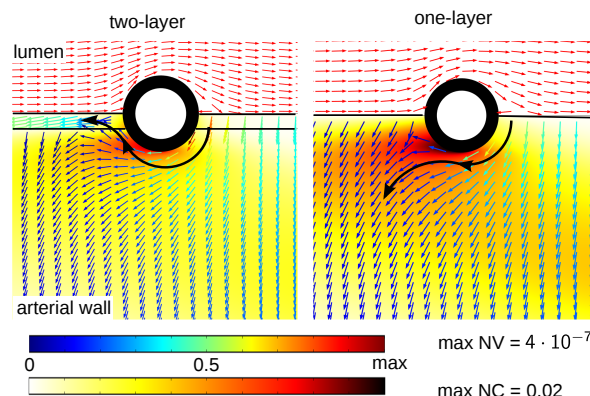


Figure 2.6: One-layer vs. two-layer modeling (paclitaxel). Normalized velocity (NV) and normalized concentration (NC) field around the first stent strut for a situation where the SES has been thickened by a factor of 3 and the total stent strut size has been decreased to $150 \mu\text{m}$. Time shown is the point of maximum concentration in the media.

enters the SES, while the OLM is incapable of capturing this characteristic flow feature. We can also see that the local changes in the flow field affect the concentration distribution and magnitude close to the stent strut.

Fig. 2.7 compares the OLM and TLM predictions for the NMC in the SES and in the media for the baseline model. Using equation (2.25) recovers the qualitative temporal evolution of the NMC in the SES. However, the peak concentration is underestimated by about 30%, and this offset continues to grow to $\approx 100\%$ at 2 hours post implantation. For a “diseased” configuration with a three-fold thickened SES, the differences between the TLM and OLM become yet more pronounced, and the peak concentration is underestimated by 100%. In the media, the agreement is very good qualitatively and quantitatively. Here also the discrepancies grow when the SES thickness is increased.

2.3.4 Effect of reaction modeling

We wished to establish if an equilibrium reaction model adequately represents drug transport in the arterial wall. Fig. 2.8 compares the temporal evolution of the total concentration (NMC) in the media for the reversible binding reaction model to the case where free and bound drug are assumed to be in a constant equilibrium. Using an equilibrium assumption, the very early behavior predicted by the non-equilibrium model can be qualitatively recovered. However, the peak concentration predicted by the equilibrium model occurs considerably later and is significantly higher compared to the reversible binding model. For the commonly used value of $\kappa = 20$ [183], the peak concentration is ≈ 3 times higher than that predicted by the dynamic reversible reaction model and occurs ≈ 9 h later. With increasing κ , the peak becomes progressively higher and is predicted to occur later. In all cases including the dynamic reaction model, the arterial wall becomes completely void of drug within a week of stent implantation. The emptying time is quicker for smaller values of κ .

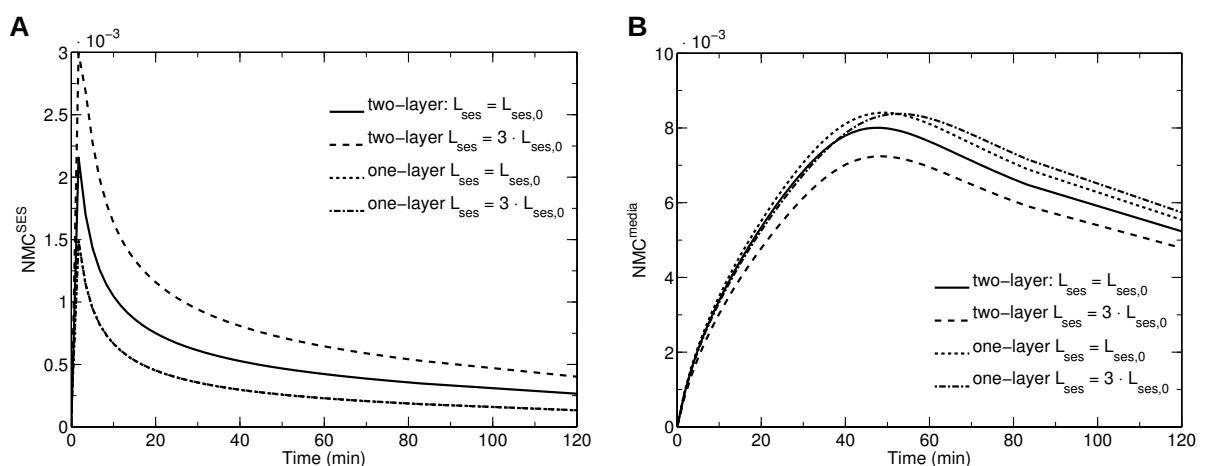


Figure 2.7: One-layer vs. two-layer modeling (paclitaxel). NMC for two different SES thicknesses ($L_{ses} = L_{ses,0}$ and $L_{ses} = 3L_{ses,0}$) **A**: in the SES (both predictions of the OLM collapse onto one curve) **B**: in the media.

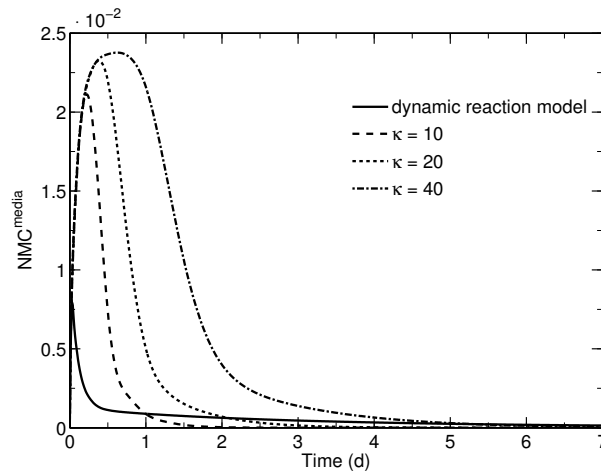


Figure 2.8: Temporal evolution of the total NMC in the media as predicted by a reversible binding reaction model (baseline model) compared to an equilibrium model for different values of the total binding coefficient κ .

2.3.5 Effect of the choice of drug

All results presented thus far focused on paclitaxel. Another common drug used in DES is sirolimus. Although different in their mode of action in preventing smooth muscle cell (SMC) proliferation and migration [60], sirolimus and paclitaxel have similar transport properties (see Table 2.3). With a binding potential $B_p > 40$, both drugs fall in the category of strongly retained drugs [179].

Figure 2.9 compares the distribution of the bound drug fraction (b) in the upstream region of the therapeutic domain for paclitaxel and sirolimus at the time of maximum total NMC in the media ($\tilde{t} = 50$ min) and one day after stent implantation. Within the first hour binding has occurred over the entire width of the arterial wall for both drugs. Binding is maximal close to the stent struts and drops gradually with distance away from the polymer. The concentration

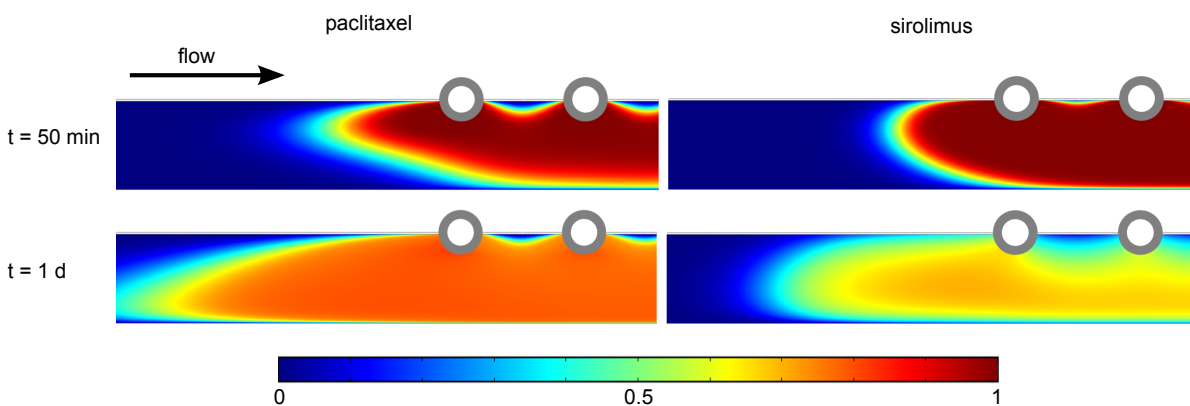


Figure 2.9: Paclitaxel vs. sirolimus. Bound drug fraction b at two different time points: $\tilde{t} = 50$ min (first row) and $\tilde{t} = 1$ d (second row).

gradient is sharper in the case of sirolimus. For paclitaxel, there is a region near the luminal surface in between the struts where little drug binding occurs; such a region exists but is considerably smaller in the case of sirolimus. At one day, the binding pattern has spread further upstream. Interestingly, paclitaxel has invaded a larger portion of the upstream therapeutic domain than sirolimus, although the axial diffusion coefficient of sirolimus is larger. These observations underscore the more convection-dominated transport of paclitaxel compared to sirolimus. Following the emptying of the stent, the unbinding process becomes the dominant effect: the binding fraction in the case of paclitaxel drops to $\approx 70\%$ on average while the equivalent value for sirolimus is $\approx 60\%$.

Fig. 2.10 compares drug transport characteristics for stents loaded with either paclitaxel or sirolimus for the baseline fast-release case (panels A, C and E) and for the case of a slow-release stent (panels B, D and F). Figures 2.10 A and C demonstrate that for the fast-release stent, the differences between paclitaxel and sirolimus are rather minor. Peak concentration magnitude and timing in the SES and media are comparable. The one difference is the slower drop following peak concentration in the media in the case of sirolimus compared to paclitaxel: for paclitaxel the drop to 25% of the peak average concentration takes ≈ 6 h while for sirolimus the same drop almost requires one day.

The slow-release stent is geometrically identical to the fast-release stent; only the diffusion coefficient in the polymer coating has been reduced by three orders of magnitude to $\tilde{D}_c = 1 \cdot 10^{-16} \text{ m}^2/\text{s}$. When comparing the concentration profiles for the two drugs in the SES (Fig. 2.10 B) and media (Fig. 2.10 D) for the slow-release stent, a very different picture emerges: while the qualitative behavior for both drugs remains similar, the concentration levels of sirolimus are continuously above those of paclitaxel. At peak concentration in the SES, the NMC of sirolimus is $\approx 50\%$ higher than that of paclitaxel. This discrepancy grows to more than 100% at 8 weeks. The peak concentration of sirolimus in the media is three times the peak concentration of paclitaxel, and after 8 weeks the NMC remains more than twice as high.

Figures 2.10 E and F compare the time-evolution of the integral Damköhler number for both drugs for the fast-release and slow-release stent platforms. In the fast-release case, paclitaxel begins in the convection-dominated regime ($Da_{\text{int}} < 1$) and after the first half day transitions into a slightly more binding-dominated regime. The transition is faster for sirolimus since with the exception of the first few hours after the beginning of drug elution, the transport of sirolimus is dominated by the binding and unbinding process. For the slow-release stent, the balance of convective and reactive terms is less variable: paclitaxel remains in a regime where convection and binding/unbinding are of comparable importance, whereas sirolimus is clearly dominated by the binding/unbinding process over the entire time.

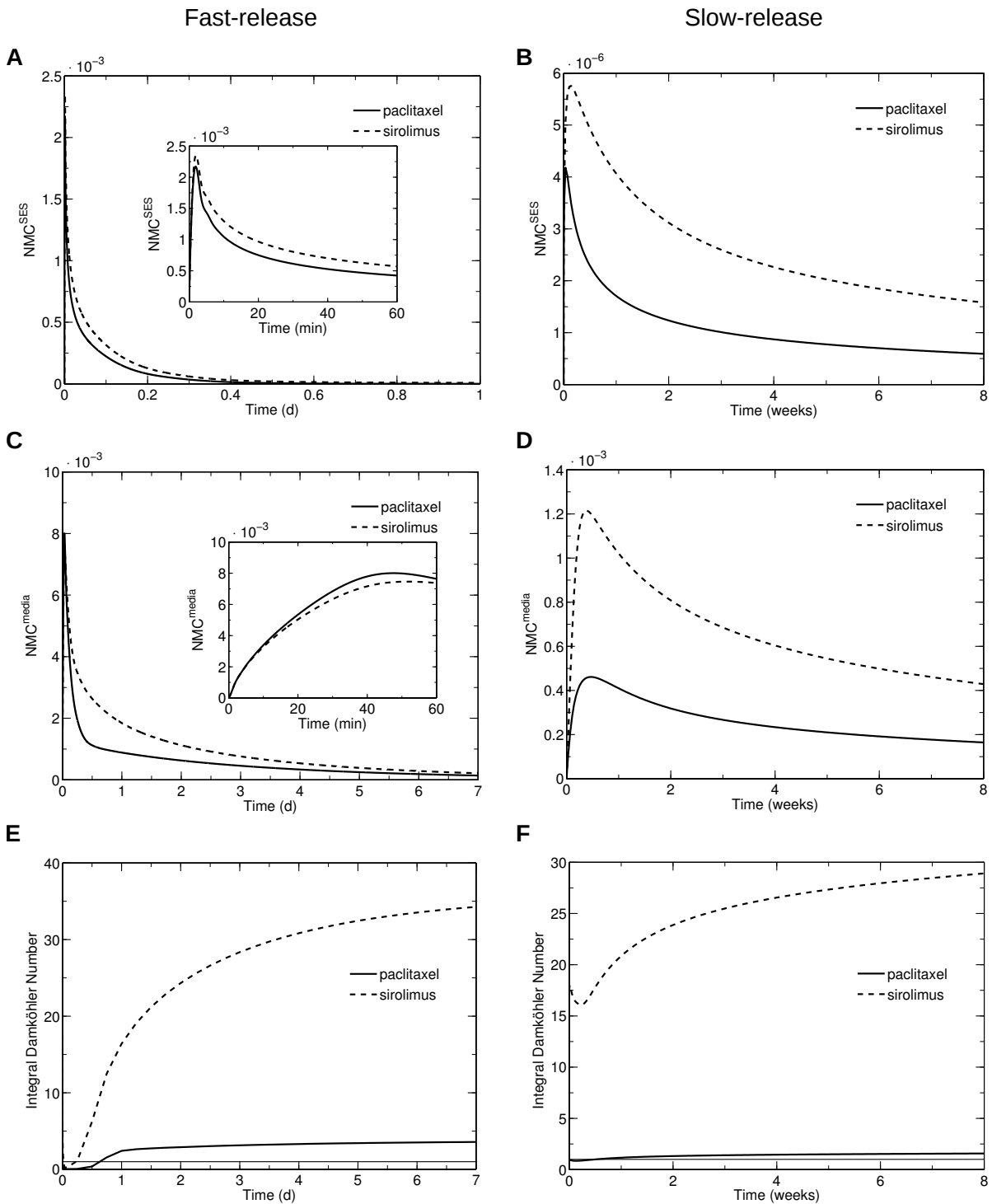


Figure 2.10: Paclitaxel vs. sirolimus. Temporal evolution of the NMC in the SES for a **A**: fast-release and **B**: slow-release stent. NMC in the media for a **C**: fast-release and **D**: slow-release stent. Integral Damköhler number for a **E**: fast-release and **F**: slow-release stent (the horizontal line indicates the $Da_{int} = 1$ threshold).

2.4 Discussion

2.4.1 Drug release is coupled to the drug and its transport properties in the arterial wall

Considering the differences in the binding and unbinding time scales of paclitaxel and sirolimus (see Table 2.5), it might appear surprising that both drugs behave so similarly in the case of a fast-release stent platform. The integral Damköhler number sheds light on this: for paclitaxel, the drug is initially predominantly in the free (and thus mobile) state and invades the media driven by plasma flow in the arterial wall, since the time scale of convection is faster than that for binding. This phase determines the initial distribution of the drug within the arterial wall. With rising concentration levels of free drug in the media, the binding rate increases, leading to an increased Da_{int} and a transitional passage through a phase of competition between the binding and convection terms. Once all binding sites are saturated, any excess drug is washed out. As soon as the stent polymer is empty and the arterial wall has become void of all excess drug, the transport becomes dominated by unbinding since $\tilde{t}_r \gg \tilde{t}_C$ and $\tilde{t}_r \gg \tilde{t}_D$. For sirolimus, on the other hand, the initial dominant process is binding. When the drug enters the media, binding sites are very rapidly occupied, since \tilde{t}_f is several orders of magnitude smaller than \tilde{t}_C or \tilde{t}_D , and only drug exceeding the maximum binding capacity invades new areas of the media. At the same time, this exhaustion of binding sites reduces the binding rate which initiates a shorter, transient passage through a more convection-driven phase. Once the stent polymer coating is empty, the behavior becomes dominated by the unbinding of drug from its binding sites, since the time scale of the unbinding process is longer than that of either convection or diffusion.

As a result, we can subdivide the activity of DES releasing hydrophobic drugs into two phases: an initial release phase where new drug is supplied from the stent and a secondary post-release phase where the drug effect is predominantly determined by the binding and unbinding process. The first phase is prone to changes in the convective and diffusive transport of the free drug. The relevance of this sensitivity is determined by the two Damköhler numbers and not only depends on the release rate (determined by \tilde{D}_c) but also on the initial concentration in the polymer \tilde{c}_0 . As demonstrated by the evolution of the integral Damköhler number for the fast-release stent, even the highly reactive sirolimus transport can become convection-driven, which explains the similarity in concentration distributions of both drugs. The sensitivity analysis of the radial Peclet number in the media Pe_m^r and the medial porosity ε_m illustrate this nicely: in the first case we do not simply vary the relative importance of diffusion and convection but also bring the second Damköhler number down from a regime where binding/unbinding dominates to a diffusion-dominated regime and, thus, we get such a large variability for the low Pe_m^r range. Once $Da_2 > 1$ the results become almost insensitive to further variation. The same is true for the variation of the medial porosity where effectively the first Damköhler number is varied: going from a low to a high porosity we approach $Da_1 \approx 1$, and the peak variability goes down. At the same time the retention coefficient almost does not vary since, with the free drug gone, it is solely determined by the unbinding process.

Once we reduce the drug release rate significantly, we obtain a very different picture: the slow, long-lasting drug supply balances the otherwise rapid unbinding process of sirolimus ensuring a high, only slowly decaying concentration level. The transport of paclitaxel does not benefit as significantly from the more permanent release since the very slow time scale of unbinding determines the retention characteristics independent of the release kinetics.

The present results demonstrate that paclitaxel and sirolimus have widely different transport dynamics in the arterial wall. These differences suggest that different drug delivery strategies should be used for these drugs. Moreover, both drugs have different therapeutic behavior: paclitaxel has a broad therapeutic window with a minimum effective concentration of $\tilde{c}_{\text{eff}} = 1 \cdot 10^{-5} \text{ mol m}^{-3}$ and a maximum concentration level of $\tilde{c}_{\text{tox}} = 1 \cdot 10^{-2} \text{ mol m}^{-3}$ above which the drug becomes toxic [87, 124], while for sirolimus to be effective, saturation of the FKBP12 binding sites appears to be required [187], raising the minimum effective concentration significantly. Thus, the choice of a drug delivery strategy for a particular drug becomes a crucial design parameter in DES development. Based on the present results and for the present geometric and flow conditions considered, a paclitaxel stent platform should optimally employ fast-release kinetics with a low initial drug load, whereas a sirolimus stent should target slow-release kinetics with a higher initial drug load. It was well established in [12] that drug release kinetics are an important factor in the DES design process. Our results complement those findings and highlight the close coupling between the drug chosen and the applied drug delivery strategy.

The interplay between stent, flow, and drug parameters provides an opportunity for implementing sophisticated optimization strategies for targeting “desirable” drug concentration profiles in the arterial wall. Optimal drug profiles would be defined in terms of various criteria including how uniformly the drug is distributed within the arterial wall and whether or not drug concentrations fall within the therapeutically efficacious window.

An additional conclusion from the present results is that the uncertainty in the diffusion coefficients in the arterial wall are of a relatively minor importance for the concentration distribution as long as the relevant dimensionless quantities, most notably the Peclet and Damköhler numbers, remain in the appropriate physiological range.

2.4.2 Multi-layer model offers improved accuracy for pathological situations

Delayed re-endothelialization occurring with DES motivates the need for more detailed drug concentration information, especially close to the endothelial surface. The SES and media are characterized by fundamentally different transport properties (Table 2.3). Accounting for these differences in the TLM revealed that higher concentration levels can be obtained in the SES than in the media especially early after stent implantation (Fig. 2.7 A). The strong sensitivity of the SES drug concentration to the luminal flow field (Fig. 2.5) underscores the differences between the two layers of the arterial wall. This also indicates that assuming a steady arterial flow may not be sufficient to make accurate predictions for the concentration levels in the arterial wall close to the lumen. In the future, time-dependent flow computations should investigate this issue.

A detailed description of drug concentration within the SES is only available in the TLM. The concentration in the SES as an averaged quantity can be extracted from the OLM with the presented approach (eqn. (2.25)). Except for an offset, the qualitative behavior of this global metric is very well recovered and even the distribution pattern at the endothelial surface is in good agreement (Fig. 2.6 B) between the TLM and OLM cases. The reason for this offset is the absence of the drug flux from the stent polymer entering the SES in the model equation. Accordingly, the offset increases with thickening of the SES where the drug flux from the polymer into the SES increases due to the larger contact area between the SES and polymer. This weakness could be overcome by adding an averaged source term to the equation (eqn. (A.5)). However, averaged concentration levels might not be the only information necessary for unraveling the processes leading to delayed re-endothelialization (especially when incomplete

endothelial coverage can be observed even up to five years after DES implantation [151]). As the diseased configuration in Fig. 2.6 A demonstrated, predictions of the flow field diverge significantly depending on the model. Convective forces can contribute considerably to the drug distribution in the arterial wall when free drug levels are elevated (Figs. 2.9 and 2.10 E).

The representation of a diseased arterial wall as presented in this study are drastically simplified for demonstration purposes. In its early stages, atherosclerosis affects primarily the intima and as such the TLM offers the potential to account for different diseased states. For example, the presence of SMCs that have migrated into the SES can be modeled by adding a reaction term to the transport equation in the SES with customized reaction parameters (like the maximum binding site concentration) or changes to the transport parameters in the SES. This could also enable improved evaluation of experimental results that are often performed on healthy vessels [152] and facilitate conjectures to the diseased case.

2.4.3 Reduction of the reaction model fails to capture important features of the transport dynamics

As we could see, the drug transport process is highly dynamic and intertwined with the release process. From a computational point of view, it would certainly be desirable if possible to avoid the stiff (especially in the case of sirolimus) and computationally expensive reaction equation. Tzafriri *et al.* [179] explored several possible concentration-dependent simplifications of the dynamic reaction model. As considered here, the crudest simplification to account for drug binding is to assume a constant partitioning of bound and free drug inherent in the equilibrium model (eqn. (2.9)). Fig. 2.8 illustrates that an equilibrium reaction model fails to capture essential features of the transport process: the binding coefficient κ reduces the transport term permanently and thus the predicted accumulation of drug far exceeds that of the dynamic reaction model. Moreover, the coupling of the convection-diffusion and reaction equations transfers free (i.e. mobile) drug into a bound (i.e. stored) state. This cannot be reflected with the equation obtained by the equilibrium model and thus the residence time of the drug in the arterial wall is underestimated. Matching the prediction of the drug accumulation by the equilibrium model to that of the dynamic reaction model requires a reduction of the partition coefficient, while matching the drug residence time demands an increase. Both objectives cannot be achieved simultaneously.

Optimized Drug Delivery for Drug-Eluting Stents

3.1 Introduction

A primary concern associated with the use of drug-eluting stents (DES) is late stent thrombosis (LST). LST, which involves the formation of blood clots at the site of stent implantation, can occur up to several years after the intervention [20, 26, 151]. Although its development is incompletely understood, LST is thought to occur as a result of the delayed healing of the endothelium following its denudation by both the stent and the balloon upon which the stent is deployed. In support of this notion, a recent study has demonstrated that DES can in some cases remain unendothelialized five years after stent placement [151]. In contrast, bare metal stents (BMS) are typically covered with new endothelium within six months of the stenting procedure [156, 182].

Drugs eluted from DES, typically paclitaxel or sirolimus, act on smooth muscle cells (SMCs) in the arterial wall to arrest their proliferation and hence inhibit vascular restenosis. A likely reason for the delayed endothelial healing in the case of DES is that these same drugs also affect endothelial cell (EC) migration and proliferation [40, 54, 107, 112, 116] and thus greatly limit endothelial wound healing. A key question that arises in the design of DES is whether or not it is possible to deliver anti-proliferative drugs at sufficiently high concentrations to SMCs to prevent restenosis while simultaneously maintaining a sufficiently low drug concentration at the EC surface to allow sufficiently rapid endothelial wound closure.

In the previous chapter, we developed a computational model for the transport of drugs eluted from DES within the arterial wall. The model considered the arterial wall to consist of a two-layered porous structure comprising the subendothelial intima and the media. Drug release from the stent was assumed to occur by diffusion and drug transport in the arterial wall was assumed to occur by convection and diffusion with the drug also undergoing a reversible reaction in the media to represent its binding to SMCs. The baseline model assumed a completely denuded endothelium in the stented portion of the artery, while the endothelium remained intact both upstream and downstream of the stent. The model was applied to the transport of both paclitaxel and sirolimus, and the results revealed important differences between the two drugs in transport characteristics and dynamics. Importantly, the results suggested that

drug distribution within the arterial wall depends on a number of parameters including the drug, its release rate into the arterial wall, and its initial concentration in the stent polymer. These findings serve as the primary motivation for the present chapter which focuses on the optimization of drug delivery strategies from DES for both paclitaxel and sirolimus.

The notion of using optimization in stent design and performance assessment has previously been invoked in other contexts. For instance, previous studies have reported the optimization of stent strut geometry with the goal of minimizing blood flow disturbance in the arterial lumen [9, 70, 71, 171], stresses in the stent itself [196], or stresses in the arterial wall [178]. Pant and collaborators recently reported the first attempt at including multiple cost functions and multiple physical phenomena in the optimization process with the use of a steady (time-independent) transport model to investigate the effect of DES geometric design on the homogeneity of drug distribution and its average concentration in the arterial wall [140, 141]. In all previous studies, stent geometric design served as the design space under consideration. DES drug delivery strategies, which are determined by the release kinetics (elution process) in the polymer coating and the drug concentration initially loaded onto this coating, were not part of these investigations. Release kinetics have been at the heart of experimental [7, 57, 68, 102, 138] and computational [12, 181] investigations over the past few years. However, optimal release kinetics remain an open question in the design process of DES [175, 185]. Optimizing the delivery process of the eluted drug holds the promise of providing strategies that at least in part address the problem of delayed endothelial healing.

In the present chapter, we focus on the development of a strategy to identify optimal drug delivery strategies of DES. To this end, we begin by formulating a cost function that needs to be minimized. The cost function evaluates how well a particular drug delivery strategy maintains an efficacious but sub-toxic drug concentration in the arterial media, provides minimal drug concentration at the endothelial surface in order to allow stent re-endothelialization, and results in a spatially homogeneous drug distribution within the arterial wall. For the purpose of the optimization, the design space is assumed to consist of two parameters: the initial drug concentration on the drug coating and the drug release rate from the coating; thus, these two parameters are assumed to provide an adequate representation of the drug delivery strategy. Minimization of the cost function is accomplished by coupling a novel surrogate management framework optimization algorithm [16, 17] with our physiologically-based computational model of drug transport in stented arteries (see Chapter 2). This approach is applied to determine optimal drug delivery strategies for paclitaxel- and sirolimus-eluting stents.

The results of the optimization suggest that the concentration that needs to be initially loaded onto a DES is dependent on the therapeutic window of the drug. Thus, paclitaxel-eluting stents require very low initial concentrations to comply with the aforementioned objectives. We also observed that optimal drug release times are dependent on the drug kinetics in the arterial wall; this allows either very rapid (quasi-bolus) or long-term zero-order release kinetics for paclitaxel-eluting stents but restricts the release of sirolimus-eluting stents to long-term zero-order kinetics. For both drugs intermediate release kinetics (implying first-order release kinetics) are inappropriate to achieve optimal stent designs.

3.2 Materials and methods

3.2.1 Computational model

Chapter 2 described the computational model for drug transport used in the present optimization analysis. The optimization is performed on a DES consisting of three circular struts spaced at intervals of 0.7 mm and deployed within a straight and rigid-wall arterial segment represented as an axisymmetric cylinder. The stent struts have a diameter of $100\ \mu\text{m}$ to which a $10\ \mu\text{m}$ -thick polymeric coating is applied reflecting approximate dimensions of typical second generation DES [60]. We apply the transport model of Chapter 2 to the elution of the two small hydrophobic drugs paclitaxel and sirolimus. The baseline simulations consider an endothelium that is completely denuded within the stented portion of the vessel but intact otherwise (configuration E1 in Fig. 3.1 A). Some simulations assume a second model configuration where the endothelium is considered denuded not only in the stented zone but also upstream and downstream of the stent for a distance half the length of the inter-strut spacing, always measured from the strut centers (configuration E2 in Fig. 3.1 B). As a consequence of removing the shielding capacity of the endothelium upstream and downstream of the stent, the flow field becomes symmetric around all struts, effectively increasing convection in those two domains of the arterial wall. We define the *therapeutic domain* as the volume of the arterial wall containing the stent and extending by $2/3$ of the stent length both upstream and downstream of the stent.

3.2.2 Cost function

As already mentioned in the Introduction, we propose a cost function that needs to be minimized for optimal drug delivery from DES. Minimization of the cost function serves to accomplish the following three objectives:

1. *Therapeutically efficacious but sub-toxic drug concentration in the media*: The eluted drug needs to have its desired therapeutic effect. We assume that as long as the local drug concentration in the media remains within the drug's therapeutic window, i.e. above an

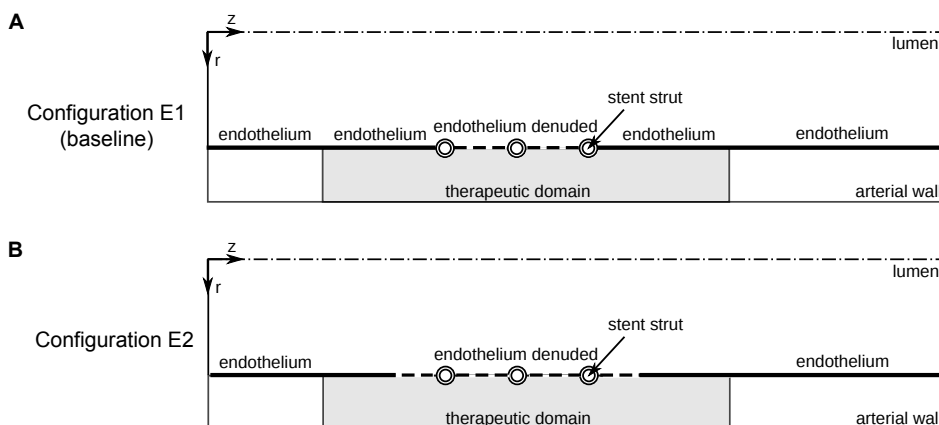


Figure 3.1: Two configurations of the computational model used in the simulations. **A**: Configuration E1 considers an endothelium that is completely denuded within the *stented portion* of the vessel but intact otherwise. **B**: Configuration E2 considers an endothelium that is completely denuded in the *therapeutic domain* but intact otherwise.

efficacious minimum threshold and below a toxic maximum concentration, the drug effectively arrests SMC proliferation thereby having the desired effect of preventing neointimal hyperplasia and vascular restenosis.

2. *Minimal drug concentration at the arterial wall luminal surface:* We need to minimize drug concentration at the luminal surface in order to allow endothelial wound healing to occur. We postulate that if the drug concentration at the luminal surface remains below the lower limit of the drug's therapeutic window, then EC proliferation will be unhindered.
3. *Maximal homogeneity of the drug concentration distribution in the media:* We assume that local concentration extrema are detrimental and that a homogeneous drug distribution in the media is desirable.

How well a particular stent design performs in accomplishing the three above goals can serve as a metric of the quality of the design. For the purpose of the current investigation, a *design* is defined by the two parameters that determine the drug delivery strategy from DES: the initial drug concentration c_0 in the stent polymer coating within which the drug is loaded and the characteristic drug release time from this polymer coating. Because drug release is assumed to occur by diffusion only, this characteristic time is given by $t_E = \pi L_c^2 / (4D_c)$, where L_c is the thickness of the polymer coating and D_c is the drug diffusion coefficient in the coating. The two parameters defining a particular design serve as input for a simulation using our computational model. The resulting concentration distribution is then used as the basis to quantify the performance of a particular design by means of the following cost function:

$$J_{\text{ETH}}(c_0, t_E) = \bar{I}_m + \frac{1}{3} (\bar{T}_l + \bar{T}_{\text{ses}} + \bar{T}_m) + \bar{H}_m. \quad (3.1)$$

The cost function is formulated as the sum of three scores evaluated within the therapeutic domain of the numerical model: a score that denotes drug inefficacy in the media (\bar{I}_m), an overall toxicity score that consists of the arithmetic average of the three toxicity scores in the lumen, subendothelial space (SES), and media (\bar{T}_l , \bar{T}_{ses} and \bar{T}_m , respectively), and a drug homogeneity score (\bar{H}_m). The shapes of the cost function J_{ETH} as well as the inefficacy, toxicity, and homogeneity scores are schematically depicted in Fig. 3.2. We will now describe the three scores that constitute the cost function in detail.

Inefficacy score

The inefficacy score in the media I_m is defined as follows:

$$I_m = \frac{1}{V_{m,\text{th}}} \int_{V_{m,\text{th}}} \varphi \, dV \quad \text{where} \quad \varphi = \begin{cases} 1, & \text{if } c_{T,m} \leq c_{\text{eff}}, \\ 0, & \text{otherwise.} \end{cases} \quad (3.2)$$

Every point in the medial portion of the therapeutic domain with a drug concentration below the minimum efficacious threshold c_{eff} is assigned a score of 1 and a score of 0 otherwise (Fig 3.2 A). The inefficacy score I_m is obtained by integrating the point-by-point scores over the entire medial therapeutic domain volume ($V_{m,\text{th}}$) and then dividing by this volume. Therefore, I_m represents the percentage of the media within the therapeutic domain where the total drug concentration $c_{T,m}$ (i.e. sum of free and bound drug) falls below the minimum efficacy threshold.

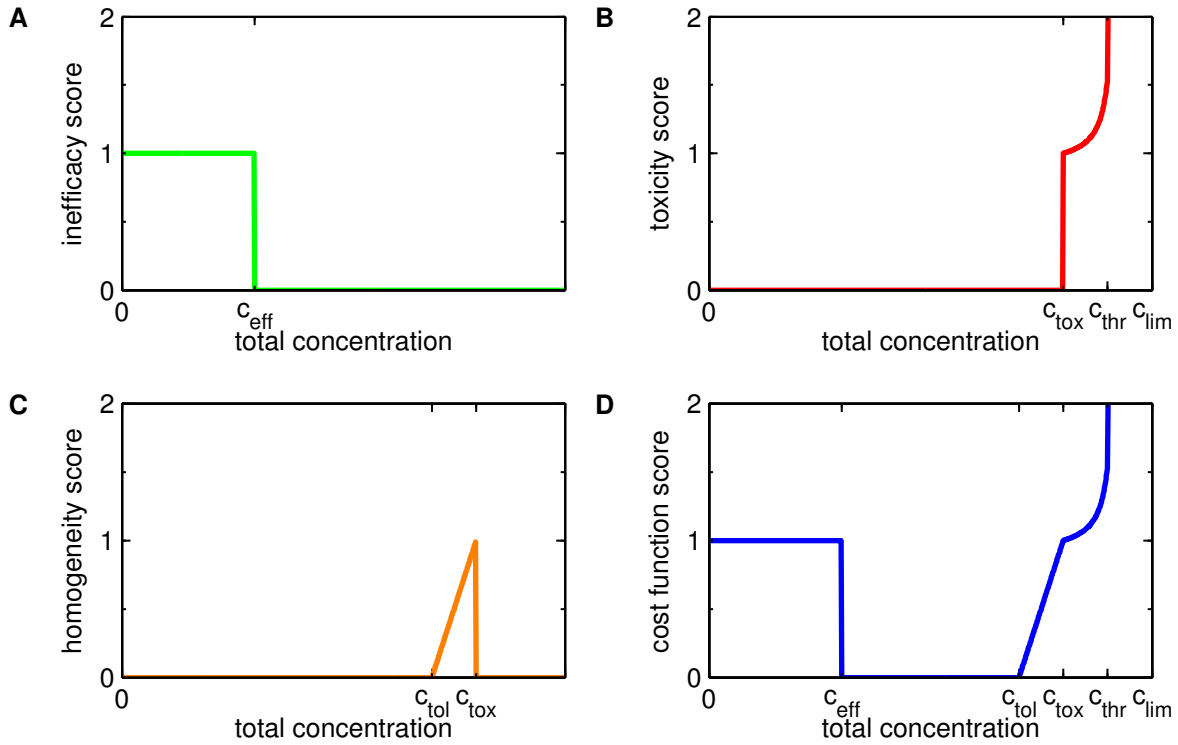


Figure 3.2: Shape of the cost function and its contributing scores. **A:** inefficacy score I_m ; **B:** toxicity score T_m ; **C:** homogeneity score H_m ; **D:** cost function J_{ETH} representing the sum of the individual scores.

Equation (3.2) is evaluated for every time point of the simulation and then averaged over the entire simulation time t_{end} yielding the time-averaged inefficacy score \bar{I}_m . The simulation time t_{end} corresponds to the period of time over which the optimization is performed.

Toxicity score

While the minimum efficacious concentration c_{eff} sets the lower limit of the drug therapeutic window, the toxic concentration c_{tox} defines the upper limit. In the media, the toxicity score \bar{T}_m is obtained through the following series of steps. First, similar to the inefficacy parameter, the expression

$$\vartheta_m = \frac{1}{V_{m,th}} \int_{V_{m,th}} \vartheta \, dV \quad \text{where} \quad \vartheta = \begin{cases} \frac{c_{T,m} - c_{tox}}{\gamma_{thr} c_{tox}}, & \text{if } c_{T,m} \geq c_{tox}, \\ 0, & \text{otherwise.} \end{cases} \quad (3.3)$$

is evaluated. This integral quantifies the fractional volume of the media in the therapeutic domain that is exposed to toxic drug concentrations, with the score weighted by the relative deviation from the toxic threshold so that the higher the concentration above the toxic threshold, the higher the score (and hence the larger the penalty). The scaling factor γ_{thr} provides a mechanism for adjusting the weighting to establish which deviation from the toxic threshold is considered equally harmful as a concentration that is not efficacious (i.e. a score of 1). Once this first step is completed, the second step consists of mapping the result of Equation (3.3)

onto a hyperbola whose asymptote is at the limit value ϑ_{lim} :

$$T_m = \begin{cases} 1 + \frac{\vartheta_{\text{lim}} - \vartheta_{\text{thr}}}{\vartheta_{\text{lim}} - \vartheta_m} \frac{\vartheta_m}{\vartheta_{\text{thr}}}, & \text{if } 0 \leq \vartheta_m < \vartheta_{\text{lim}}, \\ \infty, & \text{otherwise.} \end{cases} \quad (3.4)$$

The slope of this hyperbola is adjusted such that it passes through 1 at the threshold value ϑ_{thr} . Furthermore, the hyperbola is lifted by 1 to emphasize that any toxic concentration is undesirable. The rapid increase in toxicity score as drug concentrations increase above the toxic threshold emphasize that these concentrations should be avoided by all means and serve to drive the optimization away from these concentrations. Fig. 3.2 B schematically depicts the variation of the toxicity score with drug concentration.

The arterial wall luminal surface is handled virtually identically to the media with the following two equations:

$$\vartheta_{S,l} = \frac{1}{S_{l,\text{th}}} \int_{S_{l,\text{th}}} \vartheta_S \, dS \quad \text{where} \quad \vartheta_S = \begin{cases} \frac{c_1 - c_{\text{eff}}}{\gamma_{\text{thr}} c_{\text{eff}}}, & \text{if } c_1 \geq c_{\text{eff}}, \\ 0, & \text{otherwise.} \end{cases} \quad (3.5)$$

$$T_l = \begin{cases} 1 + \frac{\vartheta_{\text{lim}} - \vartheta_{\text{thr}}}{\vartheta_{\text{lim}} - \vartheta_{S,l}} \frac{\vartheta_{S,l}}{\vartheta_{\text{thr}}}, & \text{if } 0 \leq \vartheta_{S,l} < \vartheta_{\text{lim}}, \\ \infty, & \text{otherwise.} \end{cases} \quad (3.6)$$

There are two differences to point out: 1) Given that we are now considering the lumen-wall interface, the integral in Equation (3.5) becomes a surface integral rather than a volume integral. 2) At the luminal surface we do not want the drug to impair EC proliferation; therefore, we consider that the “toxic” concentration limit is the minimum efficacious concentration and formulate the toxicity score in a manner to drive the algorithm towards concentrations lower than this threshold. We note that because a concentration jump occurs across the luminal surface whenever endothelium is present, we evaluate the interfacial toxicity parameter from both the luminal side (denoted by $\vartheta_{S,l}$ and T_l) and the SES side (denoted $\vartheta_{S,\text{ses}}$ and T_{ses}). The SES evaluations are similar to those shown above for the lumen but with the concentration c_1 replaced by c_{ses} . The arithmetic mean of the toxicity scores from the luminal and SES sides provides the toxicity score of the luminal surface T_e . As in the case of the inefficacy score, the toxicity scores are evaluated for every time point of the simulation and then averaged over the entire simulation time t_{end} yielding the desired time-averaged toxicity scores.

Homogeneity score

The final term appearing in the cost function is the homogeneity score H_m which is defined as follows:

$$H_m = \frac{1}{V_{m,t}} \int_{V_{m,t}} \eta \, dV \quad \text{where} \quad \eta = \begin{cases} \frac{c_{T,m} - c_{\text{tol}}}{c_{\text{tox}} - c_{\text{tol}}}, & \text{if } c_{\text{tol}} \leq c_{T,m} < c_{\text{tox}}, \\ 0, & \text{otherwise.} \end{cases} \quad (3.7)$$

The portion of the therapeutic domain of the media with a concentration superior to a tolerable value c_{tol} but inferior to the toxic threshold c_{tox} is weighted on a scale that increases linearly from 0 to 1 as the drug concentration approaches c_{tox} (see score function in Fig. 3.2 C). The spatially-averaged H_m is then averaged over the simulation period t_{end} to form the final homogeneity score \overline{H}_m .

The primary purpose of \overline{H}_m is to drive the optimization to designs with a more spatially homogeneous drug distribution in the arterial wall. Designs which lead to concentrations that lie within the reduced concentration window bound by c_{eff} and the tolerable concentration threshold c_{tol} have a smaller concentration variation and are thus more homogeneous. They are favored over less optimal designs with concentrations that lie in between c_{tol} and c_{tox} . In addition to this role, the tolerable concentration c_{tol} as formulated here also serves the purpose of creating a buffer region in the optimization by penalizing concentrations close to the toxic limit. This ensures a certain robustness of the optimization, in the sense that optima that are immediately adjacent to non-optimal regions would be avoided.

Choice of cost function parameters

The cost function described above provides a set of calibration parameters that offer flexibility in balancing the relative importance of the efficacy against toxicity. While the two concentration thresholds c_{eff} and c_{tox} need to be determined experimentally, the remaining four parameters c_{tol} , γ_{thr} , ϑ_{thr} and ϑ_{lim} allow calibration of the stringency of the toxicity constraint. Thus, it might be deemed acceptable to live with a certain level of wall toxicity in some cases but not in others, and these adjustable parameters allow this form of fine tuning. In light of the severe consequences of delayed endothelial healing [53, 69] and in view of currently available experimental data, we chose the calibration parameters summarized in Table 3.1.

The choice of parameter values for c_{tol} , γ_{thr} , ϑ_{thr} and ϑ_{lim} is rather conservative and is expected to allow us to avoid arterial wall toxicity. Lacking experimental data on the relative severity of toxic concentration in the different layers of the arterial wall covered by each toxicity score we (arbitrarily) assume the three toxicity scores to be of equal importance. As a consequence we choose the same set of calibration parameters for each of the toxicity scores and a weight factor of $1/3$ multiplying each toxicity score of the cost function. It should be recognized, however, that new experimental results or clinical studies might lead to future changes in some or all of these parameters as well as choosing a different set of parameters for each individual score.

Both paclitaxel and sirolimus inhibit the proliferation of SMCs and ECs by arresting the cells at a point in their cell cycle. At sufficiently high concentrations, paclitaxel is cytotoxic and leads to cell death [112]. Values for toxic paclitaxel concentrations are available in the

Table 3.1: Calibration parameters of the cost function

| Drug | c_{tol} | γ_{thr} | ϑ_{thr} | ϑ_{lim} | c_{eff} (mol m ⁻³) | c_{tox} (mol m ⁻³) |
|------------|------------------------|-----------------------|--------------------------|--------------------------|---|---|
| Paclitaxel | 90% · c_{tox} | 1% | 1% | 5% | $1 \cdot 10^{-5}$ | $1 \cdot 10^{-2}$ |
| Sirolimus | 90% · c_{tox} | 1% | 1% | 5% | 0.29 | 0.73 |

literature [87, 102]. The values of minimum efficacious concentration and toxic concentration for paclitaxel used in the present work, $c_{\text{eff}} = 1 \cdot 10^{-5} \text{ mol m}^{-3}$ and $c_{\text{tox}} = 1 \cdot 10^{-2} \text{ mol m}^{-3}$, are taken from [124].

Unlike paclitaxel, sirolimus is a cytostatic agent, i.e. its arrest of the cell cycle is not associated with cell death even at relatively elevated concentrations. This behavior allows for a wider therapeutic window for sirolimus than for paclitaxel. While the minimum sirolimus efficacious concentration may be as low as $1 \cdot 10^{-6} \text{ mol m}^{-3}$ [94, 123, 147, 191], the toxic threshold is less clear, even if limited toxic reactions to sirolimus have been reported [83, 191]. In the present work, we investigated two different therapeutic windows. The first is based on the results of Wang *et al.* [187] that suggest that for effective inhibition of restenosis, it is desirable to maintain the cellular binding sites for sirolimus occupied; thus, we use a very narrow therapeutic window spanning only 80% to 200% of the maximum binding site density. The second therapeutic window we study aims to isolate the effect of the drug itself on our results and thus uses the same three order of magnitude-wide therapeutic window used for paclitaxel.

The effect of total drug dose (integral of drug concentration over time) is not considered as a separate metric in the present cost function because the experimental evidence in the literature of the effect of drug dose is too sparse to be translated into a reliable metric. Also, we did not include any measure of the homogeneity of the drug concentration distribution per se, as the homogeneity score considered here is completely dependent on the choice of the therapeutic window and c_{tol} , both of which are specified model parameters.

Practical considerations

To avoid spending valuable calculation time on undesirable parameter configurations, we implemented additional criteria terminating the evaluation process of the cost function if the toxicity parameter ϑ_m surpasses a value of 5% or if beyond five days of simulated time the maximum total concentration in the media $c_{T,m}$ drops below the efficacious limit. The latter criterion automatically discards designs that do not lead to efficacious concentration levels within that five day period. If the simulation is terminated early, we take the score calculated at the last computation prior to termination as the basis for the remaining time in the averaging process. The toxicity parameter was capped at a maximum value $T_{\text{max}} = 10$, since this already corresponds to a ten-fold increase over what by design is considered an undesirable situation.

To impose a gradient in the case of non-efficacious designs, we add $1 - \max(c_{T,m})/c_{\text{eff}}$ to \bar{I}_m . Based on typical DES release times and motivated by the pathobiology following stent implantation, we set four weeks as the target simulation time t_{end} [3, 94, 121, 150]. A sensitivity study of the cost function has shown that our results are fairly insensitive to a variation of the evaluation period between one and eight weeks.

To keep the simulation time of each function evaluation to a minimum and as has already been mentioned, we only include three stent struts in our numerical model with the endothelium completely denuded in the stent region and intact upstream and downstream of the stent. Thus, the overall stent length simulated is considerably smaller than real stents. Our simulations have shown that the concentration distribution around the struts within the arterial wall, with the exception of the first and last strut, is symmetric (Chapter 2). Since this concentration distribution serves as the basis for the evaluation of our cost function, we can approximate a longer stent by appropriately multiplying the score obtained for the symmetric mid-section

of our strut setup. A sensitivity analysis has revealed that the final results are only minimally altered by this manner of stent prolongation.

3.2.3 Optimization framework

We use a Surrogate Management Framework- (SMF-) type optimization algorithm [23] to minimize the cost function J_{ETH} . Here we will only outline the basic concepts of this method. The reader is referred to Chapter 4 for more details.

The SMF method belongs to the class of pattern search algorithms for numerical optimization. These algorithms minimize a given cost function by gradually exploring the design space. Booker *et al.* [23] introduced the idea of a *global search step* that efficiently leverages information obtained from previously evaluated points of the design space. All previously evaluated points are used to create an approximation of the cost function hypersurface which serves as an inexpensive surrogate to identify potential new minimum points in the entire design space. As long as the potential minimum points revealed by the search step yield improved cost function values, the information from these points is added to the approximation surface and a new search is performed.

The most common interpolation method used in this context is the Kriging method [97, 122]. A major advantage of this interpolation method is that on top of an estimation of the function value, it also provides an uncertainty about the estimated value. This information can then be used to enhance the search procedure: instead of minimizing the Kriging interpolant directly, new prospective optimum points are identified by maximizing the probability of improvement over the current optimum by a predefined margin [86].

The optimization procedure begins with the evaluation of a set of initial sampling points to create the very first surrogate surface. We use the latin hypercube sampling algorithm presented in [56] to assure a uniform distribution of these points throughout the design space. We use 20 initial designs for our 2-dimensional design space.

When a search step fails to provide a new minimum a *poll step* is initiated. Starting from the current minimum point of the design space, a set of new points is chosen in the design space. The choice of these points is restricted to a grid which discretizes the design space and follows a distinct set of rules which defines the search pattern. The cost function values at these points are then evaluated (a process referred to as *polling*). If any one of these points yields a cost function value that is lower than the value associated with the initial point, then this point becomes the new minimum point from which the next poll step originates. If, however, none of these points is able to improve the cost function, then the grid spacing is refined and a new set of points is chosen on this new grid. As long as certain conditions are met in this process, convergence to a minimum is guaranteed. A new search step succeeds the poll step, independent of its outcome.

We consider the design space to have been exhaustively explored once the mesh of the poll step is refined 10-fold and the search step fails to identify new optimum points in five consecutive search steps. At this point the optimization is terminated.

We employ a novel SMF algorithm which was developed by our collaborators Belitz and Bewley and is described in detail in [16, 17]. The major novelty of this algorithm lies in the choice of the underlying lattice used for the optimization: instead of the classical Cartesian lattice, the search and poll steps are performed on a “laminated” lattice [16], which maximizes the regularity and density of the grid points for the respective dimension of the design space.

Also, the poll step of our method uses a new mesh adaptive direct search (MADS) algorithm, dubbed “ λ -MADS” [16].

3.2.4 Optimization cases

In this chapter, we performed six different optimization runs in total: two runs with the baseline model as described in section (configuration E1 in Fig. 3.1 A) with paclitaxel and sirolimus as the eluted drugs and two runs with a modified model where the endothelium was considered denuded upstream and downstream of the stent (configuration E2 in Fig. 3.1 B) (again both drugs). The fifth run investigated the effect of having paclitaxel loaded only onto the part of the stent coating that was embedded in the arterial wall. The final run was performed on the baseline model with sirolimus as the eluted drug but assuming the therapeutic window of paclitaxel.

3.3 Results

We wish to determine the optimal drug delivery strategy, defined here as the combination of the drug concentration initially loaded onto the stent c_0 and the drug release time t_E as characterized by the diffusion coefficient of the drug D_c within the $10\ \mu\text{m}$ -thick polymeric matrix in which it is embedded. The optimization is performed for both paclitaxel and sirolimus.

3.3.1 Paclitaxel delivery optimization

Figure 3.3 A depicts the surface of the cost function obtained using the default model setup of paclitaxel elution. The axes span equivalent release periods of a few minutes to several years and concentration values from 0.1 to $100\ \mu\text{g cm}^{-2}$. The plot is the result of a natural neighbor interpolation [166] of the evaluated designs indicated by the gray dots. Point 1 indicates the design with the lowest value of the cost function and is thus considered the global minimum. Borrowing terminology from topographical maps (equating function value magnitude with elevation), we can describe the resulting shape of the cost function as a mountain range with two valleys marking two optimal regions. Further exploiting this analogy, we will refer to the direction pointing towards increasing concentration as north, while we denote the direction of increasing release times as east. As indicated by the black coloring, no feasible designs can be found for initial loading concentrations that exceed $10\ \mu\text{g cm}^{-2}$ (demarcated by a horizontal white dashed line). Below $10\ \mu\text{g cm}^{-2}$ the optimization reveals two valleys separated by a ridge. The separation occurs at the one week mark. We distinguish the following three regions demarcated approximately by the white dashed lines in the figure: a rapid release (release time of only hours) region labeled *QB* representing quasi-bolus administration of the drug; an intermediate release (weeks) region labeled *FO* where release is concentration-dependent and follows first-order kinetics; and a slow release (months) region labeled *ZO* where drug release becomes concentration-independent and thus follows zero-order kinetics. The first row in Fig. 3.4 illustrates typical release profiles for these three cases. Points 1 - 3 are typical example designs for each of these regions. Their scores are decomposed in Table 3.2.

Three colored contours are shown in Figure 3.3: the green contour line traces $\bar{I}_m = 1$ and thus defines a border for inefficacious designs; the yellow contour line traces $\bar{T}_m = 1$ and thus marks the threshold of toxicity in the media; the red contour line traces $\bar{T}_e = 1$ and hence demarcates the zone of unacceptable endothelial toxicity. At the northern border of the *QB*

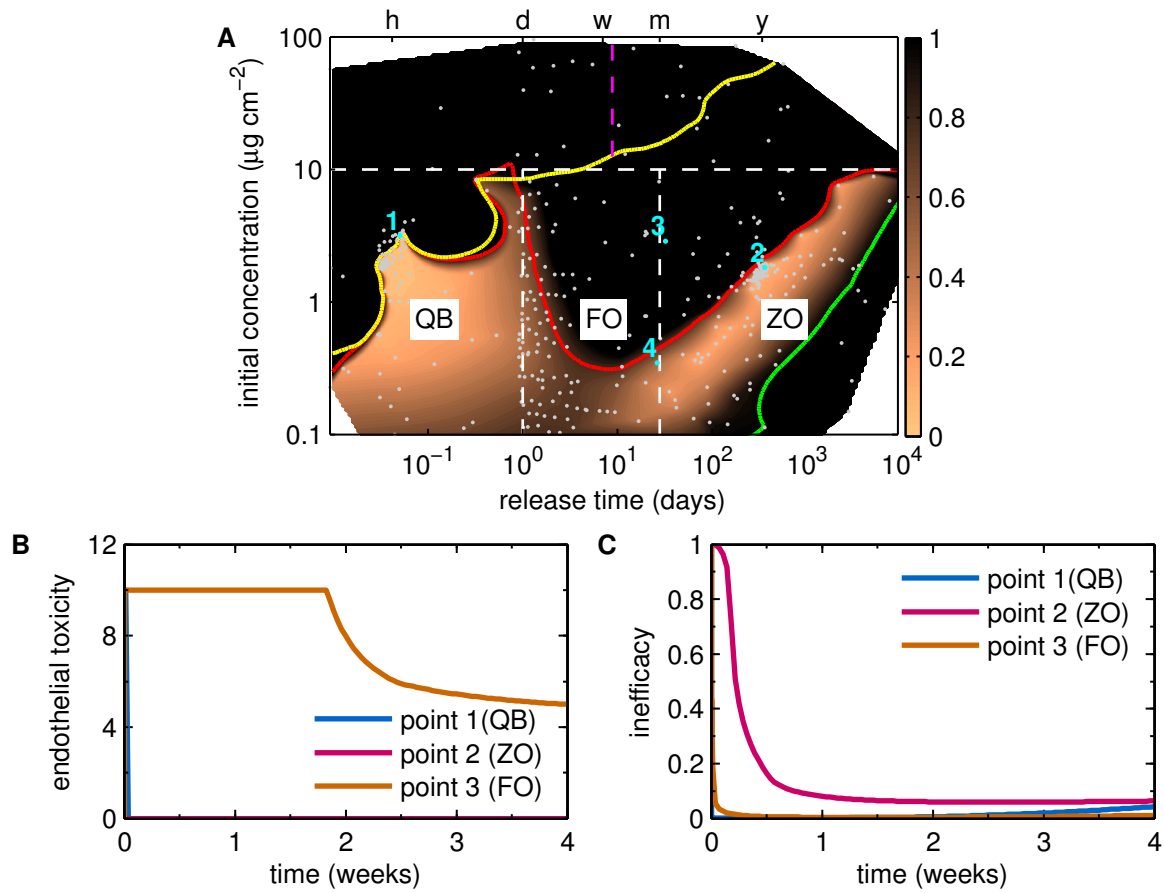


Figure 3.3: Paclitaxel baseline optimization. **A:** Filled contour plot of the cost function over the design space of *initial concentration in the stent polymer* c_0 and *release time* t_E . The scale for the cost function representation is truncated at a maximum of 1; all values larger than 1 are colored black. The white dashed vertical lines separate the three regions of *quasi-bolus*, *first-order* and *zero-order* release kinetics. The dashed magenta line marks the time scale for drug unbinding. The green contour line traces $\bar{I}_m = 1$, the yellow contour line $\bar{T}_m = 1$, and the red contour line $\bar{T}_e = 1$. The horizontal axis on top of the plot marks the time points of 1 (h)our, 1 (d)ay, 1 (w)EEK, 1 (m)onth and 1 (y)ear. Detailed scores of the representative design points 1 - 4 are summarized in Table 3.2. **B:** Time evolution of the endothelial toxicity score \bar{T}_e for points 1, 2, and 3 taken respectively from the *QB*, *FO*, and *ZO* regions. **C:** Time evolution of the inefficacy score \bar{I}_m for points 1, 2 and 3.

Table 3.2: Detailed cost function score data of the points 1 - 4 in Fig. 3.3 and 5 - 7 in Fig. 3.5

| # | c_0 (mol m ⁻³) | D_c (m ² s ⁻¹) | J | \bar{I}_m | \bar{T}_1 | \bar{T}_{ses} | \bar{T}_m |
|---|------------------------------|---|-------|-------------|-------------|-----------------|-------------|
| 1 | 3.4 | $1.8 \cdot 10^{-14}$ | 0.059 | 0.012 | 0.060 | 0.060 | 0.020 |
| 2 | 2.0 | $2.6 \cdot 10^{-18}$ | 0.13 | 0.13 | 0 | 0 | 0 |
| 3 | 3.1 | $2.8 \cdot 10^{-17}$ | 5.2 | 0.0091 | 5.6 | 10.0 | 0 |
| 4 | 0.37 | $3.5 \cdot 10^{-17}$ | 0.48 | 0.10 | 0.32 | 1.1 | 0.037 |
| 5 | 9.7 | $2.4 \cdot 10^{-18}$ | 0.080 | 0.080 | 0 | 0 | 0 |
| 6 | 2.3 | $2.6 \cdot 10^{-14}$ | 0.11 | 0.071 | 0.060 | 0.060 | 0.024 |
| 7 | 3.4 | $1.9 \cdot 10^{-14}$ | 0.062 | 0.016 | 0.060 | 0.060 | 0.020 |

valley, the medial and endothelial toxicity almost coincide. It is important to highlight that care should be taken when interpreting the results. The interpolated surface is only as good as the underlying evaluated designs (indicated by gray dots). While the western bound of the *QB* valley is a good representation of the actual shape, the shape of the northern bound is less certain since no designs have been evaluated east of the optimum point 1. While this limits our ability to come to detailed conclusions in some local regions of the design space, the overall conclusions are unaffected.

Figure 3.3 broadly reveals two optimal regions. The first lies in a polygonal, relatively flat valley spanning an initial concentration range of 0.3 to 3 $\mu\text{g cm}^{-2}$ and covering a release time of 1 to 6 hours. The second optimal region is in a chasm beginning at a release time scale of ≈ 5 months and an initial concentration of $\approx 0.2 \mu\text{g cm}^{-2}$ and ending at a release time of ≈ 6 years and an initial concentration of $\approx 8 \mu\text{g cm}^{-2}$. It is interesting to note that designs corresponding to today's stents are found in the release range of a few weeks to a few months with initial concentration loads beyond 10 $\mu\text{g cm}^{-2}$ [152] and thus lie on top of the central mountain in the north of our landscape.

Figure 3.3 B compares the time evolution of endothelial toxicity (T_e) for the three different release strategies defined by points 1, 2, and 3 in panel A over the 4-week simulation period. As already mentioned, point 1 (in the *QB* region) corresponds to the overall optimum of the cost function. Point 2 (*ZO* region) is the local optimum within the chasm described above. Point 3 (*FO* region) has a release time scale of about one month with a similar initial concentration as point 1. The endothelial toxicity score of point 1 exhibits a very short but high peak within the first day after stent implantation. Except for a very small bump on day two (not visible on the current scale), the endothelial toxicity associated with point 2 has a constant value of zero. Point 3 shows a maximal toxicity score for more than a week before beginning to decrease gradually. The transition to a level of $T_e = 5$ in the following weeks reflects the fact that drug release decreases so that the concentration from the luminal side drops below the toxic threshold. The concentration on the SES side, on the other hand, remains above this threshold for the entire 4-week period.

Figure 3.3 C depicts the time evolution of the inefficacy score in the media \bar{I}_m over the 4-week simulation period for the same three points as in panel B. The behavior is very similar for points 1 and 3 with \bar{I}_m attaining minimum inefficacy (i.e. maximum efficacy) within a day of stent deployment and remaining at this level for almost the rest of the time. The inefficacy

associated with point 1 begins to increase marginally after about 3 weeks leading to a slightly worse average inefficacy \bar{I}_m score than point 3 (see Table 3.2). The inefficacy score of point 2 is considerably larger than that of the other two points but becomes quite small at the 1-week time point and beyond.

Point 4 in Figure 3.3 A is a point of additional interest in that it is characterized by a similar release time as point 3 but with an initial drug concentration that is ten-fold smaller. As shown in Table 3.2, this point still allows significant exposure of the endothelial surface to unacceptably high concentrations despite the low level of initial stent loading. This observation underscores the generally poor drug delivery strategies associated with the intermediate release (*FO*) region.

The results thus far have focused on quantitative assessments averaged over the entire stent. In order to gain additional physical insight into the optimization results, we now turn our attention to a more local level and consider the drug concentration distributions around the stent struts. Fig. 3.4 depicts the normalized concentration distributions around the stent strut furthest downstream (third strut) at the 1-hour, 2-week, and 4-week time points and for the three representative design points 1, 2, and 3 representative respectively of quasi-bolus release, zero-order release, and first-order release as was defined above.

The quasi-bolus drug release kinetics (left column in Fig. 3.4 B) lead to the release of all of the drug within the first few hours after implantation. Accordingly, the highest drug concentrations are attained at the 1-hour time point with very high local concentrations (exceeding 100 times the toxic threshold) in the media near the stent strut and unacceptably high concentrations in the subendothelial space (SES). At this time point, drug concentrations are at efficacious levels over practically the entire media. The next two time points illustrate how the magnitude of drug concentration decays over the following four weeks. At the four-week time point, concentrations in the media in between the stent struts and closest to the stent surface have lost their efficacy. Because the characteristic time for drug release in this case is considerably shorter than all of the time scales characterizing drug transport and reaction (convection, diffusion, as well as drug binding and unbinding), the quasi-bolus release strategy can be thought of as a transport-limited scenario.

For the first-order drug release kinetics (middle column), large parts of the media are exposed to efficacious concentration levels at the 1-hour time point. This is also true for the SES. In the downstream zone close to the strut, the concentration levels reach ten-fold those of the efficacious threshold. Two weeks later, the concentration levels are elevated in the media and are efficacious over the entire width. Although the overall concentration in the SES has dropped, the concentration close to the strut is considerably higher than the concentration that would inhibit EC proliferation and this remains the case even at four weeks. In the media, the concentration has decreased and in the areas in between the stent struts has attained sub-efficacious levels.

For the zero-order drug release kinetics (right column), the concentrations do not attain the efficacious threshold within the first hour anywhere in the domain. After two weeks, the concentration levels in most of the media are efficacious, except for the zones in between struts close to the luminal surface. The steady release over the next two weeks leads to a very similar concentration distribution at the end of the simulation. Since all time scales of the transport and reaction problem in the arterial wall are significantly faster than the release time scale in this case, we have reached a quasi-steady state of the transport in the arterial wall and hence a release-limited scenario.

The above simulations were performed for the baseline case where the endothelium was

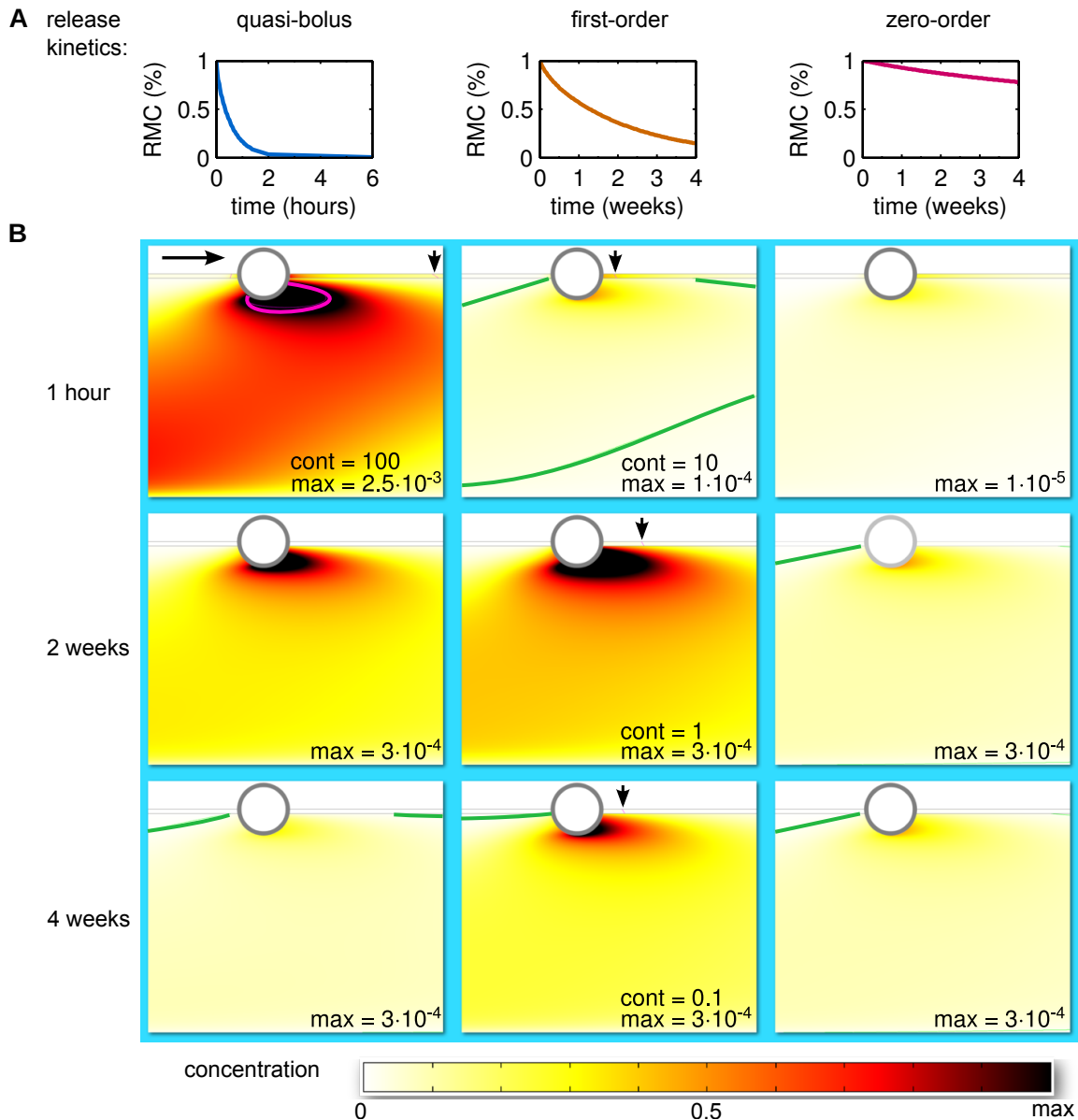


Figure 3.4: Release kinetics and resulting normalized concentration distributions for representative designs of the *quasi-bolus* (point 1), *first-order* (point 3), and *zero-order* (point 2) regions. **A**: Release profiles as quantified by the time evolution of the remaining mass percentage (RMC) of drug in the polymer coating. **B**: Contour plots of the normalized concentration distribution at 1 hour (*first row*), 2 weeks (*second row*) and 4 weeks (*third row*) post stent implantation. The different release kinetics require adjustment of the color scale in some of the panels. The maximum value of the color scale for the normalized concentration is indicated by the word “max”. The highest concentration values encountered close to the stent strut surface are colored in black. With endothelium only present at the downstream side of the strut, an asymmetric flow is induced around the strut causing an asymmetry in the concentration distribution. A green contour line marks the threshold between efficacious and non-efficacious drug concentration in the media: the depicted media at 2 weeks of quasi-bolus and first-order release kinetics are entirely exposed to efficacious concentration, while drug concentration in the depicted media at 1 hour of zero-order release kinetics has not yet reached efficacious levels. Magenta countour lines in the media and vertical arrows at the endothelium indicate $\text{cont} = c/c_{\text{tox}} - 1$. The black horizontal arrow in the very first tile points in the direction of flow in the lumen.

assumed to be completely denuded in the stented portion of the vessel but intact otherwise. In order to investigate the sensitivity of our optimization results to this assumption, we performed simulations where the endothelium was also denuded both upstream and downstream of the stent. As depicted in Fig. 3.5 A, the resulting contour plot of the optimization in this case is very similar to that of the baseline case (Figure 3.3 A) with two optimal valleys separated by a non-optimal mountain. The contour line tracing a value of the cost function of 1 is shown for the baseline case for comparison. For the present simulation the contour of $J_{\text{ETH}} = 1$ approximately follows the border of the black regions. The quasi-bolus valley is almost unaltered with only its western border shifted slightly to faster release times. The chasm of the zero-order release is wider and more elongated compared to the baseline surface. Hypothetically, even initial concentration values of up to $100 \mu\text{g cm}^{-2}$ can now lead to feasible designs; however, that would require a release time of ≈ 30 years! Qualitatively, the upper bound formed by endothelial toxicity has shifted to higher concentration values in the range of first and zero-order release. This becomes evident quantitatively when we compare the score of the global optimum point (point 5 in Table 3.2) of this optimization to the zero-order release optimum of the baseline optimization (point 2). For a similar release time of approximately 13 months, the initial concentration can be raised 5-fold, increasing the efficacy of the design by almost 40% and entirely avoiding toxic concentration levels at the endothelial surface.

The contour plot in Fig. 3.5 B shows how the optimization results are affected when drug is initially loaded only in the part of the stent polymer coating that is embedded into the arterial wall. Again, the white contour line traces $J_{\text{ETH}} = 1$ for the baseline optimization (Fig. 3.3) whereas for the present simulation the contour of $J_{\text{ETH}} = 1$ approximately follows the border of the black regions. It is important to note that the representation of the region with a release time t_E of months and years (ZO region) of the present simulation is less accurate since only few designs have been evaluated in that region (indicated by gray dots) during the optimization. The most obvious difference compared to panel A and to the baseline simulation is that the bound to the west of the quasi-bolus region is no longer present. The release time can thus be decreased without causing adverse concentration at the endothelium. The global optimum (point 7) can be found in this valley. The differences between this optimum and the optimum of the baseline optimization (point 1) are insignificant.

Figures 3.5 C and D compare the temporal evolution of the endothelial toxicity score and the medial inefficacy score for points 5, 6 and 7. The detailed breakdown of the averaged scores can be found in Table 3.2. The global optimum of the simulation with completely denuded endothelium (point 5) shows zero toxicity at the luminal surface at all times. The endothelial toxicity of the quasi-bolus optima in both cases in Figure 3.5 (points 6 and 7) evolves identically, shooting up to maximum toxicity within seconds after implantation and then decreasing to zero after 6 hours. Fig. 3.5 C illustrates that the inefficacy of the zero-order optimum of the denuded endothelium optimization case (point 5) decreases rapidly in the first week and then more slowly thereafter until the end of the simulation. Both quasi-bolus optima decrease nearly immediately to near zero inefficacy. At longer times, the inefficacy score of point 6 rises slowly, whereas that of point 7 remains small for the entire simulation period.

3.3.2 Sirolimus delivery optimization

The above presentation of the results focused on paclitaxel as the eluted drug. When we change the drug on the stent to sirolimus, we also need to shift the range of the design space significantly because of sirolimus' different therapeutic window. Fig. 3.6 A depicts the results

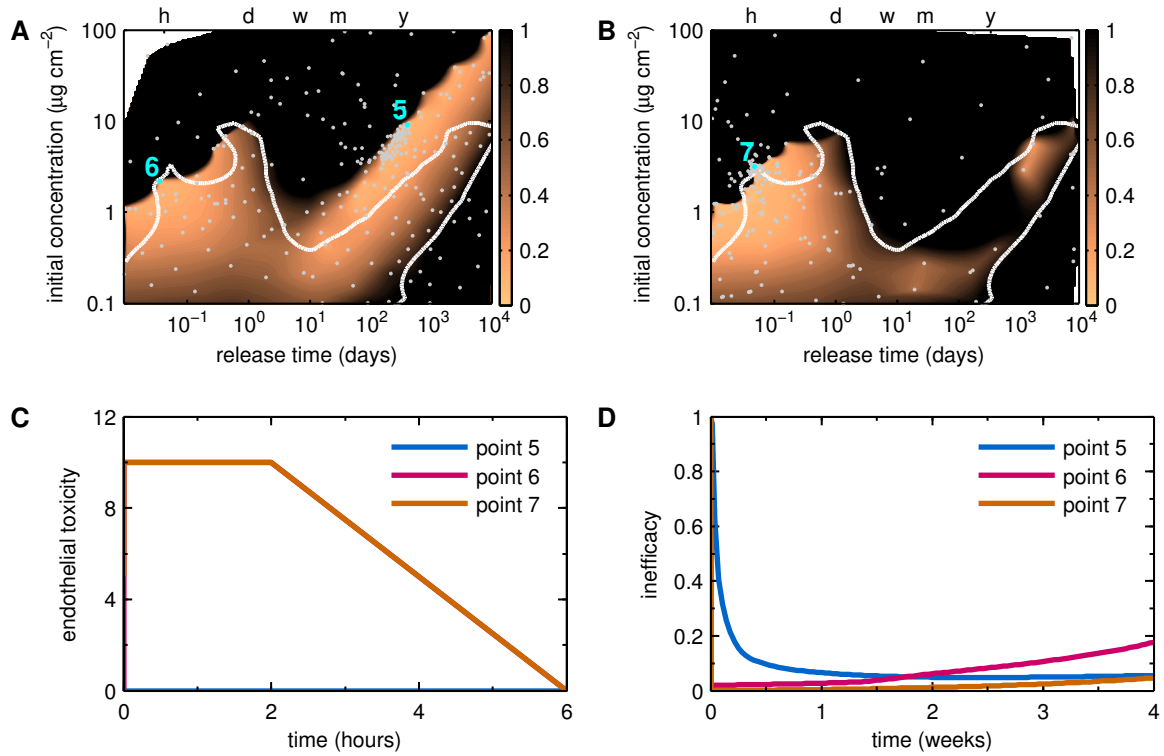
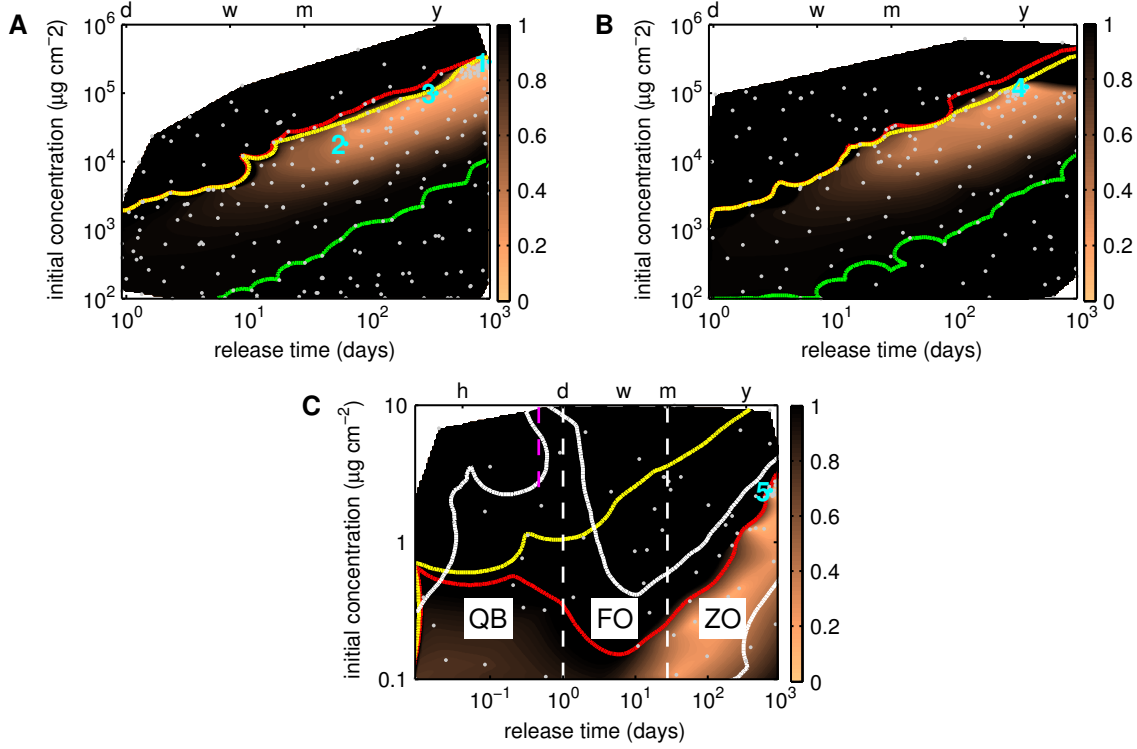


Figure 3.5: Filled contour plot of the cost function over the design space of *initial concentration in the stent polymer* c_0 and *release time* t_E for a paclitaxel-eluting stent with **A**: endothelium denuded both upstream and downstream of the stent and **B**: drug initially only loaded in the polymer part embedded in the arterial wall. The scale for the cost function representation is truncated at a maximum of 1; all values larger than 1 are colored black. The white contour line traces $J_{ETH} = 1$ for the baseline optimization (Fig. 3.3). The horizontal axis on top of the plots marks the time points of 1 (h)our, 1 (d)ay, 1 (w)EEK, 1 (m)ONth and 1 (y)EAR. **C** and **D**: Time evolution of the endothelial toxicity (T_e) and medial inefficacy (I_m) scores for the representative design points 5 - 7 shown in panels A and B and summarized in Table 3.2. In panel C, points 6 and 7 overlap.

of the baseline optimization (denuded endothelium in the stented portion but intact otherwise) for sirolimus. The results offer a very different picture from the case of paclitaxel: there is only a single, narrow, band of optimal release starting at a characteristic release time of ≈ 9 weeks with an initial concentration of $\approx 1.8 \cdot 10^4 \mu\text{g cm}^{-2}$ (point 2) and ending at the global optimum point (point 1) with a release time of ≈ 2.5 years and an initial concentration of $\approx 2.8 \cdot 10^5 \mu\text{g cm}^{-2}$. The detailed scores shown in the accompanying table reveal that within this optimal band, the designs gain in efficacy at the expense of increasing toxicity in the media.

The optimal band in Fig. 3.6 A is bounded on one side by the region of unacceptably high drug toxicity both in the media and at the luminal surface (delineated respectively by the yellow and red contour lines which nearly overlap), and on the other side by the zone of unacceptably low drug efficacy in the media (delineated by the green contour line).

Fig. 3.6 B depicts the contour plot of the optimization when the endothelium is also denuded upstream and downstream of the stent. The results demonstrate that the effect of additional endothelial denudation is minimal. Differences between the two cases can only be found in small details: the optimum value shifts to a lower concentration at an increased



| # | c_0 (mol m ⁻³) | D_c (m ² s ⁻¹) | J | \bar{I}_m | \bar{T}_{ses} | \bar{T}_m |
|---|------------------------------|---|------|-------------|-----------------|-------------|
| 1 | $2.8 \cdot 10^5$ | $1.0 \cdot 10^{-18}$ | 0.10 | 0.096 | 0 | 0.012 |
| 2 | $1.8 \cdot 10^4$ | $1.5 \cdot 10^{-17}$ | 0.30 | 0.30 | 0 | 0 |
| 3 | $9.7 \cdot 10^4$ | $2.7 \cdot 10^{-18}$ | 0.14 | 0.14 | 0 | 0 |
| 4 | $1.2 \cdot 10^5$ | $2.6 \cdot 10^{-18}$ | 0.19 | 0.18 | 0 | 0.025 |
| 5 | 2.4 | $1.2 \cdot 10^{-18}$ | 0.10 | 0.10 | 0 | 0 |

Figure 3.6: Sirolimus optimization. **A:** Filled contour plot of the cost function over the design space of *initial concentration in the stent polymer* c_0 and *release time* t_E under baseline conditions. The scale for the cost function representation is truncated at a maximum of 1; all values larger than 1 are colored black. The green contour line traces $\bar{I}_m = 1$, the yellow contour line $\bar{T}_m = 1$, and the red contour line $\bar{T}_e = 1$. **B:** Similar simulation but with the endothelium also denuded upstream and downstream of the stent. **C:** Sirolimus simulation using the therapeutic window previously used for paclitaxel. The white contour traces $J_{ETH} = 1$ of the default paclitaxel optimization (Fig. 3.3) for comparison. The white dashed vertical lines separate the three regions of *quasi-bolus*, *first-order* and *zero-order* release kinetics. The dashed magenta line marks the time scale for drug unbinding. The horizontal axis on top of the plots marks the time points of 1 (h)our, 1 (d)ay, 1 (w)EEK, 1 (m)onth and 1 (y)ear. Detailed scores of the representative design points 1 - 5 are summarized in the table.

release rate (point 4 in the table of Fig. 3.6), but the medial toxicity and efficacy scores are not much different from the equivalent point 3 of the baseline optimization run. Moreover, the toxicity and efficacy contour bounds follow largely the same behavior in both cases.

Figure 3.6 C depicts what the optimization would yield had we assumed sirolimus to have the same efficacy and toxicity thresholds (and hence the same therapeutic window) as paclitaxel. This efficacy threshold would only be about a factor of five higher than the minimum effective concentration observed in experiments. It is important to point out the different axes of this plot relative to those in Figure 3.3 A. The contour plot is somewhat similar to the paclitaxel baseline case, but it exhibits only a single optimal region in the zero-order kinetics valley. Notably, the yellow and red contour lines respectively marking a value of 1 for the medial and endothelial toxicity score shift towards lower concentrations; the yellow contour shifting significantly by almost an entire order of magnitude. Moreover, the inefficacy border in the southeast zone disappears. The breakdown of the score of the global optimum (point 5) is very similar to that of the optimum of the baseline sirolimus optimization, the only difference being that instead of a small medial toxicity score, this point has a very small SES toxicity score.

Figure 3.7 *Left* depicts the sirolimus concentration distribution in the arterial wall at one week post implantation for the optimal drug delivery strategy under baseline conditions (point 3 in Fig. 3.6 A). This time point corresponds to the highest toxicity levels in the arterial wall. Drug concentration is highest near the stent struts, surpassing the 1% toxicity threshold as indicated by the magenta contour line. Almost the entire remaining therapeutic domain has attained efficacious drug concentration levels, as can be seen by the green contour line engulfing most of the medial domain. Figure 3.7 *Right* shows the concentration distribution of the optimum at the one-week time point assuming the wider therapeutic window corresponding to paclitaxel. In this case, the highest concentration close to the struts does not surpass the maximum toxic concentration. The green contour line confirms that concentrations are effective in the entire medial domain. The distribution is, however, less homogeneous than the one on the left.

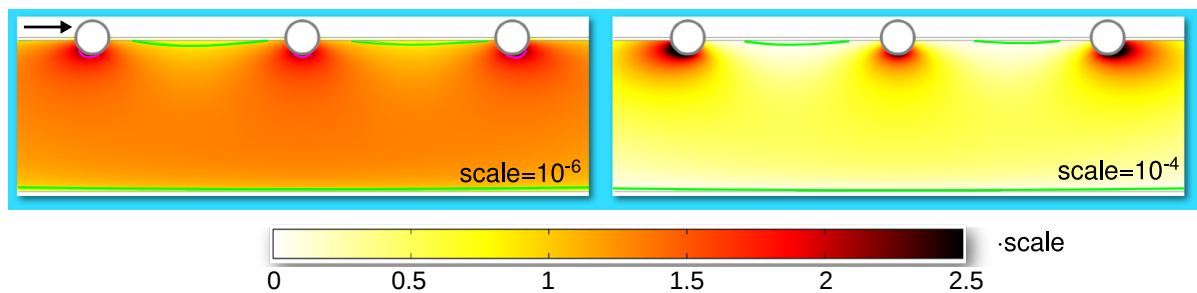


Figure 3.7: Normalized concentration distribution for optimal release from a sirolimus-eluting stent at one week post implantation. *Left*: Narrow therapeutic window; *Right*: wide therapeutic window corresponding to the toxicity and efficacy thresholds of paclitaxel. The green contour line traces the threshold between efficacious and non-efficacious drug concentration in the media, while the magenta contour (close to the struts) denotes concentrations 1% higher than c_{tox} . The arrow points in the direction of luminal flow.

3.4 Discussion

In this chapter, we used the surrogate management framework to optimize drug delivery from paclitaxel- and sirolimus-eluting stents. The design parameters in the optimization were the drug release rate and the initial drug concentration loaded onto the stent. The results revealed dramatically different results for the two drugs, primarily attributable to their different therapeutic windows, i.e. their efficacy and toxicity thresholds as well as differences in reaction kinetics. We now wish to summarize our findings and to gain insight into the physical basis of the optimization results. Given the assumptions that we have made and the degree of simplification in our numerical model of drug transport, we will refrain from denoting one particular combination of design parameters as *the* optimum and rather focus on a broader description of regions in the design space identified in the optimization.

3.4.1 Paclitaxel-eluting stents require quasi-bolus or zero-order drug release kinetics to avoid adverse concentration levels at the endothelium

Optimization of paclitaxel-eluting stents (P-DES) led to a design space that is divided into four zones. The first zone is characterized by initial drug concentrations higher than $10 \mu\text{g cm}^{-2}$. This zone has no acceptable designs regardless of drug release kinetics. The sub- $10 \mu\text{g cm}^{-2}$ area contains the remaining three zones of which only the designs with a quasi-bolus or zero-order release kinetics lead to acceptable designs, while any designs with first-order release kinetics result in undesirable conditions in the arterial wall.

Detailed inspection of the simulation results reveals that what primarily limits the efficacy of a particular P-DES design is the excessive supply of drug to the SES, leading to concentrations that are expected to inhibit EC proliferation. In the computations, we assumed drug concentration in the SES to be determined by convection and diffusion only; this is expected to lead to lower drug concentrations in the SES than would be the case had we also taken into account drug reaction in the SES. In principle, the reaction model that we used to describe drug-tissue interaction in the media can be extended to the SES.

The baseline simulations assumed that the endothelium was denuded in the stented segment of the artery but intact both upstream and downstream of the stent. Our simulations demonstrated that the optimization results are not very sensitive to the extent of endothelial denudation around the stent. Removing the endothelium merely reduced the size of the mountain of endothelial toxicity and shifted its southern rim to higher concentrations while not affecting the $10 \mu\text{g cm}^{-2}$ demarcation described above. Given that typical P-DES in clinical use sit on top of this mountain and beyond the $10 \mu\text{g cm}^{-2}$ limit, our results shed insight into one aspect of the multi-factorial reasons for the sometimes poor re-endothelialization of P-DES [19, 50]. Especially notable is the observation of focal cell necrosis close to stent struts associated with high-load P-DES, which is not surprising in light of the present results [49, 152].

Based on the present findings, we propose a number of recommendations for improved drug delivery strategies from P-DES. The first recommendation would be to lower the initial drug load by an order of magnitude and to shift the designs to slower release kinetics on the order of several months or even a year. The combination of the wide therapeutic window of paclitaxel and its long retention properties ensures sufficient efficacy in the media while the slow release of the drug precludes adverse concentrations at the endothelial surface.

The long retention capabilities of paclitaxel also open up a second possible strategy: quick unloading of the drug within hours thereby flushing the entire wall with paclitaxel and then

letting arterial wall drug kinetics do the rest. This strategy is largely similar to the idea of a drug-eluting balloon. If administered at the right concentration and in the right time frame, the binding process takes up as much drug as is required to provide effective drug concentration levels in the entire therapeutic domain for weeks. The initial short concentration spike should pose no significant problems from the standpoint of re-endothelialization because the endothelium in the vicinity of the stent struts is severely denuded during the first few days, and the extent of re-endothelialization in the first few days is quite limited in any case. Though promising, the outcomes associated with this strategy are expected to be quite sensitive to changes in the convective field within the arterial wall; therefore, a more accurate assessment of this field is probably needed before implementation of such a strategy.

A third possibility to address the difficulties associated with paclitaxel is to position the drug onto the stent in such a manner that it is as far away from the endothelial surface as possible. The optimization performed with our model where only the abluminal half of the coating contained drug showed, however, that it is not sufficient to only coat the abluminal side (as is done for example on the BioMatrix[®] stent by Biosensors). More elaborate designs, like drug-filled stent designs where the drug reservoir is inside of the stent body and the drug is eluted directly into the arterial wall via small holes (currently developed by Medtronic) or stents where small drug patches are applied only to the very abluminal surface of the stent body (like for example the JACTAX HD stent by Boston Scientific) appear to be more promising.

3.4.2 Sirolimus-eluting stents require zero-order release kinetics due to sirolimus' weak retention capabilities

Aside from the differences in their biological mode of action [112], the most significant difference between sirolimus and paclitaxel is the factor of 20 that separates their time scales of unbinding. Despite sirolimus' very high lipophilicity (approximately three times higher than paclitaxel), its weak retention capability requires constant supply of fresh drug from the stent and renders the design of a sirolimus-eluting stent (S-DES) with quasi-bolus release kinetics unfeasible. This sirolimus-specific feature has been reported in the literature [66]. The recent redesign of the zotarolimus-eluting Endeavour Resolute (Medtronic) stent (zotarolimus is a derivative of sirolimus) is another example highlighting this requirement: the release time was increased from 2 weeks in the initial design to 4 months due to the poor restenosis outcome of the original design [68, 90].

Time scale restriction aside, it should be noted that the kinetic properties of sirolimus make it a desirable drug for the design of DES: the high lipophilicity renders transport process in the arterial wall largely independent of changes in the convective field and thus predictable and robust. Furthermore, initial sirolimus concentration in the stent polymer can be used to tune the concentration profile to the requirements in the arterial wall, whether the therapeutic window is wide or narrow. Additionally, cytotoxicity is less of an issue for this drug due to its cytostatic mode of action. On the other hand, the lipophilicity of sirolimus also leads to more pronounced concentration peaks close to the stent struts which might compromise tissue integrity and explain the increased rate of stent strut malapposition observed with S-DES [108].

3.4.3 Low-dose P-DES and S-DES with zero-order release kinetics lead to a similar shape of the cost function

Comparing the contour plots of the cost function for paclitaxel and sirolimus with a narrow therapeutic window, we can identify large similarities between the two drugs in the zero-order release kinetics region. In this region the release from the stent coating is quasi-steady and the concentration on the stent surface remains nearly constant over the entire period considered. The time scales of transport and reaction in the arterial wall are all significantly faster than the release time scale and we can thus assume that a quasi-steady state is established in the arterial wall. For the case of constant surface concentration or equivalent constant surface flux, strongly lipophilic drugs (like paclitaxel and sirolimus) have very similar transport dynamics in the arterial wall that can be categorized depending on whether or not the applied surface concentration/flux exceeds a well defined threshold [179].

In the case of *above-threshold* drug supply, drug concentration in the arterial wall exceeds the binding capacity of the arterial wall and drug transport is increased since significant amounts of drug are now in the mobile unbound state. In the case of *sub-threshold* drug supply, drug concentration in the arterial wall is below the binding capacity of the arterial wall, and drug transport is considerably decreased since the drug is now mostly in the bound and thus immobile state. For paclitaxel and sirolimus this threshold is on the same order of magnitude as their respective binding capacities. The cost function enforces that drug concentration throughout the arterial wall remains below the toxic concentration threshold, which in the case of P-DES and the S-DES optimization with the same therapeutic window is below the respective binding capacities. Thus, by design of our cost function, the optimal slow-release P-DES and low-dose S-DES both fall into the sub-threshold category, hence explaining the similarity of the resulting cost function surfaces in the region of zero-order release kinetics. The optimized high-dose S-DES falls in the above-threshold category.

3.4.4 The cost function responds to drug kinetics in the arterial wall

The shapes of the landscape of the cost function for both paclitaxel and sirolimus are a mere reflection of the drug-related processes in the artery, confirming that the initial goal of creating a cost function that scores designs rather than forcing designs in a distinct direction could be achieved. At the same time, it leaves the designer with a necessary degree of liberty allowing him to weigh the severity of inefficient designs against designs that surpass preset concentration thresholds in a physically meaningful way. The very conservative approach of choosing very strict penalties at the toxic limit has identified stent designs of high efficacy throughout the period of the first four weeks after stent implantation, almost entirely avoiding any exposure of the endothelium to adverse and the media to toxic concentrations. Finally, comparing the concentration distributions of optimal S-DES for the two different therapeutic windows, we were able to show that it is possible to control the degree of concentration distribution homogeneity in the arterial wall without including a direct measure of homogeneity in the cost function.

3.4.5 Paclitaxel vs. sirolimus: a settled debate?

About a decade ago the FDA approved the first two DES: one eluting sirolimus (Cypher stent by Cordis) and the other eluting paclitaxel (Taxus stent by Boston Scientific). When we look at the current generation of DES that are either commercially available or at the clinical research stage, the initial 50:50 split has shifted significantly in favor of sirolimus and its derivatives

to the point where P-DES appear almost “exotic” [61, 62]. This trend appears to be driven by clinical evidence which often ranks first- and second-generation S-DES ahead of their P-DES counterparts [1, 20, 151, 168, 174]. Another explanation may be the aforementioned robustness of sirolimus alluded to above.

However, our results also offer a different perspective on the sub-optimal performance of P-DES: the applied concentrations and associated release kinetics in first-generation P-DES might just have been unsuited for the kinetics of paclitaxel. Other numerical studies (see Chapter 2 or [124]) and several experimental studies [49, 50, 102, 152] point in a similar direction. The recent success of paclitaxel-coated balloons [6, 37, 66, 158] indicates a level of incompletely tapped potential of paclitaxel.

Late stent thrombosis remains the biggest risk in the clinical use of DES. The occurrence of this viscious complication is strongly correlated with delayed endothelial healing [19, 53, 69, 74]. The cost function developed in the present study operates on the premise that drug concentrations between efficacious and toxic levels would lead to favorable stent outcomes. What is not accounted for in this model is a dependence of the efficacy and/or toxicity on the amount of time that the tissue has been exposed to a certain concentration, i.e. the cumulative dose. While both paclitaxel and sirolimus show dose-dependent behavior [7, 57, 87, 94, 142, 165], it is not clear how cumulative dose affects delayed endothelial coverage. If cumulative drug dose plays an important role in delaying arterial re-endothelialization, then sirolimus would be less flexible in its application than paclitaxel.

Optimizing the Strut Design of Paclitaxel- and Sirolimus-Eluting Stents

4.1 Introduction

Drug-eluting stents (DES) have revolutionized the treatment of occlusive coronary disease. By coating existing bare-metal stents (BMS) with an anti-proliferative drug that is released in a controlled manner into the arterial wall, the occurrence of in-stent restenosis has been reduced from $\approx 30\%$ to less than 5%. Shortly after the introduction of first generation DES, major safety concerns were raised: early data [173] suggested that the overall rate of late stent thrombosis (LST) of DES was significantly increased compared to BMS. Although these concerns have been ameliorated for second generation DES [157], the long-term safety of DES (especially after cessation of anti-thrombotic treatment [26, 145]) remains a controversial and timely topic in the design of DES [83].

LST is an incompletely understood complication that is associated with a particularly high mortality rate when it occurs. Currently, a low incidence rate of LST is assured with post-surgical anti-coagulation medication. The ideal duration of this treatment is currently unknown and is a controversial topic [34, 67, 88, 143, 167, 184, 194]. It appears, however, that LST is strongly related to poor and delayed recovery of the endothelial cell layer damaged by DES implantation [53, 54, 69]. Delayed endothelial healing is a more acute problem for DES than BMS and is thought to be related to the effect of the anti-proliferative drug, traditionally sirolimus (or one of its derivatives) or paclitaxel, on endothelial cell wound healing. As we showed in Chapter 3, drug release kinetics of DES can lead to drug concentration levels at the endothelial surface that would inhibit the proliferation of endothelial cells and thus interfere with stent strut re-endothelialization. However, drug release kinetics cannot entirely explain poor endothelialization of DES that can be observed up to 5 years after surgery [151], long after all of the drug has been eluted from the stent. Therefore, there is a need to better understand factors that influence re-endothelialization following DES deployment.

Implantation of a stent (BMS or DES) in an artery perturbs the arterial flow field around the stent struts and downstream of the stent [18, 31, 44, 149, 163]. Endothelial cells are known to

exquisitely respond to hemodynamic forces [32, 33, 42] which can even affect wound healing [64]. Changes in the local flow field at the site of stent implantation have also been associated with the incidence of in-stent restenosis and stent thrombosis [96].

In a review of first generation DES, Pendyala et al. conclude that “the optimal DES should have minimal impact on endothelial cell structural and functional recovery along with maximal inhibitory effect on SMC proliferation and migration” [144]. Considering the multiplicity of physical phenomena involved, devising an optimal DES becomes quite a challenge. An added source of complexity is that the fluid dynamics in the lumen and the drug transport in the arterial wall are coupled [11, 127, 128, 162, 183]. Accounting for all contributing phenomena leads to complex computational models (see Chapter 2, [24, 51, 139]) that are expensive to evaluate.

Studies that have performed optimization of stent design have often focused on minimizing blood flow disturbance in the arterial lumen [9, 70, 71, 171], but also stresses in the stent itself [196] or stresses in the arterial wall [178]. Pant and collaborators conducted the most comprehensive optimization to date by including multiple objectives and multiple physical phenomena [140, 141]. More specifically, they incorporated six performance measures including fluid dynamic stent performance metrics based on time-dependent momentum transport and drug-related metrics based on steady drug transport. Other studies optimized geometric features of stents including stent strut width [140, 171], stent strut height [171], the number of consecutive stent segments [70, 71], and the shape of stent strut connectors [141] with either circular or rectangular stent struts. The time-dependent character of drug transport and its effect on optimal strut shapes as well as optimal properties of polymeric stent coatings for the two different drugs have not been included in these studies.

A second issue stemming from the complexity of the computational model is that classical optimization methods are rendered unfeasible by the very long computational time necessary to explore a multi-dimensional parameter space. A very common optimization framework used with this type of expensive computational models is the surrogate management framework (SMF) [23]. This method has previously been applied to the optimization of aerospace [118, 119] and bioengineering [120, 198] problems. In all of these studies, a Cartesian lattice is used to discretize the design space, i.e. the parameter space that is explored by the optimization. Belitz and Bewley [16, 17] demonstrated that the use of other lattices with a denser and more regular discretization of the design space can lead to significantly improved performance of these algorithms in finding an optimal design.

The primary purpose of the present chapter is to determine optimal stent strut designs for DES eluting paclitaxel or sirolimus. The design objective is to maximize drug efficacy in the arterial wall while avoiding adverse concentrations and simultaneously minimally disturbing the flow field in the lumen. Optimal designs are identified by a novel SMF optimization algorithm [16, 17] that uses a lattice with optimal discretization properties to discretize the design space of the parameters that define the stent strut design. The strut shape can be varied continuously from circular to rectangular. Cost function scores are determined from the drug concentration distribution and luminal flow field obtained by the numerical simulation of the computational model of drug transport in stented arteries described in Chapter 2. A sensitivity analysis on the cost function reveals that the optimal properties of single-layered polymer coatings of DES which were previously determined (see Chapter 3) can be re-used in the context of the present strut design optimization. Our results demonstrate that optimal strut designs need to be tailored to the drug transport in the arterial wall.

The analysis of the cost function also motivates a second set of optimization runs which

aim at identifying optimal properties of two-layered polymer coatings where an additional thin top-coat encases a thicker polymeric layer. The thick layer contains either of the two drugs paclitaxel or sirolimus while the thin top-coat is void of drug. This investigation complements our previous investigation of optimal one-layered polymer coating properties (see Chapter 3). In addition to the initial concentration and diffusion coefficient of the drug in the thick polymeric layer, we optimize the thickness of this layer and the permeability of the additional top-coat. The results of this study demonstrate that an optimal polymer coating of paclitaxel-eluting stents can be relatively thin and does not require a top-coat while an optimal coating for sirolimus-eluting stents needs to be thick with an added top-coat.

4.2 Materials and methods

4.2.1 Computational model

We will begin by briefly recalling the most important features of the computational model used to carry out the numerical simulations. A detailed discussion of this model can be found in Chapter 2. We consider a 2D axisymmetric straight arterial segment of radius $r_l = 1.5$ mm within which a model drug-eluting stent (DES) with three struts spaced at intervals of 0.7 mm is deployed (Fig. 3.1 A). We define the strut shape using the so-called ‘‘Superformula’’ [63]:

$$r(\beta) = \left[\left| \frac{1}{a_s} \cos\left(\beta \frac{m_s}{4}\right) \right|^{n_2} + \left| \frac{1}{b_s} \sin\left(\beta \frac{m_s}{4}\right) \right|^{n_3} \right]^{-1/n_1} \quad \text{with } \beta \in [0, 2\pi] \quad (4.1)$$

The six parameters of the Superformula ($a_s, b_s, m_s, n_1, n_2, n_3$) allow the generation of a large diversity of shapes. Fixing $m_s = 4$ and setting $n_1 = n_2 = n_3 = n$ restricts the set of attainable shapes to variations ranging from diamonds ($n = 1$, Fig. 4.1 A) to rectangles ($n \gg 1$, Fig. 4.1 C). The parameters a_s and b_s set the semi-strut height a_s and width b_s , respectively. Setting $n = 2$ we recover the familiar equation describing an ellipse (Fig. 4.1 B). A $10 \mu\text{m}$ -thick polymer coating containing the drug is applied to the stent strut reflecting typical dimensions of second generation DES [164]. We apply the transport model of Chapter 2 to the elution of the two commonly used hydrophobic drugs paclitaxel and sirolimus.

We use two different configurations of the computational model for the simulations. The first configuration considers an endothelium that is completely denuded within the stented portion of the vessel but intact otherwise (configuration E1 in Fig. 3.1 A). The second configuration considers endothelium that is denuded not only in the stented zone but also upstream and downstream of the stent for a distance half the length of the inter-strut spacing and intact otherwise (configuration E2 in Fig. 3.1 B). The two different assumptions result in a change in the convective field in the arterial wall around the upstream and downstream strut due to

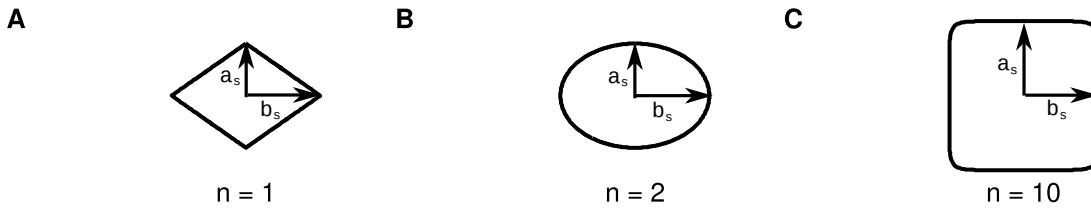


Figure 4.1: Different shapes generated with the Superformula. A: diamond; B: ellipse; C: rectangle.

the shielding function of the endothelium (see Chapter 2 Fig. 2.6). We define the *therapeutic domain* as the volume of the arterial wall containing the stent and extending by $2/3$ of the stent length both upstream and downstream of the stent.

In the literature, the drug concentration that is initially loaded onto a DES is typically presented in terms of drug mass per unit stent strut surface area [152]. However, the physically relevant quantity is the drug concentration in the polymer coating. In Chapter 3, the thickness and shape of the polymer coating were constant, so we could simply convert the drug concentration to drug mass per unit strut surface area. In the present chapter, the shape and thickness of the polymer coating are variable, so we will express drug load in terms of concentrations, since the conversion to drug mass per unit strut surface area depends on the coating thickness.

4.2.2 Cost function

In this chapter, we propose the following total cost function to measure the quality of a stent design:

$$J(\mathbf{x}_i) = J_{\text{ETH}}(\mathbf{x}_i) + w_{\text{FDI}} J_{\text{FDI}}(\mathbf{x}_i), \quad (4.2)$$

where J_{ETH} (defined and discussed in Chapter 3) is the drug-related cost function related to drug efficacy, toxicity, and homogeneity; J_{FDI} is the flow-related cost function which will be defined below; and w_{FDI} is a weight factor that establishes the relative weight of the flow-related cost function relative to the drug-related cost function. We will refer to a stent design as the set of d design variables (e.g. semi-strut height a_s , semi-strut width b_s , and strut shape exponent n) $\mathbf{x}^{(i)} = (x_1 \ x_2 \ \dots \ x_d)^T$ that determine a particular stent strut shape. As detailed in Chapter 3, minimizing J_{ETH} aims to provide a therapeutically efficacious but sub-toxic drug concentration in the media, minimal drug concentration at the luminal surface, and maximal homogeneity of the drug concentration in the media. To this function we now add J_{FDI} whose minimization is intended to minimize the extent of luminal flow disturbance induced by the stent [31, 149]. This is motivated by studies that have established that flow perturbations in the form of low shear stress or recirculating flow zones can greatly hinder the healing of a damaged endothelium [33, 64].

The drug-related cost function J_{ETH} was defined in Chapter 3 as:

$$J_{\text{ETH}}(\mathbf{x}) = \bar{I}_m + \frac{1}{3} (\bar{T}_1 + \bar{T}_{\text{ses}} + \bar{T}_m) + \bar{H}_m. \quad (4.3)$$

and is thus the sum of three scores: the inefficacy score \bar{I}_m , the arithmetic average of the three toxicity scores \bar{T}_1 , \bar{T}_{ses} and \bar{T}_m , and the homogeneity score \bar{H}_m . Each score is spatially averaged in the therapeutic domain and temporally averaged over a period beginning with stent deployment and ending after four weeks (t_{end}) of drug elution.

The score J_{FDI} portion of the cost function measures the flow disturbance in the lumen induced by the presence of a stent and is given as follows:

$$J_{\text{FDI}}(\mathbf{x}) = \min(\text{FDI}, 1) \quad (4.4)$$

where the Flow Disturbance Index (FDI) is defined as:

$$\text{FDI} = \frac{1}{S_w} \int_{S_w} \left| \frac{\tau - \tau_0}{\tau_0} \right| dS, \quad (4.5)$$

similar to [70, 71]. It evaluates the deviation of the local wall shear stress (WSS) τ from the unperturbed WSS τ_0 that would exist in the vessel in the absence of the stent and averages this quantity over the surface S_w . In the present study, the surface S_w spans the area of the luminal surface of the arterial wall that begins at the upstream end of the therapeutic domain and ends at the downstream end of the computational domain. Even though our model stent only consists of three consecutive struts, the work of Seo *et al.* [163] showed that three consecutive struts are sufficient to approximate the degree of flow disturbance.

We assume blood to be a Newtonian fluid with density $\rho = 1060 \text{ kg m}^{-3}$ and dynamic viscosity $\mu_b = 3.5 \cdot 10^{-3} \text{ Pa s}$. This assumption is reasonable given the shear rate values under consideration for the flow conditions of interest (luminal Reynolds number $\text{Re}_l = 400$). For fully developed flow through a circular cross-section vessel pipe with radius r_1 :

$$\tau_0 = \frac{2\mu_b^2 \text{Re}_l}{r_1^2 \rho}. \quad (4.6)$$

The present work focuses on steady flow. However, were we to consider time-dependent flow, then the WSS τ in Eq. (4.5) would be replaced by its time-average over a pulsatile cycle. For the extreme case of purely oscillatory flow with a zero mean, $\tau = 0$, yielding an FDI value of 1. Because purely oscillatory flow leads to vascular inflammation and dysfunction, we will consider this condition as the worst possible flow condition and consequently limit the FDI at an upper value of 1 as indicated in Eq. (4.5).

Optimization in the present chapter is performed using the aggregate cost function J defined in Eq. (4.2). This requires a choice of the weight factor w_{FDI} . Without experimental evidence of the relative importance of an optimal drug concentration distribution in the arterial wall (as defined above) vs. having a stent design that minimally disturbs the flow field, the choice of w_{FDI} is arbitrary. We use a baseline value of $w_{\text{FDI}} = 0.5$ in the majority of the optimization runs but also briefly probe the effect of this parameter on the results.

A common approach to avoid using arbitrary weight factors in the cost function of multi-objective optimization problems is to refrain from forming an aggregate cost function (sometimes referred to as a utility function [153]) and instead searching for the pareto optimal design of the different objectives [56, 140, 153]. A design is pareto optimal when a small deviation in any of the design variables leads to an improvement in one of the objectives only at the expense of another objective. Pareto optimal designs are thus typically non-unique, and identifying them is an involved and computationally expensive process. On the other hand, the use of an aggregate cost function as we have done here (J (Eq. (4.2))) allows us to create a fully automated and efficient algorithm that, based on the *a priori* choices made by the designer, yields a unique optimal design.

4.2.3 Optimization method

In this chapter, the goal is to identify the design which yields the lowest possible score of the cost function J (Eq. (4.2)). Solving such an optimization problem is often associated with gradient-based methods that estimate gradients of the cost function with respect to the design variables in order to determine the direction of decreasing cost function. These methods are known to have excellent convergence properties and can assure convergence to a minimum; however, this class of methods requires the cost function to be continuously differentiable and the gradient to be easy to obtain [153]. Furthermore, gradient methods can only search for

a local minimum and will miss the global minimum that cannot be reached by a continuously descending path from the initial guess.

In the present study, the cost function value is estimated using the computational model described in Chapter 2. The model is implemented in the commercial multi-physics finite element solver COMSOL and can require several hours of computation time for one evaluation. We have thus no prior knowledge of the shape or differentiability of the cost function hypersurface in the design space. Considering the computational cost, the use of gradient-based optimization methods is intractable. We thus rely on the derivative-free optimization method described below.

Basic concept of the optimization method

We use an optimization algorithm based on the Surrogate Management Framework (SMF) [23] to minimize the cost function J (Eq. (4.2)). Following evaluation of an initial set of designs, SMF algorithms use a succession of search and poll steps to identify the optimal design of the cost function (Fig. 4.2). In the *search step* a Kriging model [97, 122] interpolating the cost function (called the surrogate) is used to inexpensively scan the space of possible designs (called design space) for prospective optimum points. The Kriging model is an interpolation (and extrapolation) function based on previously evaluated designs which estimates the value of the cost function and the uncertainty of the prediction for new designs of the design space (Fig. 4.3). The predicted value and its uncertainty are combined to calculate the probability that a new design would improve by a defined margin the cost function value of the best design that has been identified to this point. Maximizing this probability of improvement is used to identify new prospective optimal designs.

The cost function of the determined prospective optimal design is then evaluated using the direct numerical simulation of the computational model. If this computed cost function score J is smaller than the value of J of the current optimal design, then the new design and the value of the cost function J are added to the Kriging model to generate a new interpolation surrogate and the search step is repeated. Otherwise, a *poll step* is initiated which numerically computes the value of J for new designs with design variables closer to the current optimal design. Failure to identify a new optimum in the poll step results in a refinement of the grid on which new designs are looked for in the design space. All newly evaluated designs and their respective computed value of the cost function are again added to the Kriging model and a new search step is initiated.

The following two key novelties have been implemented in the present SMF algorithm leading to improved performance of the optimization procedure: 1) The arrangement of different designs is on a grid with a higher number of directly neighboring designs than in the case of the typically used Cartesian grid [70, 118–120, 198]. 2) The factor by which the grid is refined after a failed poll step is reduced compared to other algorithms so that the number of designs that can be investigated in each poll step increases without having to pick designs that are very close to the current optimal design (see Fig. 4.4 and the discussion below for details).

In the following section we will discuss the SMF algorithm in more depth. We will outline the derivation of Kriging, detail some of the particularities of our method, and highlight the extensions made to the code (generously supplied by our UCSD collaborators Belitz and Bewley). A detailed description including studies investigating the performance of the method can be found in [16] and [17].

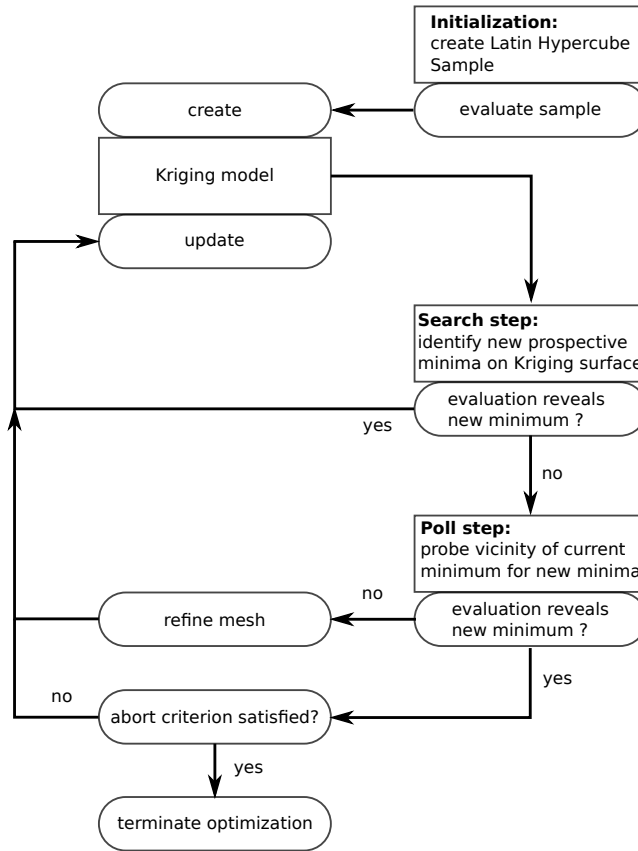


Figure 4.2: Flow diagram of the optimization algorithm and its coupling to the computational model.

Detailed description of the optimization method

Definitions: Before we begin the more detailed description of the optimization method, we need to define a few terms that will be useful throughout the remainder of this section:

- *design variable* x_i : property of a stent which is to be optimized, e.g. stent semi-strut height a_s , stent semi-strut width b_s , or strut shape exponent n .
- *design range*: For each design variable a range of interest is specified in which the optimization shall be performed. The range is bounded by “soft” constraints which can be overcome by the optimization algorithm in certain cases. For some design variables, “hard” constraints can be defined reflecting physical considerations that are not considered by the computational model and thus should not be overcome by the algorithm. See the section *Implementing constraints as well as encountering infeasible designs and failed function evaluations* below for more details.
- *design* $\mathbf{x}^{(i)} = (x_1 \ x_2 \ \dots \ x_d)^T$: vector of d design variables defining a particular stent design.
- *design (hyper-)space* $\mathbb{D} = \mathbb{R}^d$: space of all possible designs. Each design variable forms an axis of the design space. All designs are located on a grid that discretizes the design space with a grid size $G^{(k)}$ (minimum distance between two design variables). To avoid any bias

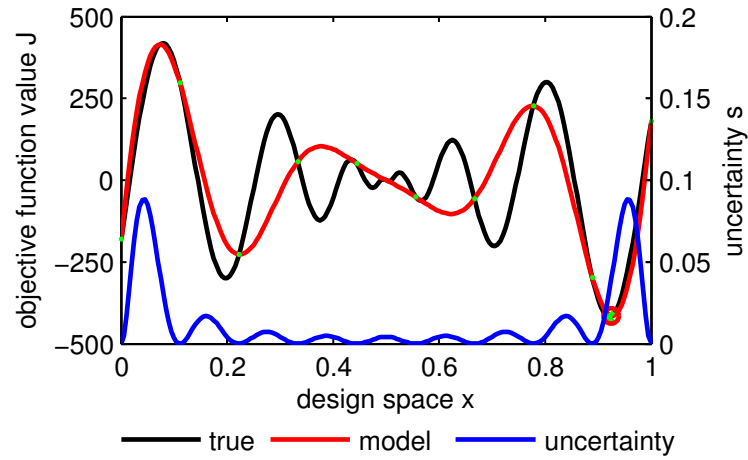


Figure 4.3: One-dimensional example of a Kriging interpolation hypersurface (red) of the true cost function hypersurface (black) based on 10 evaluated points P (green) with uncertainty s (blue) over the design space x . The design space x and the cost function values form the cost function hyper-space. The true cost function minimum (green cross) could almost perfectly be identified by the Kriging model (predicted minimum marked by red circle) with only 10 points.

or distortion of the optimization procedure related to different dimensions or units of the design variables, the d design variables are mapped onto the unit hyper-cube $\mathbb{D}^* = [0, 1]^d$ based on the range of the soft constraints [56, 153]. Our initial grid is discretized by 6 grid points per design variable [16] and thus the initial grid size $G^{(0)} = 1/5$.

- *cost function (hyper-)surface* $J(\mathbf{x}) \subset \mathbb{O}$: true surface of the cost function.
- *cost function (hyper-)space* $\mathbb{O} = \mathbb{R}^{d+1}$: space in which the hypersurface of the cost function J lies.
- *surrogate (hyper-)surface* $\hat{J}(\mathbf{x}) \subset \mathbb{O}$: estimated surface of the cost function surface obtained via interpolation and extrapolation of a Kriging model.
- *current optimum design (COD)* \mathbf{x}^{COD} : design that yields the lowest cost function J^{COD} value among all evaluated designs up to the current iteration.
- *search direction*: vector connecting the \mathbf{x}^{COD} and a design $\mathbf{x}^{(*),i}$ that is designated for evaluation in the current iteration.
- indices i, j : $i, j \in (0, 1, 2, \dots)$, $\mathbf{x}^{(i)}$, $\mathbf{x}^{(j)}$ denote different designs.
- index k : $k \in (0, 1, 2, \dots)$, $G^{(k)}$ is the grid size after k grid refinements.

Generating a surrogate surface via Kriging: Kriging [97, 122] is the essential tool used in the search step of the SMF algorithm to generate an estimated cost function surface that reflects the trends of previously evaluated designs. We will thus outline the major steps in the derivation

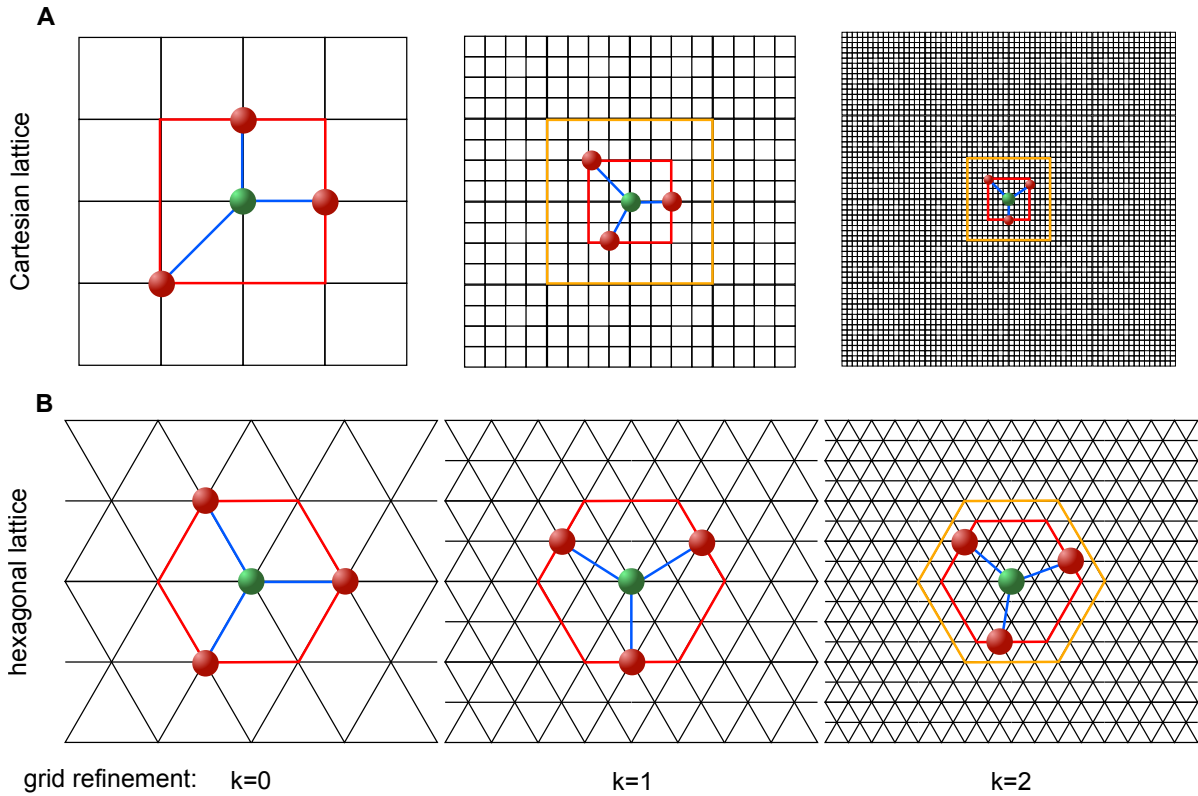


Figure 4.4: Polling the design space. **A:** Two consecutive factor of 4 grid refinements and factor of 2 shell of prospective polling designs refinements of the LT-MADS algorithm on a 2-dimensional Cartesian lattice; **B:** Two consecutive factor of 2 mesh refinements of the λ -MADS algorithm on a hexagonal lattice A_2 with a shell of prospective polling designs at a distance of 1, 2 and 3 grid points for the initial grid ($k = 0$) and after $k = 1$ and $k = 2$ consecutive grid refinements, respectively. Search directions (in blue) of a minimal positive basis connect the current optimum design (in green) with the selected poll designs (red). Current shell of prospective polling designs is marked in red, previous shell of prospective polling designs is marked in orange.

of this method. The interested reader is advised to consult Jones *et al.* [86] or Forrester *et al.* [56] for an excellent review of the method.

The fundamental assumption of Kriging is that the cost function value $J^{(i)}$ of a design $\mathbf{x}^{(i)}$ is the observation of a normally distributed random process with mean μ and standard deviation σ . Furthermore, we are going to assume that the random processes of two different designs $\mathbf{x}^{(i)}$ and $\mathbf{x}^{(j)}$ are correlated by the expression:

$$\phi(\mathbf{x}^{(i)}, \mathbf{x}^{(j)}) = \exp\left(-\sum_{l=1}^d \theta_l |x_l^{(i)} - x_l^{(j)}|^{p_l}\right)_{ij}. \quad (4.7)$$

The two parameters θ_l and p_l , which are the most notable difference between this correlation and the standard Gaussian distribution formula, serve as tuning parameters of the Kriging model. These parameters are tuned during the derivation of the Kriging model such that the shape of the surrogate surface has the highest probability of correctly mimicking the trends

of previously evaluated designs. A low value of θ_l leads to a wider shape of the Gaussian bell function indicating less variation of the surrogate surface along the design variable x_l . p_l ranges from 0 to 2 whereby values in the lower range indicate a rather discontinuous shape and $p_l = 2$ characterizes a smooth shape. To save time in the optimization, we will omit the optimization of the exponents p_l and simply fix a value of $p_l = 2$ [56].

Based on n_{eval} previously-evaluated designs $\mathbf{X} = \left(\mathbf{x}^{(1)} \mathbf{x}^{(2)} \dots \mathbf{x}^{(n_{\text{eval}})} \right)^T$ with cost function values $\mathbf{J} = \left(J(\mathbf{x}^{(1)}) J(\mathbf{x}^{(2)}) \dots J(\mathbf{x}^{(n_{\text{eval}})}) \right)$, the Kriging model estimates the cost function value of a new and unknown design $\mathbf{x}^{(*)}$ as:

$$\hat{J}(\mathbf{x}^{(*)}) = \hat{\mu} + \hat{\boldsymbol{\psi}}^T \hat{\boldsymbol{\Psi}}^{-1} (\mathbf{J} - \mathbf{1}\hat{\mu}) \quad (4.8)$$

where

$$\hat{\boldsymbol{\Psi}} = \left(\hat{\phi}(\mathbf{x}^{(i)}, \mathbf{x}^{(j)}) \right)_{ij} \quad \text{with } i, j = 1, \dots, n_{\text{eval}} \quad (4.9)$$

is the correlation matrix of all previously evaluated designs,

$$\hat{\boldsymbol{\psi}}^T = \left(\hat{\phi}(\mathbf{x}^{(1)}, \mathbf{x}^{(*)})^T \dots \hat{\phi}(\mathbf{x}^{(n_{\text{eval}})}, \mathbf{x}^{(*)})^T \right) \quad (4.10)$$

is the correlation vector of the previously evaluated designs with the unknown design, and $\mathbf{1}$ is an $n_{\text{eval}} \times 1$ vector of ones. $\hat{\phi}$ is a similar correlation expression to that in Eq. (4.7) except that the tuning parameters θ_l and p_l are replaced by their optimal values $\hat{\theta}_l$ and \hat{p}_l . To obtain the optimal parameters $\hat{\theta}_l$ and $\hat{\mu}$ (remember we do not optimize for \hat{p}_l), we start by expressing the likelihood of observing \mathbf{J} given the parameters μ and σ :

$$L = \left(2\pi\sigma^2 \right)^{-n_{\text{eval}}/2} |\boldsymbol{\Psi}|^{-1/2} \exp \left[-\frac{1}{2\sigma^2} (\mathbf{J} - \mathbf{1}\mu)^T \boldsymbol{\Psi}^{-1} (\mathbf{J} - \mathbf{1}\mu) \right]. \quad (4.11)$$

Maximizing this likelihood with respect to σ and μ yields the optimal values

$$\hat{\mu} = \frac{\mathbf{1}^T \boldsymbol{\Psi}^{-1} \mathbf{J}}{\mathbf{1}^T \boldsymbol{\Psi}^{-1} \mathbf{1}}, \quad (4.12)$$

$$\hat{\sigma}^2 = \frac{1}{n_{\text{eval}}} (\mathbf{J} - \mathbf{1}\hat{\mu})^T \boldsymbol{\Psi}^{-1} (\mathbf{J} - \mathbf{1}\hat{\mu}). \quad (4.13)$$

Plugging these values back into Eq. (4.11) and optimizing the likelihood function numerically with Brent's method (a modified bisection method) [25] yields the optimal parameters $\hat{\theta}_l$.

We have obtained the model parameters that are most likely to yield the observed cost function values \mathbf{J} of our designs. Given this model, we now wish to obtain the most likely prediction of a cost function value \hat{J} for a new design $\mathbf{x}^{(*)}$. We thus add the predicted objective value \hat{J} to obtain $\tilde{\mathbf{J}} = (\mathbf{J} \hat{J})^T$ together with the new design to the rest of the designs which yields an additional correlation vector $\hat{\boldsymbol{\psi}}$ (Eq. (4.10)) and the augmented correlation matrix

$$\tilde{\boldsymbol{\Psi}} = \begin{pmatrix} \hat{\boldsymbol{\Psi}} & \hat{\boldsymbol{\psi}} \\ \hat{\boldsymbol{\psi}}^T & 1 \end{pmatrix}. \quad (4.14)$$

Plugging $\tilde{\boldsymbol{\Psi}}$, $\hat{\boldsymbol{\psi}}$, $\hat{\boldsymbol{\theta}}$, $\hat{\boldsymbol{p}}$, $\hat{\mu}$ and $\hat{\sigma}$ into Eq. (4.11) and maximizing the resulting expression with respect to \hat{J} finally gives Eq. (4.8). This value has an associated uncertainty that can be

derived as the mean squared error of a Gaussian process [155]:

$$\hat{s}^2(\mathbf{x}^{(*)}) = \hat{\sigma}^2 \left(1 - \hat{\boldsymbol{\psi}}^T \hat{\boldsymbol{\Psi}}^{-1} \hat{\boldsymbol{\psi}} + \frac{\left(1 - \mathbf{1}^T \hat{\boldsymbol{\Psi}}^{-1} \hat{\boldsymbol{\psi}}\right)^2}{\mathbf{1}^T \hat{\boldsymbol{\Psi}}^{-1} \mathbf{1}} \right). \quad (4.15)$$

In our implementation we omit the last term of this equation which is very small and prone to cause numerical issues.

Initializing the optimization algorithm: In the initial step of a SMF algorithm, a sample of $10d$ designs is distributed over the design space which serves as the basis of the first Kriging model. We use the latin hypercube sampling algorithm presented in [56] to assure a uniform distribution of these points throughout the design space.

The global search step: The purpose of the search step is to explore the entire design space for prospective new designs that minimize the cost function and then evaluate these prospective designs with the expensive computational model to obtain the true cost function value. We saw above that a Kriging model inexpensively yields a prediction of the cost function value $\hat{J}(\mathbf{x}^{(*)})$ as well as the associated uncertainty $\hat{s}^2(\mathbf{x}^{(*)})$ for unevaluated designs based on previously evaluated designs. The uncertainty is maximal in between and zero at already evaluated designs (Fig. 4.3). Instead of searching the surrogate surface directly for minima, Jones *et al.* [86] recommend the following strategy: given a target $T_G = J^{\text{COD}} - \alpha (J^{\text{max}} - J^{\text{COD}})$ for improvement over the COD (J^{COD}), we can evaluate the likelihood that a certain design $\mathbf{x}^{(*)}$ improves the COD by at least this value. Minimizing the expression [86]:

$$\frac{\hat{J}(\mathbf{x}^{(*)}) - T_G}{\hat{s}(\mathbf{x}^{(*)})} \quad (4.16)$$

(which is equivalent to maximizing the likelihood of improvement) with a conjugate gradient method will then reveal a prospective design $\mathbf{x}^{(*)}$ that has a high likelihood of having a lower cost function value than the COD. The choice of α controls whether this search in the design space will be more exploratory (meaning scanning the entire design space) or local (looking in the vicinity of the COD). As the density of evaluated designs around the COD increases, the uncertainty about this region decreases. Eventually the uncertainty $\hat{s}(\mathbf{x}^{(*)})$ of designs close to the COD approaches 0 and the ratio in Equation (4.16) becomes very large, driving the search step towards unexplored regions of the design space away from the COD.

The convergence rate of this method is highly sensitive to the choice of the control parameter α which sets the target value of improvement for the search. The optimal choice of this value is not only tied to the optimization problem at hand but might also change during the course of the optimization. While in the beginning of the optimization larger (and thus more exploratory values) are desirable, a smaller value of α might be necessary to speed up the convergence to the optimum once the design space has been scanned sufficiently. To solve this issue, we investigate 10 values of α spanning the range from 0 to 3 in every search step as suggested by Jones *et al.* [86] to ensure that at every iteration candidate designs emerge that are close to the optimum as well as in less explored regions of the design space. To maximize the performance of this method, the search and evaluation of the different candidate designs is performed in parallel and as soon as one of these evaluations yields a lower cost function, the search step is deemed *successful* and a new search step is initiated with the newly evaluated points added to

the Kriging model. The search step is repeated until no new point can be identified in which case a poll step is initiated around the COD.

The local poll step: The poll step of the SMF algorithm investigates the vicinity of the COD for designs that yield lower cost function values than the COD. This assures convergence of the algorithm to a design for which gradients of the cost function with respect to the design variables vanish [95]. We use a novel Mesh-Adaptive Direct Search (MADS) algorithm, dubbed λ -MADS [16], in the poll step. To explain the concept of this MADS algorithm, it is helpful to remain in a two-dimensional example as depicted in Fig. 4.4 B, with the understanding that all of the following can be extended to higher dimensions. After a failed search step, we are now looking at the COD (the green point) on our initial grid (discretizing the design space) with grid spacing $G^{(0)}$.

Starting from the COD, a set of $d + 1 = 3$ search directions is chosen on the grid which positively spans the design space, meaning that any grid point of the design space is expressible as a linear combination of these search directions with only positive coefficients. The first of these search directions (the *seed search direction*) is chosen at random while the remaining two search directions are the solutions of the Thomson problem [177] which seeks the equilibrium solution of equally charged particles distributed on a (hyper-)sphere. The length of these search directions is exactly one grid size. The designs that are at the tip of these search directions (marked with red points) will then be polled, meaning their cost function values will be evaluated using our computational model. All prospective designs that could be polled lie on the hexagon around the COD marked in red; we call this set of designs the *shell of prospective polling designs* (henceforth referred to simply as shell). If any of these polled designs yields a cost function value that is lower than the cost function value of the COD, the poll step is deemed *successful*, otherwise it is deemed to have *failed*. Independent of the outcome, the evaluated designs and their respective cost function values are added to the Kriging model and a new search step is initiated (we call this updating the Kriging model).

If the poll step fails, then we will also reduce the grid size by a factor of 2 (the number of grid refinements is thus $k = 1$) and the shell will be moved to a distance of $k + 1 = 2$ grid points. This means for the first grid refinement that the shell will remain at the same distance, however, with an increased number of prospective polling designs. Again a set of search directions is determined (with a random seed search direction) and the selected designs polled. To avoid selecting the same poll designs as in the previous iteration, these designs will be assigned a smaller charge, thus diverting the equilibrium search of the Thompson algorithm to other designs. If the poll step fails again, the grid is again refined by a factor of 2 ($k = 2$) and the width of the new shell is moved to a distance of 3 grid points, which corresponds to $3/4$ of the width of the previous shell (marked in orange).

If, on the other hand, the poll step is successful, then the grid size remains constant and the seed search direction will be the same as the previously successful search direction. After two successful poll steps, the grid is coarsened by a factor of 2 (meaning that k is reduced by one) and the distance of the shell adjusted accordingly.

Separating refinement of the grid from the refinement of the shell is the key advantage of MADS algorithms compared to other direct search algorithms since in every iteration the number of search directions increases. Eventually, the search directions become dense in the design space, a property of these algorithms which can assure convergence to a local optimum [2]. A key novelty of λ -MADS compared to other MADS algorithms like LT-MADS [10] is that these refinements are slowed down (see Fig. 4.4 A for a two-dimensional example). Typically a factor of 2 refinement is chosen for the shell and a factor of 4 for the mesh. The advantage

of slowing down the refinement is that the number of search directions is increased without drastically reducing the size of the shell at the same time.

Laminated lattices at the heart of the optimization algorithm: The second novelty of the SMF algorithm used in this study, which was introduced by Belitz and Bewley [16, 17], was to break with the paradigm of using a Cartesian lattice to discretize the design space and use more uniform and densely packed lattices instead (meaning every grid point has a larger number of directly neighboring grid points). For every dimension d a lattice can be found that maximizes these two properties, the so called laminated lattices λ_d : this is in two dimensions the hexagonal lattice A_2 , in three dimensions the face-centered-cubic lattice A_3 and in four dimensions the checkerboard lattice D_4 . An overview of the theory behind these lattices can be found in [16, 17]. Belitz and Bewley [16, 17] were able to show that using laminated lattices significantly improves the performance of SMF algorithms. If we compare the initial grids in Fig. 4.4, we see that the Cartesian lattice has only 4 direct neighbors while the hexagonal lattice has 6 and the $d + 1$ search directions are perfectly isotropic compared to the search directions of the LT-MADS algorithm. These benefits account in part for the improved performance of the current SMF algorithm.

Implementing constraints as well as encountering unfeasible designs and failed function evaluations: The searching procedure of the search step is restricted to a set of constraints on the design space that are defined *a priori*. The constrained search is realized by penalizing search results that violate these constraints by a dynamically adjusted weighting factor. We call these constraints soft constraints, since the search can still converge on a design outside of the borders of these constraints if the prospect of finding improved designs is so high that it surpasses those of the designs that lie inside the constraints. Moreover, the poll step is an unconstrained optimization algorithm *per se* and can explore the design space far beyond the soft constraints. The advantage of having soft constraints is that it gives the designer some flexibility regarding the definition of the design space. The designer might, for example, have envisioned a certain range of a design variable to be explored during the optimization, which is not based on any physical constraints. If, however, the optimization algorithm discovers that significantly superior designs can be found outside of this range, the algorithm has the possibility to explore them.

Other design constraints might have physical bases that are not considered by the computational model and are thus undesired by the designer. If the search or poll step encounters a design that goes beyond these hard constraints, the cost function is not evaluated and the design is imputed with a value that corresponds to

$$J(\mathbf{x}^{(i)}) = J_{\text{imp,hard}}(\mathbf{x}^{(i)}) = \hat{J}(\mathbf{x}^{(i)}) + 2\hat{s}^2(\mathbf{x}^{(i)}) . \quad (4.17)$$

This strategy of assigning a value is inspired by Forrester *et al.* [56] who suggest imputing the values of designs that lead to failed function evaluation by their predicted value $\hat{J}(\mathbf{x}_i)$ plus a penalty corresponding to the square of the uncertainty at the design \mathbf{x}_i :

$$J(\mathbf{x}^{(i)}) = J_{\text{imp,fail}}(\mathbf{x}^{(i)}) = \hat{J}(\mathbf{x}^{(i)}) + \hat{s}^2(\mathbf{x}^{(i)}) . \quad (4.18)$$

This method ensures that the algorithm is diverted from the design without exceedingly distorting the surrounding interpolation model. We adopted the same strategy in our algorithm when a cost function evaluation failed.

Quality management of the Kriging model: As the optimization algorithm progresses, the design space becomes more and more explored and the underlying mesh gets increasingly

refined. After a number of mesh refinements the density of polling points increases significantly and design clusters are formed. This causes the correlation matrix, required in the process of generating the Kriging model, to become ill-conditioned which results in an inaccurate Kriging model [23, 56]. One way to address this issue is to add a small constant to the leading diagonal of the correlation matrix and generate a Kriging model with regression [23, 56]. Although the Kriging model obtained is no longer an exact interpolation of the data points, the quality of the Kriging model is not compromised.

We have developed an alternative approach to tackle this issue by filtering the data points used to create the Kriging predictor and hence thinning the clusters in the design space responsible for the ill-conditioned matrix. First we determine the average minimum Euclidean distance of our data points, which serves as an upper bound $f_{\text{filt,max}}$ of the filtering process, and the minimum Euclidean distance of our data points, which marks the lower bound $f_{\text{filt,min}}$. Starting from the current optimum design (COD), we now filter (remove) any points within the hyper-sphere of radius $f_{\text{filt,min}}/2$ that have a higher cost function value than the COD. This procedure is then repeated for the point with the lowest cost function value among the remaining points and so on. Once all points have been filtered with the lowest filtering scale $f_{\text{filt}} = f_{\text{filt,min}}$, we attempt again to create the Kriging model. If the process fails again, then the filtering scale is increased by a factor of 2 and the filtering procedure repeated until the maximum filtering scale $f_{\text{filt,max}}$ is reached at which point the set of data points has been sufficiently thinned to allow the Kriging model to be computed.

This method has two key benefits: the Kriging model will still pass through the evaluated data points and since the minimum points in every filtered cluster are preserved, the search method will not be inclined to revisit the filtered regions. Moreover, even if we have removed some (less crucial) information from the Kriging model, we can leverage the filtered points to test the quality of the Kriging model during the current optimization.

Since we know the true cost function values of filtered points \mathbf{x}_{filt} , we can calculate a correlation coefficient r_{cor}^2 between the predicted values $\hat{J}(\mathbf{x}_{\text{filt}})$ and the true function values $J(\mathbf{x}_{\text{filt}})$ [56]

$$r_{\text{cor}}^2 = \left(\frac{\text{cov}(J(\mathbf{x}_{\text{filt}}), \hat{J}(\mathbf{x}_{\text{filt}}))}{\sqrt{\text{var}(J(\mathbf{x}_{\text{filt}})) \text{var}(\hat{J}(\mathbf{x}_{\text{filt}}))}} \right)^2$$

$$= \left(\frac{n_{\text{filt}} \sum_{i=0}^{n_{\text{filt}}} J^{(i)} \hat{j}^{(i)} - \sum_{i=0}^{n_{\text{filt}}} J^{(i)} \sum_{i=0}^{n_{\text{filt}}} \hat{j}^{(i)}}{\sqrt{\left[n_{\text{filt}} \sum_{i=0}^{n_{\text{filt}}} J^{(i)2} - \left(\sum_{i=0}^{n_{\text{filt}}} J^{(i)} \right)^2 \right] \left[n_{\text{filt}} \sum_{i=0}^{n_{\text{filt}}} \hat{j}^{(i)2} - \left(\sum_{i=0}^{n_{\text{filt}}} \hat{j}^{(i)} \right)^2 \right]}} \right)^2. \quad (4.19)$$

A high correlation coefficient indicates that the current Kriging model is capable of appropriately mimicking the trends of the cost function while a low value would indicate that either the Kriging model is missing important features of the cost function or that the cost function is very irregular. Beyond serving as a simple indicator of the quality of the Kriging model, this information could also be implemented as part of the termination strategy of the optimization.

Terminating the optimization algorithm: The optimization is terminated when we consider the design space exhaustively explored. In our definition, this point is reached when the

following three criteria are met:

1. The mesh of the poll step was 10-fold refined.
2. At least as many search directions were polled on this finest mesh as there are direct neighbors to the COD.
3. 5 consecutive search steps failed following these poll steps.

4.2.4 Sensitivity estimation of the cost function to design variables and model parameters

Taking the physiological parameters of our computational model (Chapter 2) and the calibration parameters of the cost function as given, we are left with 10 parameters in our computational model that need specification (Table 4.1). The first group contains the geometric design variables that appear in the Superformula (Eq. (4.1)): the stent semi-strut height a_s , the stent semi-strut width b_s , and the strut shape exponent n . The indicated design range of a_s and b_s reflects the typical dimensions of modern stents (low end) up to the thicker struts of first generation DES [60]. The shape exponent covers the range of round ($n = 2$) to chamfered rectangular ($n = 6$) struts. These design ranges also indicate the bounds of the soft constraints used for the search step of the SMF algorithm. Values in parentheses mark hard constraints. The meaning of the sensitivity range will become evident in a moment.

The second group contains design variables that define the drug delivery strategy of the polymer coating (without specifying the exact type of release): the effective diffusion coefficient D_c which controls the release rate from the polymer coating, the drug concentration c_0 which is initially loaded in the polymer coating, the thickness of the polymer coating L_c , and the permeability P_c of a possible top-coat that encases the polymer. The highest value in these ranges ($D_c = 1 \cdot 10^{-13} \text{ m}^2 \text{ s}^{-1}$) is indicative of a rapid release of the drug (quasi-bolus release kinetics) and the lowest ($D_c = 1 \cdot 10^{-18} \text{ m}^2 \text{ s}^{-1}$) of concentration-independent long-term release (zero-order release kinetics). Whenever there are two rows of values for a design variable, the upper row of values corresponds to the range that we used for the optimization of paclitaxel-eluting stents (P-DES) while the lower row contains the range for the optimization of sirolimus-eluting stents (S-DES). We chose different ranges for paclitaxel and sirolimus based on our experiences in Chapter 3. The ranges of c_0 are also influenced by the results of Chapter 3; they do, however, contain the order of magnitude which can be found for typical P-DES and S-DES ($\approx 100 \text{ mol m}^{-3}$). The design range of L_c reflects the dimensions of typical DES. The upper end of the range of top-coat permeabilities ($P_c = 1 \text{ m s}^{-1}$) is in principle identical to a situation without any top-coat, while the low end ($P_c = 1 \cdot 10^{-10} \text{ m s}^{-1}$) represents a very resistant barrier to the elution of drug from the underlying polymer coating.

The third and final group contains parameters of the computational model that express assumptions we made in the computational model setup rather than actual variables of the stent design. The strut embedment p_{st} determines how far the struts of our model stent penetrate the arterial wall. This parameter represents the outcome of the implantation process rather than an actual variable that can be controlled. For all simulations, we assume the hypothetical situation where the stent is exactly half embedded into the arterial wall. The time parameter t_{end} controls the time period covered by the simulation and set as the target time for the evaluation of the cost function. We chose $t_{end} = 4$ weeks based on typical DES release times and motivated by the pathobiology following stent implantation [3, 94, 121, 150]. Finally, the parameter tpd_f

Table 4.1: Model parameters and design variables of the computational model with respective design and sensitivity ranges

| Symbol | Description | Sensitivity range | | Design range | | Unit |
|---|---------------------------|--------------------|--------------------|--------------------|--------------------|----------------------------|
| | | min | max | min | max | |
| <i>geometrical design variables</i> | | | | | | |
| a_s | semi-strut height | 25 | 75 | 25 (12.5) | 75 | μm |
| b_s | semi-strut width | 25 | 75 | 25 (12.5) | 75 | μm |
| n | strut shape exponent | 1.5 | 6 | 2 (1.5) | 6 | — |
| <i>design variables of two-layered polymer coatings</i> | | | | | | |
| c_0 | initial concentration | 0.1 | 100 | 0.1 | 100 | mol m^{-3} |
| | | 100 | $1 \cdot 10^5$ | 100 | $1 \cdot 10^5$ | |
| D_c | diffusion coefficient | $1 \cdot 10^{-18}$ | $1 \cdot 10^{-15}$ | $1 \cdot 10^{-18}$ | $1 \cdot 10^{-13}$ | $\text{m}^2 \text{s}^{-1}$ |
| | | | | $1 \cdot 10^{-17}$ | $1 \cdot 10^{-14}$ | |
| L_c | polymer coating thickness | 10 | 50 | 10 | 30 | μm |
| P_c | top-coat permeability | $1 \cdot 10^{-10}$ | 1 | $1 \cdot 10^{-10}$ | 1 | m s^{-1} |
| | | $1 \cdot 10^{-10}$ | 1 | $1 \cdot 10^{-10}$ | $1 \cdot 10^{-6}$ | |
| <i>parameters of the computational model</i> | | | | | | |
| p_{st} | strut embedment | 20% | 80% | 50% | | — |
| t_{end} | simulation time | 1 | 6 | 4 | | weeks |
| tpd_f | therapeutic domain size | 50% | 100% | 100% | | — |

defines the percentage of the radial width of the arterial wall that is considered to be part of the therapeutic domain in which the cost function is evaluated. In all simulations we set the therapeutic domain to span 100% of the arterial wall.

Estimated mean and standard deviation of elementary effects

The elementary effect $e_i^{(j)}$ of a design variable x_i at a design $\mathbf{x}^{(j)}$ on the cost function J is defined as [129]:

$$e_i(\mathbf{x}^{(j)}) = e_i^{(j)} = \frac{1}{\Delta} \left(J \left((x_1, \dots, x_i + \Delta, \dots, x_d)^T \right) - J \left((x_1, \dots, x_i, \dots, x_d)^T \right) \right) \quad (4.20)$$

where $\Delta = 1/(m-1)$ is the mesh size of the mapped design space (\mathbb{D}^* , where all design variables x_i are scaled to the interval $[0, 1]$) discretized by m mesh points per dimension ($m = 10$ in our case). An elementary effect is thus an evaluation of the gradient of the cost function J with respect to the design variable x_i at a design $\mathbf{x}^{(j)}$. If we distribute a number of n_{elem} ($n_{\text{elem}} = 5$ in our case) designs throughout the design space \mathbb{D}^* (following the randomized statistical process described in [129]) and evaluate their elementary effects $e_i^{(j)}$ at these designs, then the estimated mean value and standard deviation of the elementary effects $e_i^{(j)}$ of each design variable x_i gives an estimate of the importance of the design variable x_i for the cost function J : a large estimated mean (absolute value > 1) indicates that the cost function J is sensitive to variations of the design variable x_i (i.e. on average the non-dimensional gradients throughout the design space are large) and a large standard deviation (absolute value > 1) implies that the design variable x_i is involved in interactions with other variables (i.e. the non-dimensional gradients vary a lot throughout the design space).

4.3 Results

4.3.1 Sensitivity estimation of the cost function

We will first apply the sensitivity estimation method to estimate the importance of the design variables and model parameters shown in Table 4.1 for the flow-related (J_{FDI} , Eq. (4.4)) and the drug-related parts of the cost function (J_{ETH} , Eq. (4.3)). This approach has previously been suggested in [56]. Although the parameters p_{st} , t_{end} and tpdf_f (Table 4.1) of the computational model are not strictly speaking design variables, we will treat them as such for the first part of this section and will simply refer to the ensemble of design variables and computational model parameters as *parameters*.

We will consider four different cases in this analysis: two cases with paclitaxel as the eluted drug, once without a top-coat being applied to the polymer coating and once with a top-coat; and two cases with sirolimus again with and without a top-coat. All four cases consider an endothelium that is completely denuded within the stented portion of the vessel but intact otherwise (configuration E1 in Fig. 3.1 A). We will then discuss the importance of the parameters for the total cost function J (Eq. (4.2)). Afterwards we will be ready to determine the optimization runs considered in this chapter. The design range we investigated in the following analysis is indicated in the column “sensitivity range” of Table 4.1.

Since the estimated mean and standard deviation of the elementary effects of each parameter as depicted in Figs. 4.5 and 4.6 are based on a single random distribution of a small number

(5) of designs, the values are not fully converged and only the order of magnitude of these two quantities will be of interest.

Sensitivity estimation of the flow-related part of the cost function J_{FDI}

Fig. 4.5 depicts the estimated mean values and standard deviations of the elementary effects of each parameter on J_{FDI} . Only parameters that determine the geometry of the stent strut (a_s , b_s , n and L_c) or its embedment in the arterial wall (p_{st}) are important for J_{FDI} . For the other parameters, the estimated mean and standard deviation of their respective elementary effects is zero and thus J_{FDI} is neither sensitive to these parameters nor are these parameters involved in interactions with other parameters. Therefore, these parameters are not shown in Fig. 4.5. J_{FDI} is most sensitive to the strut embedment p_{st} since out of all considered parameters, the estimated mean value of the elementary effects of p_{st} is the largest. The strut embedment p_{st} is involved in interactions with other parameters since the standard deviation of the elementary effects of p_{st} is also the largest one. This is not unexpected since the embedment controls the degree to which the entire stent structure is exposed to luminal flow. The shape exponent n of the struts has a more significant effect on J_{FDI} than the semi-strut height a_s and the polymer coating thickness L_c . The flow disturbance caused by the stent is least sensitive to the semi-strut width b_s . The overall small magnitudes of the estimated mean values and standard deviations indicate that changes of the parameters in the considered ranges only lead to mild variations of J_{FDI} .

Sensitivity estimation for the drug-related part of the cost function J_{ETH}

Fig. 4.6 depicts the distribution of the estimated mean values and standard deviations of the elementary effects of the investigated parameters on J_{ETH} . In this figure, estimated means and standard deviations of the elementary effects of some of the parameters are not shown because their absolute values are negligibly small, indicating lack of sensitivity of the cost function to those parameters. The four panels correspond to the four different model setups discussed above: P-DES without (Fig. 4.6 A) and with (Fig. 4.6 B) a top-coat and S-DES without (Fig.

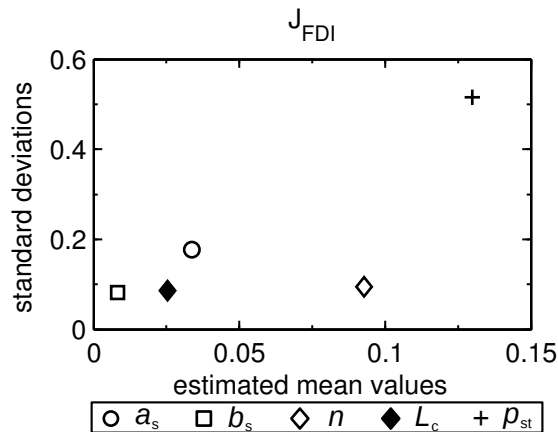


Figure 4.5: Sensitivity estimation of J_{FDI} . Distribution of the estimated mean values and standard deviations of the elementary effects of each parameter (see Table 4.1) on J_{FDI} (Eq. 4.4). Parameters with an estimated mean and standard deviation of elementary effects of zero are not shown.

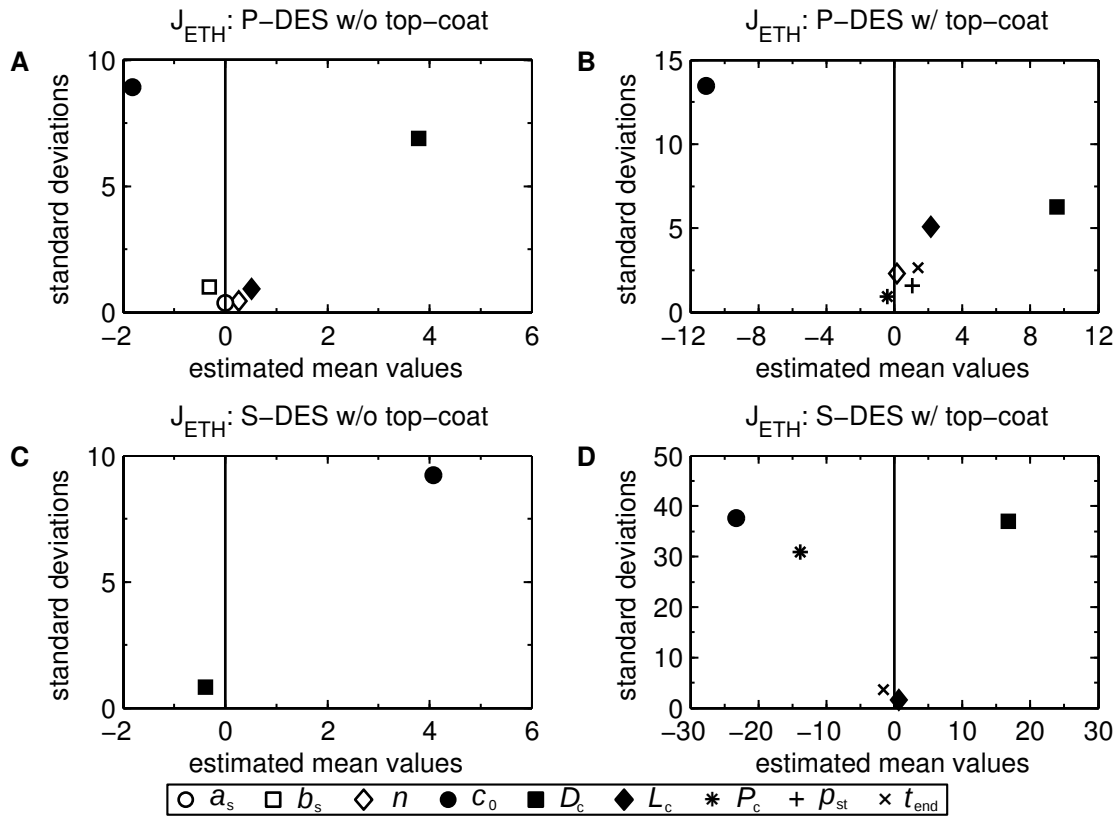


Figure 4.6: Sensitivity estimation of J_{ETH} . Distribution of the estimated mean values and standard deviations of the elementary effects of each parameter (see Table 4.1) on J_{ETH} (Eq. 4.3) for: **A**: P-DES without a top-coat, **B**: P-DES with a top-coat, **C**: S-DES without a top-coat, and **D**: S-DES with a top-coat. Parameters with an estimated mean and standard deviation of elementary effects of absolute value smaller than 1 are not shown.

4.6 C) and with (Fig. 4.6 D) a top-coat. For both DES drugs studied and regardless of whether or not a top-coat is applied (i.e. all four panels), the mean and standard deviation of the elementary effects of the initial concentration c_0 and the effective diffusivity in the polymer coating D_c have the largest absolute values. This indicates that these parameters have the strongest effect on J_{ETH} and that they exhibit the highest level of interaction with other design variables. For the case of S-DES without a top-coat (Fig. 4.6 C), The diffusivity D_c plays a smaller role relative to the initial concentration c_0 than in the other three cases. Interestingly, the thickness of the polymer coating L_c plays a role in the cost function of P-DES (Fig. 4.6 B) but not S-DES (Fig. 4.6 D). The permeability of the top-coat P_c is the third most important parameter for S-DES (Fig. 4.6 D) but is a much less significant parameter for P-DES (Fig. 4.6 B). The means and standard deviations of the elementary effects of the remaining parameters shown in Fig. 4.6 cluster closer to zero; however, since their absolute values are larger than 1, they do have an effect on J_{ETH} .

The stent strut geometric parameters a_s , b_s and n only play an important role in the design of P-DES and not S-DES (Fig. 4.6). The strut width b_s is the most dominant parameter amongst these if no top-coat is applied to the paclitaxel polymer coating (Fig. 4.6 A), while the strut shape exponent n is the only variable that influences the drug-related part of the cost function

for P-DES with a top-coat (Fig. 4.6 B).

Another interesting observation is that the extent of strut embedment p_{st} can have a significant effect on J_{ETH} but only for the case of P-DES with a top-coat (Fig. 4.6 B). The results also show that the simulation time t_{end} has a strong effect on J_{ETH} only for DES with a top-coat (Figs. 4.6 B and D). As long as the radial thickness of the therapeutic domain (controlled by tpd_f) is chosen to be larger than half of the arterial wall thickness, this thickness does not have a significant effect on J_{ETH} .

The last two observations concerning the simulation time t_{end} and the thickness of the therapeutic domain (controlled by tpd_f) have a rather simple explanation: the highest concentrations in the arterial wall during a simulation are encountered close to the stent struts and the endothelial surface and without a top-coat the highest concentrations typically occur within the first week of drug elution. A top-coat can significantly delay the incidence of highest concentration, causing drug concentration to reach efficacious levels very late. Therefore, the drug-related score of the cost function J_{ETH} becomes sensitive to variations of t_{end} beyond one week in the case of DES with a top-coat. Since the range investigated for tpd_f yields therapeutic domains that always include the highest computed concentrations, J_{ETH} is not affected by a variation of tpd_f over the range studied.

Sensitivity estimation of the total cost function J

We obtain the estimated mean value of the elementary effects of a parameter with respect to the total cost function J by adding the estimated mean value of the elementary effects of that parameter on J_{ETH} to the product of the estimated mean value of the elementary effects of that parameter on J_{FDI} and the FDI weight factor w_{FDI} . This summation does not hold for the standard deviation of elementary effects but it still gives a good estimate. Since the estimated sensitivity of J_{FDI} to geometric parameters (Fig. 4.5) is about ten times smaller than the sensitivity of J_{ETH} to these parameters (Fig. 4.6), only when the FDI weight factor w_{FDI} is larger than 10 does J_{FDI} play a significant role in the variation of the total cost function J . In such a case, the geometric parameters strut height a_s , width b_s , and shape exponent n to which J_{FDI} is sensitive will induce variations in J comparable to the variations induced through J_{ETH} by the parameters of the polymer coating drug delivery strategy, i.e. the initial concentration c_0 and the effective diffusion coefficient D_c . This implies that a value of w_{FDI} of order 1 or below will not significantly affect optimization of the total cost function J . In this case, we can separate the optimization of the drug delivery parameters from the optimization of the geometric parameters, since the impact of the geometric parameters on the optimum of the cost function J is negligible in comparison to the effect of the parameters that govern the drug delivery strategy.

4.3.2 Optimization results

We have performed two groups of simulation runs. The first group aims to determine optimal stent strut geometries, whereas the second group focuses on two-layered polymer coatings and aims to optimize the design of the stent coating. Both groups of optimization are investigated for stents eluting either paclitaxel or sirolimus.

Group 1: Optimization of stent strut design

In this group of simulations, the goal is to determine optimal strut geometries for stents eluting either paclitaxel or sirolimus. The three design variables used in the optimization are the semi-strut height a_s , the semi-strut width b_s , and the strut shape exponent n . Drug release is assumed to occur at the optimal slow-release values identified in Chapter 3, where drug release becomes concentration-independent and thus follows *zero-order release kinetics* (implying a low effective diffusivity D_c in the polymeric coating).

We carried out six optimization runs. Two runs, one with paclitaxel at low initial loading (henceforth referred to as low-dose P-DES) and one with sirolimus at a high initial loading concentration (high-dose S-DES), assumed a model configuration where the endothelium is denuded within the stented portion of the vessel and also upstream and downstream of the stent (configuration E2 in Fig. 3.1 B). Two runs, again one for low-dose P-DES and one for high-dose S-DES, were performed assuming that the endothelium is denuded within the stented portion of the vessel but intact otherwise (configuration E1 in Fig. 3.1 A). The fifth optimization run in this group was with low-dose S-DES with the goal of gaining insight into the extent to which the optimization results depend on the type of drug used or the initial loading concentration; this run was performed assuming the therapeutic window of paclitaxel and with endothelial model configuration E1. Finally, the sixth optimization run explored the consequences on the optimal design of choosing a large value for the FDI weight factor w_{FDI} . In this simulation, we set $w_{\text{FDI}} = 10$ (all other optimization runs in this group were performed with $w_{\text{FDI}} = 0.5$) and used low-dose P-DES in model configuration E1. In all optimization runs of this first group, the thickness of the polymer coating was set to $L_c = 10 \mu\text{m}$. An overview of the six Group 1 optimization runs is provided in Table 4.2.

Table 4.2: Group 1 optimization runs: strut design optimization with semi-strut height a_s , semi-strut width b_s , and strut shape exponent n as the design variables

| # | Figure ^a | Drug | Dose | Release | c_0 (mol m^{-3}) | D_c ($\text{m}^2 \text{s}^{-1}$) | c_{eff} (mol m^{-3}) | c_{tox} (mol m^{-3}) | Config. ^b | w_{FDI} ^c |
|---|---------------------|----------------|------|-----------------|----------------------------------|---|---|---|----------------------|-------------------------------|
| 1 | 4.8 A | P ^d | low | ZO ^f | 2.0 | $2.6 \cdot 10^{-18}$ | $1 \cdot 10^{-5}$ | $1 \cdot 10^{-2}$ | E2 | 0.5 |
| 2 | 4.9 A | P | low | ZO | 2.0 | $2.6 \cdot 10^{-18}$ | $1 \cdot 10^{-5}$ | $1 \cdot 10^{-2}$ | E1 | 0.5 |
| 3 | 4.10 | P | low | ZO | 2.0 | $2.6 \cdot 10^{-18}$ | $1 \cdot 10^{-5}$ | $1 \cdot 10^{-2}$ | E1 | 10 |
| 4 | 4.12 A | S ^e | high | ZO | $2.8 \cdot 10^5$ | $1.0 \cdot 10^{-18}$ | 0.29 | 0.73 | E2 | 0.5 |
| 5 | 4.13 | S | high | ZO | $2.8 \cdot 10^5$ | $1.0 \cdot 10^{-18}$ | 0.29 | 0.73 | E1 | 0.5 |
| 6 | 4.14 | S | low | ZO | 2.4 | $1.2 \cdot 10^{-18}$ | $1 \cdot 10^{-5}$ | $1 \cdot 10^{-2}$ | E1 | 0.5 |

^a figure depicting optimal strut design

^b model configuration of the endothelium as depicted in Fig. 3.1

^c FDI weight factor

^d P: paclitaxel

^e S: sirolimus

^f zero-order release kinetics, i.e. concentration-independent long-term release

Strut design optimization of paclitaxel-eluting stents

Optimization case 1: As indicated in Table 4.2, the first optimization is for a low-dose P-DES in configuration E2. In all of the simulations, we do not know the true shape of the cost function at every point in the design space. Rather, we can only rely on presenting designs that have actually been calculated during the optimization runs. Extracting detailed information from an interpolated representation of the three-dimensional hypersurface of the cost function that results from the optimization is challenging and can be deceiving, especially since the interpolation is only as good as the underlying calculated designs. Therefore, to better understand and more clearly present the results of the optimization, we use the following multi-step approach, which is explained with the help of the optimization results in Fig. 4.7 A for optimization case 1:

1. We selected sample sets of designs (among all simulated designs) for which the cost function was evaluated with two design variables kept approximately constant (within the constraints of the simulated designs) and the third one varied along its design range. For instance, in Fig. 4.7 A, the semi-strut width ($b_s = 68 \pm 1.1 \mu\text{m}$) and the strut shape exponent ($n = 5.1 \pm 0.63$) are fixed while the semi-strut height a_s is varied in the range $a_s = [14, 75] \mu\text{m}$.
2. Starting with the design for which the varied design variable is lowest, we compared the magnitudes of the contributing scores of the total cost function of two designs in increasing order of the varied design variable. In Fig. 4.7 A, the two scores that contribute to the value of the overall cost function are the inefficacy score in the media \bar{I}_m (black) and the flow disturbance score J_{FDI} (white).
3. From the comparison in the previous step, we estimated the trend of the contributing scores, i.e. whether these scores increased or decreased with an increase in the design variable. In Fig. 4.7 A, the inefficacy score \bar{I}_m and J_{FDI} both increase with increasing semi-strut height a_s .
4. We repeated steps 1-3 for different parts of the design space. If we observed the same estimated trend for each of these samples, then we considered the trend as *global*, i.e. valid for the entire design space. Fig. 4.7 A depicts a representative sample of the estimated global trend and can thus be understood as a discrete line cut through the three-dimensional cost function hypersurface along the semi-strut height a_s .

Fig. 4.7 B shows the evolution of the inefficacy score \bar{I}_m (black) and the flow disturbance score J_{FDI} (white) with increasing semi-strut width b_s . All values are normalized by their respective maximum score encountered among the depicted designs (marked by an \times). For a fixed strut height ($a_s = 45 \pm 27 \mu\text{m}$, Fig. 4.7 B) the inefficacy score \bar{I}_m decreases significantly with increasing b_s while J_{FDI} remains virtually constant in a range of $b_s = [27, 94] \mu\text{m}$.

Fig. 4.7 illustrates the following two global trends that can be observed for the cost function of the P-DES strut design optimization with an endothelial model configuration that assumes the endothelium denuded within the stented portion of the vessel and also upstream and downstream of the stent (configuration E2): 1) Thinner struts (smaller a_s) lead to decreased inefficacy scores \bar{I}_m (and hence to more efficacious stent designs) as well as to lower J_{FDI} (thus less flow disturbance). 2) Wider struts (larger b_s) improve (i.e. reduce) the inefficacy score \bar{I}_m .

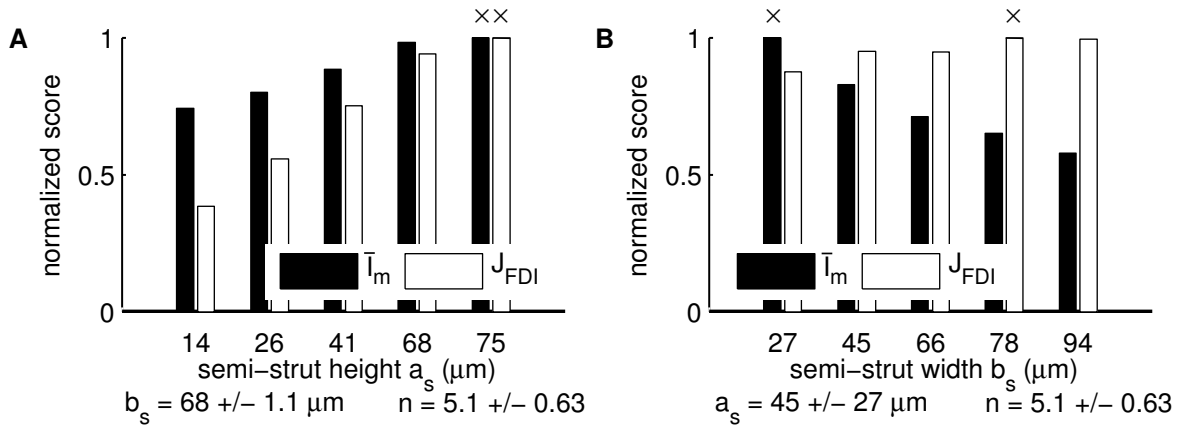


Figure 4.7: Optimization case 1: estimated global trends of the cost function of the P-DES (configuration E2) strut design optimization for a variation of semi-strut height a_s and semi-strut width b_s . Change in the inefficacy score \bar{I}_m (black bars) and flow disturbance score J_{FDI} (white bars) for increasing **A**: semi-strut height and **B**: semi-strut width. The scores are normalized by the maximum score among the presented designs which is marked by an \times .

Thus, a smaller semi-strut height a_s has a desirable effect on both the drug- and flow-related contributions to the cost function.

Fig. 4.8 A depicts the optimal strut shape that results from the optimization of P-DES in configuration E2. The optimal strut design has a small semi-strut height $a_s = 12.5 \mu\text{m}$, a large semi-strut width $b_s = 92.2 \mu\text{m}$ and a large shape exponent $n = 5.8$. Fig. 4.8 B and C depict two sub-optimal strut designs. The struts in both these cases have virtually identical semi-strut height and width with the major difference between them being their strut shape exponent n :

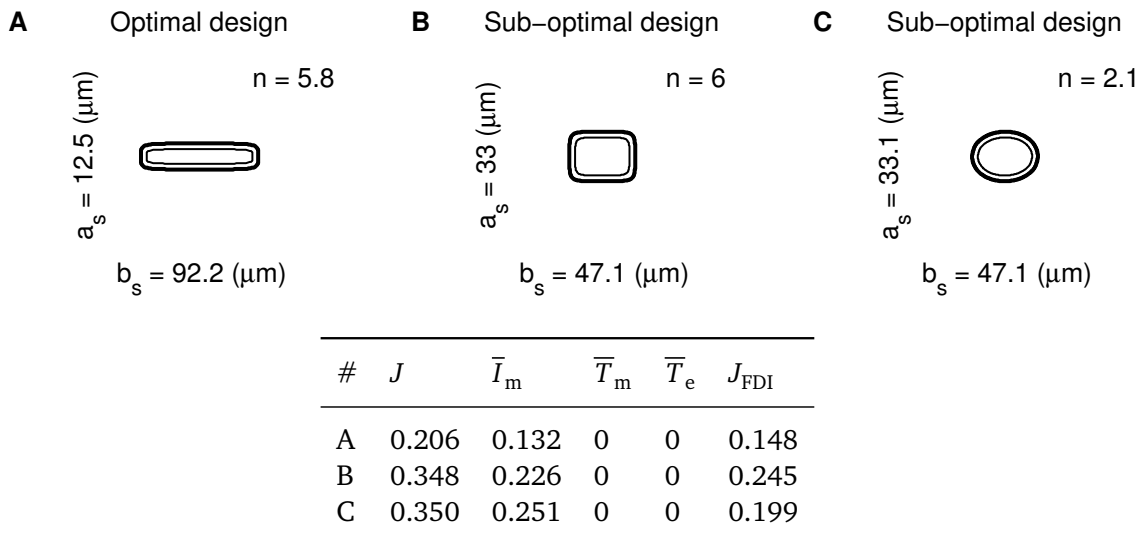


Figure 4.8: Optimization case 1: optimal P-DES strut designs compared to sub-optimal strut designs similar to commercial strut designs for $w_{\text{FDI}} = 0.5$ and configuration E2. **A**: Optimal strut design, **B**: strut design for high n , **C**: strut design for low n . The table provides the total score J and the contributing scores \bar{I}_m , \bar{T}_m , \bar{T}_e , and J_{FDI} for each strut design.

the strut in Fig. 4.8 B has an exponent at the upper end of the considered range ($n = 6$) which results in a rectangular shape, whereas the strut in Fig. 4.8 C has a small exponent ($n = 2.1$) resulting in an ellipsoidal shape. On the other hand, the optimal strut design is very elongated and extremely thin ($a_s = 12.5 \mu\text{m}$ is the hard constraint of the specified design range) compared to typical strut designs of current DES, which resemble those shown in Fig. 4.8 B and C.

The table in Fig. 4.8 shows that both toxicity scores (\bar{T}_m, \bar{T}_e) of the optimal strut design are zero, and the inefficacy score is $\bar{I}_m = 0.13$. With a J_{FDI} of 0.15, the total cost function value sums up ($w_{\text{FDI}} = 0.5$) to $J = 0.2$. The strut design of Fig. 4.8 B yields an increase in the total cost function score of 69% compared to the optimum. 66% of this change is due to an increased inefficacy score $\bar{I}_m = 0.23$ and 34% due to an increased $J_{\text{FDI}} = 0.25$. The strut design of Fig. 4.8 C results in an increase of 70% of the total cost function score relative to the optimal strut design. 82% of this increase can be attributed to $\bar{I}_m = 0.25$ and only 17% to an increase of $J_{\text{FDI}} = 0.2$. The toxicity scores remain 0 for both sub-optimal strut designs, similar to the optimal strut design.

The near three-fold size of the semi-strut minor axis a_s and the drastically reduced size of the semi-major axis b_s of both sub-optimal strut designs compared to the optimal strut design account to a large degree for the increased J_{FDI} and inefficacy \bar{I}_m scores. When we compare the scores of the two sub-optimal strut designs directly to one another, we can see that the high exponent n leads to an improved efficacy of the drug in the arterial wall which compensates for the increased flow disturbance score J_{FDI} (at a $w_{\text{FDI}} = 0.5$) resulting from the high n . Consequently, the total score of the strut design with the higher shape exponent (Fig. 4.8 B) is slightly better than that of the low n design (Fig. 4.8 C).

Similarly to the procedure described above to estimate the global trends of the cost function for the semi-strut height a_s and width b_s , we have investigated the trend for the strut shape exponent n . The three strut designs presented in Fig. 4.8 are a representative sample of the results used to deduce the estimated global trend of the cost function of a P-DES (configuration E2) optimization for the strut shape exponent n . The results indicate that for otherwise identical strut geometry parameters, a larger n decreases the inefficacy score \bar{I}_m and increases J_{FDI} .

Contrary to strut height, the strut shape exponent n drives the drug-related inefficacy score \bar{I}_m and the flow disturbance score J_{FDI} in opposite directions. For the case of $w_{\text{FDI}} = 0.5$ considered thus far, the effect of n on \bar{I}_m outweighs its effect on J_{FDI} for most of the design range until a balance is reached between the two, which determines the optimal shape exponent n .

The flat and elongated strut with a high shape exponent n of the optimal strut design (Fig. 4.8 A) is the result of all three estimated global trends. The small height leads to a low inefficacy score \bar{I}_m and J_{FDI} . Although the wide strut and the high shape exponent n increase the flow disturbance score J_{FDI} , this increase is overwhelmed by the additional reduction in the inefficacy score \bar{I}_m at high n .

Optimization case 2: The results shown above were for a low-dose P-DES in configuration E2 where the endothelium is denuded within the stented portion of the vessel and also upstream and downstream of the stent but intact otherwise (case 1 in Table 4.2). We now consider a low-dose P-DES in configuration E1 where the endothelium is assumed to be denuded only within the stented portion of the vessel (case 2 in Table 4.2). Fig. 4.9 A shows the final optimal result of the strut design optimization in this case. The optimal strut design has a large strut shape exponent of $n = 5$ and is almost 3 times wider than high ($a_s = 27.6 \mu\text{m}$ and $b_s = 75.9 \mu\text{m}$). The sub-optimal strut design shown in Fig. 4.9 B has an almost identical semi-strut width b_s (difference of 2%) and a 17% smaller semi-strut height a_s with a basically identical strut shape

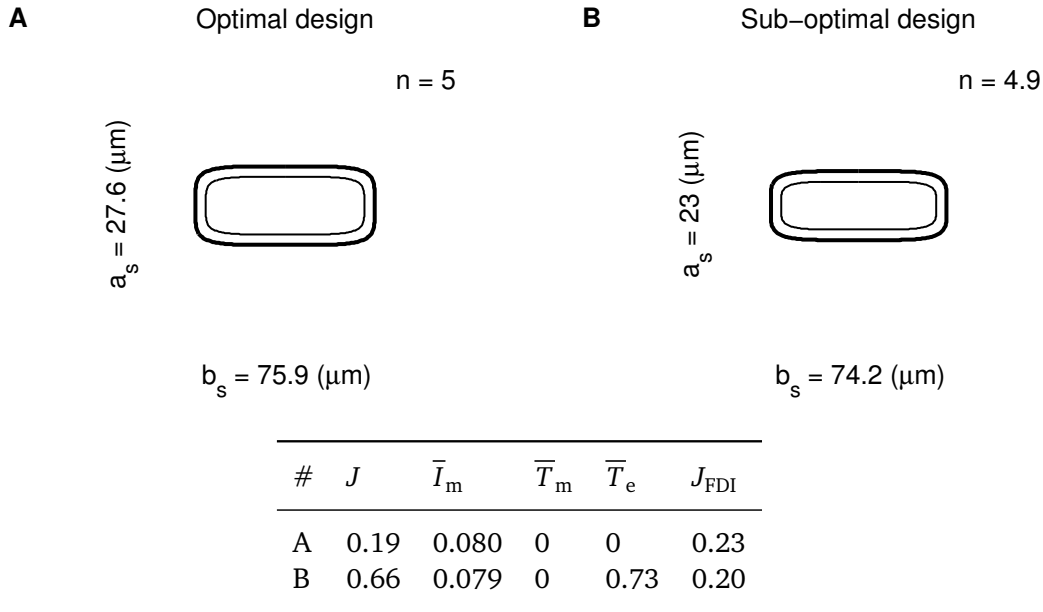


Figure 4.9: Optimization case 2: optimal P-DES strut design compared to sub-optimal strut design with smaller a_s for $w_{\text{FDI}} = 0.5$ and configuration E1. **A**: Optimal strut design, **B**: strut design for smaller a_s . The table provides the total score J and the contributing scores \bar{I}_m , \bar{T}_m , \bar{T}_e , and J_{FDI} for each strut design.

exponent n compared to the optimal strut design.

The table in Fig. 4.9 shows that the two scores that are responsible for the total score $J = 0.19$ of the optimal design are the inefficacy score $\bar{I}_m = 0.08$ and the flow disturbance score $J_{\text{FDI}} = 0.23$. Both toxicity scores are zero. The cost function score of the sub-optimal strut design is increased by 240% ($J = 0.66$), almost entirely due to the appearance of endothelial toxicity measured by $\bar{T}_e = 0.73$. These results suggest that a minimal change in the strut height has a significant effect on the toxicity performance of the strut design and may point to limitations in the robustness of our modeling.

The increase in the endothelial toxicity when endothelium is present immediately upstream and downstream of the stent stems from the altered convective field within the arterial wall which leads to drug transport from the struts towards the luminal surface. The added endothelial toxicity in the presence of endothelium represents the only difference between the optimization with and without endothelium for P-DES. Otherwise, the same three global trends are observed: 1) thinner struts lead to decreased inefficacy and flow disturbance scores \bar{I}_m and J_{FDI} ; 2) wider struts improve the inefficacy score \bar{I}_m ; and 3) larger n decreases the inefficacy score \bar{I}_m and increases J_{FDI} .

Optimization case 3: Figure 4.10 depicts the optimal low-dose P-DES strut design that results from an optimization with a FDI weight factor of $w_{\text{FDI}} = 10$ and in configuration E1 (case 3 in Table 4.2). In this case, the optimal strut shape is ellipsoidal with $n = 2.1$ and an aspect ratio $b/a \approx 2$ with a small semi-strut width of $b_s = 24.5 \mu\text{m}$. The inefficacy score is $\bar{I}_m = 0.31$ and the endothelial toxicity score is $\bar{T}_e = 1.1$. Compared to the optimal strut design obtained for a FDI weight factor $w_{\text{FDI}} = 0.5$ (Figs. 4.9 A), these values are very high, in particular the endothelial toxicity \bar{T}_e which was zero in the previous case. For the present optimum with $w_{\text{FDI}} = 10$, the high values of \bar{I}_m and \bar{T}_e are balanced by lowering J_{FDI} to 0.1. The optimal strut design for $w_{\text{FDI}} = 0.5$ had $J_{\text{FDI}} = 0.23$ (see Fig. 4.9 A).

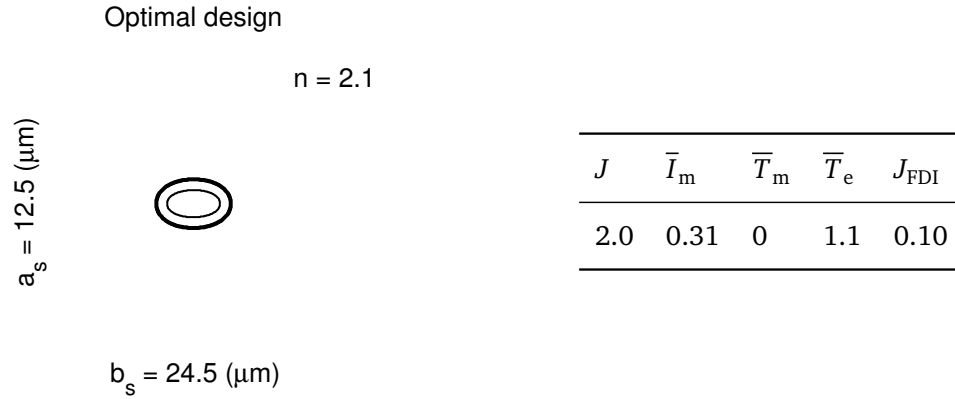


Figure 4.10: Optimization case 3: optimal P-DES strut design for $w_{\text{FDI}} = 10$ and configuration E1. The table provides the total score J and the contributing scores \bar{I}_m , \bar{T}_m , \bar{T}_e , and J_{FDI} .

Stent strut design optimization of sirolimus-eluting stents

Optimization case 4: Fig. 4.11 depicts the change in the inefficacy score \bar{I}_m (black) and the flow disturbance score J_{FDI} (white) for increasing semi-strut height a_s (Fig. 4.11 A) and semi-strut width b_s (Fig. 4.11 B) for a high-dose S-DES and configuration E2 (case 4 in Table 4.2). Fig. 4.11 A demonstrates how increasing the semi-strut height a_s from $25 \mu\text{m}$ to $72 \mu\text{m}$ with the other design variables held constant in a narrow band (semi-strut width ($b_s = 39 \pm 3.2 \mu\text{m}$) and shape exponent $n = 2.2 \pm 0.17$) decreases the inefficacy score \bar{I}_m by 32%. Over the same range, the flow disturbance score J_{FDI} increases by 146%. This behavior is observed for other pairs of b_s and n throughout the design space (data not shown).

Fig. 4.11 B shows that \bar{I}_m and J_{FDI} both decrease moderately (by approximately 20%) when the semi-strut width b_s varies from $b_s = 27 \mu\text{m}$ to $b_s = 82 \mu\text{m}$. In Fig. 4.11 B n was fixed at approximately 2.2 and a_s at $50 \pm 18 \mu\text{m}$. A decrease in the inefficacy score \bar{I}_m for increasing b_s

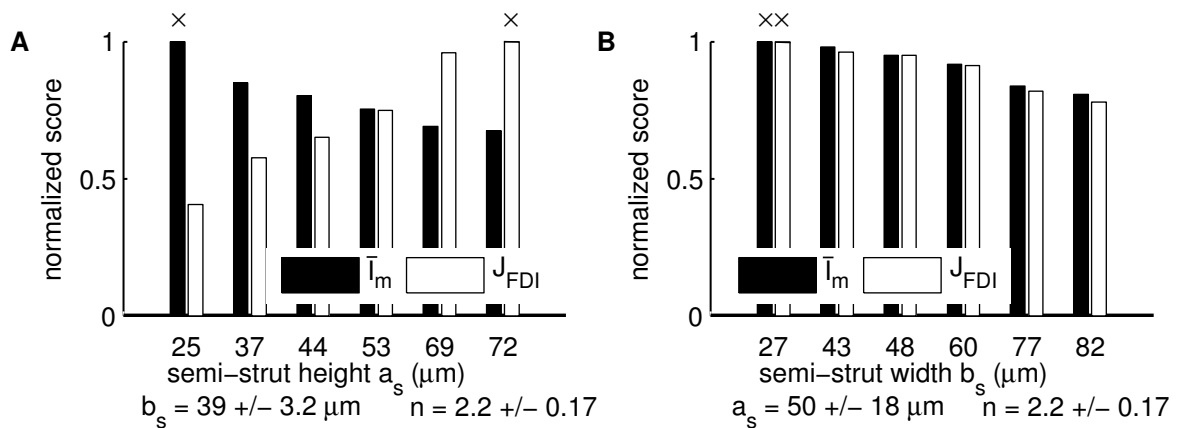


Figure 4.11: Optimization case 4: estimated global trends of the cost function of the high-dose S-DES (configuration E2) strut design optimization for a variation of semi-strut height a_s and semi-strut width b_s . Change in the inefficacy score \bar{I}_m (white bars) and flow disturbance score J_{FDI} (black bars) for increasing **A:** semi-strut height a_s and **B:** semi-strut width b_s . The scores are normalized by the maximum score among the presented designs which is marked by a \times .

is observed for all other combinations of a_s and n (data not shown). This is not the case for J_{FDI} where the variation with b_s depends on the values of a_s and n (data not shown).

Thus, two global trends for high-dose S-DES strut design optimization in configuration E2 are: 1) thinner struts (smaller a_s) lead to increased inefficacy scores \bar{I}_m and to lower flow disturbance scores J_{FDI} and 2) wider struts (larger b_s) weakly improve (reduce) the inefficacy score \bar{I}_m .

The effects of a_s on the drug-related objectives outweigh its effect on the flow-related objective when $w_{\text{FDI}} = 0.5$ for most of the design range until a balance is reached between the two objectives, which determines the optimal semi-strut height a_s . Interestingly, the effect of a_s on the drug-related objective for a S-DES is opposite to that seen previously for P-DES.

The optimal strut design of a high-dose S-DES in configuration E2 where the endothelium is denuded within the stented portion of the vessel and also upstream and downstream of the stent (case 4 in Table 4.2) is depicted in Fig. 4.12 A. The optimal strut design has equal semi-strut height a_s and semi-strut width b_s of approximately $72 \mu\text{m}$ and a small strut shape exponent of $n = 1.6$. The sub-optimal strut design (Fig. 4.12 B) has equal semi-strut height and width $a_s = b_s = 75 \mu\text{m}$ and a strut shape exponent of $n = 1.9$. The second sub-optimal strut design (Fig. 4.12 C) has a semi-strut height $a_s = 74 \mu\text{m}$, a semi-strut width $b_s = 72 \mu\text{m}$, and a strut shape exponent of $n = 5.9$. The shapes of these two struts correspond to typical DES strut shapes, their strut sizes are comparable to first generation DES.

The table in Fig. 4.12 shows that the two scores contributing to the total cost function score of $J = 0.30$ of the optimal strut design are the inefficacy score $\bar{I}_m = 0.14$ and the flow disturbance score $J_{\text{FDI}} = 0.33$. Holding strut dimensions approximately constant, we can observe how slightly increasing the strut shape exponent n to form a more circular strut shape only marginally increases (by 4%) the total cost function score J . This increase is due to an increase of J_{FDI} . If we increase the exponent further to $n = 5.9$, the total score J of the strut

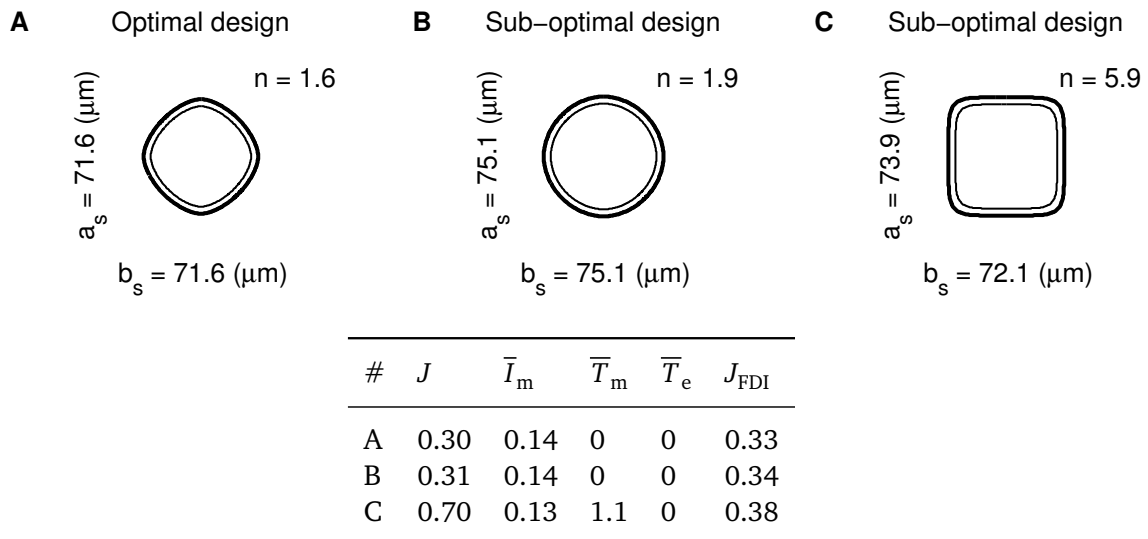


Figure 4.12: Optimization case 4: optimal high-dose S-DES strut design compared to sub-optimal strut designs similar to commercial strut designs for $w_{\text{FDI}} = 0.5$ and configuration E2. **A**: Optimal strut design, **B**: strut design for high n , **C**: strut design for low n . The table provides the total score J and the contributing scores \bar{I}_m , \bar{T}_m , \bar{T}_e , and J_{FDI} for each strut design.

design increases dramatically by 130% which can almost entirely be attributed to an increase in the medial toxicity \bar{T}_m . Generally speaking, for an otherwise identical strut design of a high-dose S-DES in configuration E2, a smaller shape exponent n decreases both the toxicity score \bar{T}_m and the flow disturbance score J_{FDI} without significantly affecting the inefficacy score \bar{I}_m .

Optimization case 5: Figure 4.13 illustrates the optimal strut design for a high-dose S-DES with endothelium denuded only in the stented region, i.e. configuration E1 (case 5 in Table 4.2). The optimal strut has an aspect ratio $b/a = 1.2$ and a semi-strut width of $b_s = 47.5 \mu\text{m}$. The strut shape exponent is at the lowest limit of the design range we allowed (hard constraint of the design range) with $n = 1.5$. The table in Fig. 4.13 shows that this strut design yields a low inefficacy score of $\bar{I}_m = 0.12$ with a minimal medial toxicity score of $\bar{T}_m = 0.02$ and a $J_{\text{FDI}} = 0.2$.

Comparison of this optimal strut design with the optimal strut design for a similar stent but with endothelial configuration E2 (Fig. 4.12 A) reveals that the strut shape is not significantly altered, i.e. the shape exponent n is very similar in both cases. The aspect ratio, however, of the optimal strut design for the E1 configuration is about 20% higher and the semi-strut width b_s is reduced by 33% compared to the optimal strut design for the E2 configuration. Due to the reduced transport in the arterial wall, which results from the shielding function of the endothelium upstream and downstream of the stent, a smaller strut size in the E1 configuration (a_s and b_s , Fig. 4.13) achieves a similar inefficacy score \bar{I}_m to that in the E2 configuration.

Optimization case 6: The S-DES simulations considered so far focused on high-dose S-DES; therefore, the binding sites in the arterial wall were predominantly occupied. Given the wide therapeutic window of sirolimus, we were also interested in investigating how the optimal strut design needs to be adjusted to be suitable for S-DES with a low initial concentration loaded onto the polymer coating. In this case, the effective and toxic concentration thresholds of the cost function are reduced to the values of the therapeutic window of paclitaxel.

Fig. 4.14 shows the optimal strut design for a low-dose S-DES with an E1 configuration (case 6 in Table 4.2). The optimization results in a highly elongated and rectangular strut with a semi-strut width of $b_s = 126 \mu\text{m}$, a semi-strut height of $a_s = 37 \mu\text{m}$ and a strut shape exponent of $n = 4.8$. This design achieves an extremely low inefficacy score of $\bar{I}_m = 0.067$ and a flow

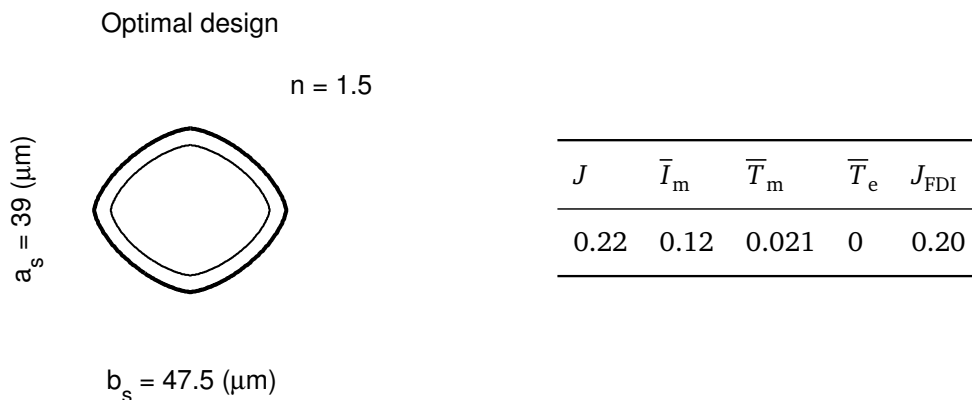


Figure 4.13: Optimization case 5: optimal high-dose S-DES strut design for $w_{\text{FDI}} = 0.5$ and configuration E1. The table provides the total score of the cost function J and its contributing scores \bar{I}_m , \bar{T}_m , \bar{T}_e , and J_{FDI} .

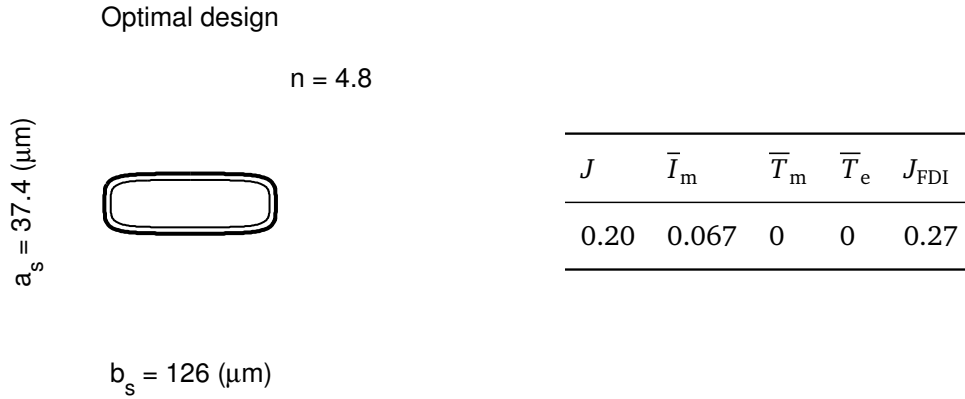


Figure 4.14: Optimization case 6: optimal low-dose S-DES strut design for $w_{\text{FDI}} = 0.5$ and configuration E1. The table provides the total cost function score J and its contributing scores \bar{I}_m , \bar{T}_m , \bar{T}_e , and J_{FDI} .

disturbance score of $J_{\text{FDI}} = 0.27$, adding up to a total cost function value of $J = 0.2$. This strut design has an even larger semi-strut width b_s than the optimal P-DES (Fig. 4.9 A) but has otherwise similar strut design variables (a_s and n).

Group 2: Optimization of two-layered polymer coatings

The second group of optimization runs aims to determine optimal properties of two-layered polymer coatings for both P-DES and S-DES. The four most significant design variables for a DES with a top-coat (as revealed by the sensitivity estimation study) are the initial drug concentration c_0 , the effective drug diffusion coefficient in the polymer coating D_c , the thickness of the polymer coating L_c , and the permeability of the top-coat P_c that encases the first polymeric layer. These parameters define the key properties of the stent polymer coating and are thus the design variables of the optimization problem. The thicker polymer coating layer encasing the stent strut contains either of the two drugs paclitaxel or sirolimus, while the thin top-coat encasing the thick polymer coating is assumed to be initially devoid of drug. We investigated the differences of an optimal coating design for the two different drugs paclitaxel and sirolimus with stents having circular struts of radius $50 \mu\text{m}$ and for the case of configuration E1 where the endothelium is denuded only in the stented zone. The specifications for the two optimization runs are summarized in Table 4.3.

The results of the two optimization runs are depicted in Fig. 4.15. The optimal polymer

Table 4.3: Group 2 optimization runs: two-layered polymer coating optimization

| Figure ^a | Drug | c_{eff} | c_{tox} | Config. ^b | w_{FDI} ^c |
|---------------------|------------|-------------------|-------------------|----------------------|-------------------------------|
| 4.15 A | Paclitaxel | $1 \cdot 10^{-5}$ | $1 \cdot 10^{-2}$ | E1 | 0.5 |
| 4.15 B | Sirolimus | 0.29 | 0.73 | E1 | 0.5 |

^a figure depicting optimal polymer coating properties

^b model configuration of the endothelium as depicted in Fig. 3.1

^c FDI weight factor

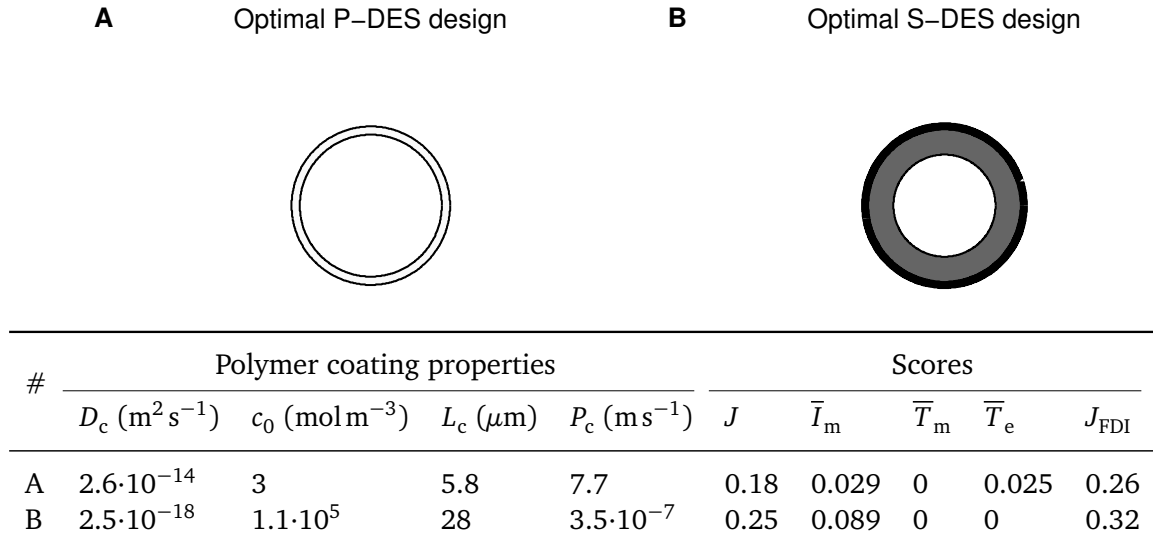


Figure 4.15: Optimal two-layered polymer coating properties for $w_{\text{FDI}} = 0.5$ and configuration E1. **A:** P-DES, **B:** S-DES. The table provides the optimal polymer coating properties comprised of effective drug diffusivity D_c , initial drug concentration c_0 , polymer thickness L_c , and top-coat permeability P_c as well as the associated total cost function score J and its contributing scores \bar{I}_m , \bar{T}_m , \bar{T}_e , and J_{FDI} . Visualization of the parameters c_0 , L_c and P_c is achieved as follows: the magnitude of c_0 is depicted using grey levels with white indicating a very low concentration and dark grey a very high concentration; the coating thickness is drawn on top of the circular strut (relative to the strut radius of $50 \mu\text{m}$); the permeability of the top-coat P_c is visualized by the thickness of the outer contour of the strut geometry with a thin line indicating a high permeability and a thick line representing a low permeability.

coating of a P-DES (Fig. 4.15 A) has a thickness of $L_c = 5.8 \mu\text{m}$ and is initially loaded with paclitaxel at a concentration of only $c_0 = 3 \text{ mol m}^{-3}$. Optimal drug release from the polymer coating occurs with an effective diffusivity $D_c = 2.6 \cdot 10^{-14} \text{ m}^2 \text{ s}^{-1}$, and the top-coat has a high permeability of $P_c = 7.7 \text{ m s}^{-1}$. A P-DES with these coating properties exhibits an inefficacy score of $\bar{I}_m = 0.03$, a low endothelial toxicity score of $\bar{T}_e = 0.025$, and a flow disturbance score of $J_{\text{FDI}} = 0.26$, yielding an overall cost function value of $J = 0.18$.

In contrast, an optimal S-DES polymer coating (Fig. 4.15 B) has very different properties. More specifically, the optimal coating thickness is $L_c = 28 \mu\text{m}$ that is initially loaded with a sirolimus concentration of $c_0 = 1.1 \cdot 10^5 \text{ mol m}^{-3}$. Optimal drug release requires an effective drug diffusivity of $D_c = 2.5 \cdot 10^{-18} \text{ m}^2 \text{ s}^{-1}$, and the top-coat needs to have a low permeability of $P_c = 3.5 \cdot 10^{-7} \text{ m s}^{-1}$. This combination of polymer coating properties leads to an inefficacy score of $\bar{I}_m = 0.09$, a zero medial toxicity score \bar{T}_m , and a flow disturbance score of $J_{\text{FDI}} = 0.32$, yielding a total cost function value of $J = 0.25$.

4.4 Discussion

The derivative-free optimization framework we have developed in this chapter has been applied for the identification of unique optimal strut designs for paclitaxel- and sirolimus-eluting stents with zero-order release kinetics. The optimal P-DES strut (Fig. 4.8 A) is very thin and elongated and has a cross-section that is rather rectangular. The general design features of the optimal

low-dose S-DES (Fig. 4.14) are comparable to the P-DES design. The optimal high-dose S-DES stent strut design (Fig. 4.12 A), however, is very different from the two previous strut designs. The strut is almost diamond-shaped with equal length and height.

4.4.1 Optimal DES strut designs are tailored to optimized transport dynamics in the arterial wall

With the exception of the semi-strut width b_s , we can explain the optimal values of the design variables of P-DES and high-dose S-DES strut designs based on the global trends of the contributing scores of the cost function (Table 4.4). For P-DES (Fig. 4.8 A), the optimal semi-strut height a_s is at the low end of the design range and the strut shape exponent n at the high end of the design range. For high-dose S-DES (Fig. 4.12 A), the value of the optimal semi-strut height a_s is at the upper end of the design range and the strut shape exponent n at the low end. When the drug-related and flow-related objectives have opposing trends with respect to a change in the design variable (e.g. semi-strut height a_s for high-dose S-DES), the optimal value is derived from the balance between the contributing scores which depends on the choice of the flow disturbance weight factor w_{FDI} . When the drug-related and flow-related objectives follow the same trend with a change in the design variable (e.g. semi-strut height a_s for P-DES), the optimal value of the design variable is expectedly at the extreme of the permitted design range. In that case, the gradient of the cost function J with respect to the design variable x_i has the same sign over the entire design space. Consequently, the optimum of the cost function J is located on one of the borders of the design space.

Changing the semi-strut width b_s has a weak effect on J_{FDI} due to the very low sensitivity of J_{FDI} to b_s (Fig. 4.5). The small optimal b_s seen with the P-DES optimization with $w_{\text{FDI}} = 10$ indicates that J_{FDI} increases with increasing b_s . This positive gradient of J_{FDI} with respect to b_s is indicated in Table 4.4 with a + sign. The weak dependence of J_{FDI} on a change in b_s for both P-DES and high-dose S-DES explains the large semi-strut width b_s of the optimal strut designs. Since the optimal semi-strut height a_s of P-DES is very small, the optimal semi-strut width b_s can be very large, even outside of the typical design range, without excessively increasing J_{FDI} . The optimal semi-strut height a_s of high-dose S-DES is larger than that of optimal P-DES; thus, the optimal semi-strut width b_s needs to be smaller in order to reduce J_{FDI} , but b_s in that case remains near the upper end of the typical design range.

Two key elements are necessary to understand the difference in the global trends of the cost function between P-DES and high-dose S-DES strut design optimizations (and thus to understand why the strut designs of P-DES (Fig. 4.8 A) and low-dose S-DES (Fig. 4.14) are so similar). First, in the cases considered, the drug is assumed to be released from the stent over a time period that is significantly longer than any of the time scales governing the processes involved in drug transport (convection, diffusion, binding and unbinding). For this slow release, the concentration in the polymer coating remains nearly constant (equal to the initial value c_0) during the period of four weeks considered in our simulations, and this concentration sets the drug concentration level in the arterial wall. After an initial transient phase, a quasi-steady state of drug transport in the arterial wall is attained (see Chapter 3). The process dominating drug transport in the transient phase and in the subsequent quasi-steady regime depends on the occupancy of drug binding sites in the media [179] (see also Chapter 2).

The transport processes of convection and diffusion only govern free (mobile), unbound drug concentration in the arterial wall. This can be seen, for example, in Equation (A.9) in Appendix A which was derived under the simplifying condition of constant equilibrium

Table 4.4: Summary of estimated global trends of the cost function of paclitaxel- and high-dose sirolimus eluting stent strut design optimizations with a FDI weight $w_{\text{FDI}} = 0.5$. The upper row corresponds to P-DES and the lower row to S-DES.

| x_i | J | \bar{I}_m | \bar{T}_m | J_{FDI} |
|-------|-----|-------------|-------------|------------------|
| a_s | + | + | 0 | + |
| | +/- | - | 0 | + |
| b_s | +/- | - | 0 | + |
| | +/- | - | 0 | + |
| n | +/- | - | 0 | + |
| | + | 0 | + | + |

+: the contributing score (\bar{I}_m , \bar{T}_m or J_{FDI}) or the cost function J (assuming $w_{\text{FDI}} = 0.5$) increases with increasing design variable x_i (i.e. the estimated gradient of the score with respect to a change of the design variable is *positive* in the estimation of global trends)

0: the contributing score (\bar{I}_m , \bar{T}_m or J_{FDI}) or the cost function J (assuming $w_{\text{FDI}} = 0.5$) does not change significantly with increasing design variable x_i (i.e. the estimated gradient of the score with respect to a change of the design variable is *negligible* in the estimation of global trends)

-: the contributing score (\bar{I}_m , \bar{T}_m or J_{FDI}) or the cost function J (assuming $w_{\text{FDI}} = 0.5$) decreases with increasing design variable x_i (i.e. the estimated gradient of the score with respect to a change of the design variable is *negative* in the estimation of global trends)

+/-: the behavior of the cost function J (assuming $w_{\text{FDI}} = 0.5$) depends on the range of the design variable x_i . The optimal design variable x_i corresponds to the value at which the variation of \bar{I}_m (with respect to x_i) balances the variation of J_{FDI} (with respect to x_i).

between the bound drug concentration b and the free drug concentration c , a situation that arises if the time scales of drug binding and unbinding are very fast compared to the time scales of convection and diffusion. The concentration equilibrium between the two drug states is expressed by the total binding coefficient κ . The inverse of κ only multiplies the convective and diffusive term of Eq. (A.9), so if κ is large, then drug transport is reduced while if $\kappa \approx 1$, then transport (of the free drug) is unhindered. In the present case, this κ depends on the free concentration: if the binding sites are saturated, then any drug concentration exceeding the maximum binding site density in the arterial wall is governed by convection and diffusion and κ would be small, and convection and diffusion become the two dominant processes of drug transport. If, on the other hand, the binding sites are not saturated, then κ would be large, and the fast binding process becomes the dominant drug transport process and significantly (by an order of magnitude) slows down convection and diffusion.

Consequently, the optimum high-dose S-DES, for which the cost function dictates concentrations of the order of the binding site density and beyond, is in the convection- and diffusion-dominated regime. Conversely, the optimum P-DES and the low-dose S-DES, for which the cost function dictates concentrations that are at least an order of magnitude lower than the drug binding site density (see Chapter 2), is in the binding-dominated regime with reduced convection and diffusion.

The second key element to understand in considering differences between P-DES and high-dose S-DES strut design optimization is that optimal strut design is determined by the balance of scores that contribute to the overall cost function. In most of the simulations, the only scores relevant to the optimization are the inefficacy score \bar{I}_m and the flow disturbance score J_{FDI} . The one exception is the case of high-dose S-DES with configuration E1 (Fig. 4.13) where the medial toxicity score \bar{T}_m remains in the formulation; however, this score typically is an order of magnitude lower than \bar{I}_m and J_{FDI} and thus has a limited effect on the optimization results.

The two optimal designs, the elongated rectangular strut (Figs. 4.8 A, 4.9 A and 4.14) and the diamond-shaped strut (Figs. 4.12 A and 4.13), identified by the optimization algorithm constitute a compromise between a fluid mechanically streamlined design and an efficient design from the perspective of optimized drug transport in the arterial wall. In this regard, we identify two regimes:

- *Binding-dominated regime:* When the binding sites are not saturated, convection and diffusion are significantly slowed down by the binding and unbinding dynamics. The only effective solution to rapidly achieve maximum efficacy in the arterial wall during the transient phase is to maximize the width of the strut, which in turn requires minimizing the strut height to obtain a streamlined design. The lower bound of this minimization is, in our case, either given by our choice of the design range or the occurrence of endothelial toxicity. In the case where endothelium is present immediately upstream and downstream of the stent (configuration E1), this endothelial toxicity occurs as a result of the convection field around the first and last struts. However, even if the endothelium is denuded upstream and downstream of the stent (configuration E2), endothelial toxicity would increase dramatically if the strut height were so small that the strut would sit in the subendothelial space and thus elute massively into this layer.
- *Convection- and diffusion-dominated regime:* When the binding sites are saturated, convection and diffusion are not slowed down, and a small strut size is sufficient to rapidly achieve high drug efficacy. The diamond strut shape enhances convection around the stent struts relative to a more rectangular strut thereby reducing concentration peaks close to the stent struts which would otherwise risk to become toxic. A flat strut design (high shape exponent n or a large aspect ratio b_s/a_s) similar to the one obtained for the binding dominated regime risks toxic concentrations in zones close to the strut where convection is small (shielding effect). The optimal S-DES strut with configuration E1 (Fig. 4.13), thus, has a slightly higher aspect ratio compared to the optimal strut with configuration E2 (Fig. 4.12 A) in order to direct convection from the central stent region to the zones where convection is shielded by the endothelium.

4.4.2 Optimal two-layered DES polymer coatings are tailored to the eluted drug

The optimization of the drug delivery strategy for single-layered P-DES and S-DES coatings, described in Chapter 3, revealed an essential difference between optimal release kinetics of P-DES and S-DES. The high retention capabilities of paclitaxel in the media, resulting from the significantly slower unbinding kinetics (see Chapter 2), enable an optimal strategy where all drug stored in the polymer coating is quickly released into the arterial wall and then the drug dynamics ensure a satisfactory concentration distribution within the therapeutic window for the remainder of the intended period of therapy (typically several weeks). Even though exposure of the arterial wall to adverse concentrations (toxic concentrations in the media and

unacceptably high concentrations at the endothelium) cannot be prevented with this strategy, the exposure times are very short. This strategy is impossible to achieve with sirolimus because of the significantly shorter retention time of sirolimus in the arterial wall resulting from the faster unbinding time scale. Thus, only very slow release kinetics at relatively high initial concentrations c_0 can assure sufficient concentration levels throughout the period of the therapy.

The results presented in this chapter for optimal two-layered polymer coatings are in line with and complement the results described above. For P-DES releasing a low initial drug load quickly, a setup unhindered by a top-coat is the best solution (Fig. 4.15 A). Also, only a relatively small amount of drug is necessary to achieve the efficacy goals of the cost function, and the consequently low resulting coating thickness further serves to reduce flow disturbance. This optimal design is consistent with recent trends towards thinner coatings on P-DES [60].

The optimal design of S-DES polymer coatings (Fig. 4.15 B) is opposite to that of P-DES. High drug loads in this case need to be stored in a thick coating and released at a very slow rate that is additionally controlled by a top-coat with low permeability. Addition of a top-coat to extend drug release time is a common feature in the design of S-DES in order to extend their efficacy in inhibiting smooth muscle cell proliferation [3, 90]. It also appears to be beneficial for stent re-endothelialization [57].

4.4.3 Challenges of the FDI weight factor

Although we have chosen a FDI weight factor that heavily favors the drug-related objectives of the cost function ($w_{\text{FDI}} = 0.5$) in the majority of the simulations considered in this chapter, we were able to identify optimal strut shapes that depended on fluid dynamic considerations. The highly elongated shapes of the optimal designs we obtained for P-DES and low-dose S-DES are probably extreme cases that are very difficult to implement in clinical practice due to considerable challenges associated with the delivery via a balloon of a stent with struts that have such high aspect ratios.

Taking the approach of optimizing the drug delivery strategy by focusing on the drug-related goals and only then optimizing strut geometry to achieve the fluid dynamic objectives may not necessarily be the most effective way to address this issue. In the one simulation in which we chose $w_{\text{FDI}} = 10$ we managed to obtain a fluid dynamically-shaped strut, but reducing J_{FDI} by about $1/3$ came at the cost of almost tripling the inefficacy score (see Figs. 4.8 and 4.10). Future experimental studies will be essential for defining the relative importance of drug- and flow-related contributions to the cost function and hence for the most appropriate value of the flow disturbance weight factor w_{FDI} .

Another direction that merits future exploration is the optimization of DES that have different shapes on their luminal and abluminal sides. The fluid dynamic objective would be emphasized in the optimization of the luminal side of the stent strut, while the drug-related objectives would be most important in the optimization of the abluminal side of the stent geometry. It is recognized, of course, that stent struts that have different luminal and abluminal shapes might pose an additional manufacturing challenge. In the current study, the stent struts were considered to be symmetric about both their major and minor axes; however, this constraint can be readily relaxed by making the parameter m_s (which controls the number of symmetry axes of the shape) in the Superformula (Eq. (4.1)) an additional design variable.

Finally, we need to emphasize that the current study did not take into account the mechanical stresses that a stent needs to withstand to open an obstructed artery or the stresses induced by the stent in the arterial wall. While the lowest values set for the design range of

the semi-strut height and width were inspired by the lowest profile stent designs found in the literature [164], the optimal results of the low-dose DES confirmed that these constraints do not ensure reasonable designs from a solid mechanical point of view. It might thus be advisable to extend the computational model via constitutive laws that describe the structural mechanics of the stent and the biomechanics of the arterial wall and add adequate scores to the cost function. However, as the number of objectives increases, an aggregate cost function approach becomes less meaningful since it is very dependent on the choice of weighting factors among the different objectives. Seeking pareto optimal solutions, which are the optimal designs for which a change in any of the design variables decreases the score of one objective only at the expense of another, might constitute a promising future approach in DES design optimization [56, 141, 153].

Conclusions

In the introductory chapter to this dissertation we raised four questions for which we can now propose some answers with the material presented in the three chapters.

What is an optimal stent? An optimal stent re-establishes blood flow in a previously obstructed artery and assures this state permanently. Assuming that the implantation of a stent has successfully re-opened the target vessel, the two major events that can potentially re-occlude the blood vessel are in-stent restenosis and stent thrombosis. Prevention of these two complications may be accomplished, on the one hand, by controlling proliferation and migration of smooth muscle cells (SMCs) and, on the other hand, by assuring a fast recovery of the endothelium. We formulated our objective for ideal drug-eluting stents (DES) on this premise:

1. An ideal delivery of the anti-proliferative drug from the DES polymer coating leads a) to therapeutic levels of drug concentration in the arterial media, limiting SMC proliferation during the process of re-endothelialization and b) to minimal drug concentration at the endothelial surface.
2. An ideal geometric design of the DES minimally disturbs the arterial flow field.

The strategy we developed to identify DES designs which comply with these two requirements used a physiologically based computational model (Chapter 2) coupled to an efficient derivative-free optimization method via our cost function (Chapters 3 and 4). This strategy proved successful in determining robust optimal DES design ranges (small changes in any of the design variables did not yield a large change in performance) in a computationally efficient manner.

What design elements are crucial for obtaining an optimal stent? The screening study performed in Chapter 4 showed that the most crucial design variables are the drug diffusion coefficient in the stent polymer coating D_c and the initial concentration of drug loaded in the polymer c_0 , which determine the drug delivery strategy of the DES design. Next in importance are the permeability of an optional top-coat encasing the polymeric coating on the DES P_c and the thickness of the polymer coating L_c . Together they determine how the drug will be eluted from the DES. Based on our cost function, the drug delivery strategy is the most crucial design element of DES, while geometric variables of the strut shape are secondary to optimal designs and can be used to refine the performance of DES.

What should these design elements be like for an optimal stent? What is the role of the drug choice? As we showed, these two questions are strongly coupled. Optimal designs depend on the drug kinetics in the arterial wall, which in turn depend on the drug delivery from the DES polymer coating. On the one hand, the therapeutic window of the drug sets the order of magnitude of the drug concentration that should be loaded onto the stent initially. The specific drug kinetics determine the rate at which the drug should be released. On the other hand, the initial drug concentration and the release rate determine the prevalent drug transport phenomena: if the drug delivery strategy results in the drug binding sites in the arterial wall being predominantly occupied, then convection and diffusion dominate. Otherwise, binding and unbinding dominate.

For optimal performance, the strut shape should be tuned to the dominant transport process. If convection and diffusion are dominant, then a small strut still yields sufficient drug efficacy throughout the arterial media, and the strut shape is adjusted to yield isotropic drug transport. If drug binding and unbinding are dominant, only very wide struts can assure efficacious drug concentrations reaching the inter-strut domains of the media, while the strut height should be minimal to obtain a more fluid-dynamically streamlined strut.

The narrow therapeutic window of paclitaxel requires very low drug concentrations in the polymer coating, thus yielding a low-dose design. These optimal drug concentrations are orders of magnitude lower than typical concentrations found on today's DES. The long retention of paclitaxel in the media enables two types of efficient DES designs, with either fast (hours) or slow (months) release of the drug. Sirolimus has a wide therapeutic window. Consequently, we found low-dose and high-dose optimal stent designs. The short retention of sirolimus in the media, however, requires a very slow release of the drug (years).

The strong coupling between physiological transport in the arterial wall and DES design demands versatile computational models that simultaneously consider all contributing drug transport phenomena that dominate at each relevant time scale. However, accurate modeling of the binding and unbinding process significantly increases computational cost. This coupling makes the model sensitive to the non-dimensional quantities that define the ratio between transport processes. Specifically, the parameter values of the model need to be sufficiently accurate to recover the dominant transport processes in the physiological situation. The relevant non-dimensional quantities are the two Damköhler numbers, which compare binding to convection and binding to diffusion, respectively. As discussed in Chapter 2, a time-dependent, spatially averaged Damköhler number (rather than a constant value) is required to accurately describe the varying importance of binding during the period of drug elution.

5.1 Future work

In the course of this dissertation a versatile framework for DES optimization was developed. Application of this framework to idealized configurations of arteries stented with a DES yielded some general guidelines for future DES design, especially concerning strategies for the effective elution of the anti-proliferative drug from the stent. Despite these very useful results, many improvements can be envisaged in future models. Limitations of the current model are that the model geometry is 2D axisymmetric, the considered stent is idealized as a series of rings, and the model is limited to a straight vessel segment. It will be important to eventually perform the simulations on more realistic three-dimensional geometries where the detailed structure of the stent design is taken into account. Such simulations, however, are expected to be much

more expensive computationally and will thus require additional computing resources. Even in the current context of two-dimensional simulations, the following three specific considerations should be taken into account in future modeling efforts:

- *additional physiological considerations*: exploring model setups where the arterial wall is in a diseased state or the stent is malapposed or poorly configured,
- *expanding the cost function*: adding other considerations to the cost function to account for additional phenomena relevant for DES design (for example in-stent thrombosis),
- *improved representation of the arterial wall*: more accurate modeling of the structure of the arterial wall paving the way for lesion-specific optimization.

The first of these pathways is a direct extension of this work that requires only minor modifications to the current computational model, while the other two directions are more challenging.

5.1.1 Additional physiological considerations

The parameter choice for the computational model as implemented throughout this dissertation assumes a healthy arterial wall, i.e. the subendothelial space (SES) has a normal physiological thickness and is free of SMCs [47, 59]. Arteries that require stenting are, of course, diseased such that SMCs, foam cells, and other constituents of plaques are present in the SES. Atherosclerotic arteries also exhibit a thickened intima with an occasionally damaged internal elastic lamina (IEL). It is of interest to investigate how these various conditions affect the outcome of the optimization. Conditions that reflect aspects of a diseased arterial wall can be readily taken into account in the current computational model in several ways. For instance, drug reaction as used in the media can be added to the SES to model the presence of SMCs in the SES (maybe with a reduced maximum binding capacity b_{\max} to account for a lower density of SMCs than in the media). Because inclusion of drug reaction in the SES is expected to lead to higher drug concentrations in the vicinity of the endothelium, design strategies focusing on abluminal drug release merit further investigation. To investigate the effect of intimal thickness on the optimization results, the parameter controlling the SES thickness L_{SES} can be increased. Finally, the Kedem-Katchalsky matching condition at the IEL can be replaced by a constant flux condition to model a damaged IEL. We intend to investigate the effect of such diseased arterial wall configurations on optimal release kinetics of paclitaxel- and sirolimus-eluting stents and on optimal DES strut shapes in future simulations.

Chapter 4 did not include the strut shape optimization of fast-release paclitaxel-eluting stents (P-DES). Figure 5.1 depicts preliminary results on the optimal strut shape and the associated cost function scores for a P-DES with fast release kinetics. The computational model setup of this case assumed the endothelium to be denuded only in the stented portion of the vessel but intact otherwise. The optimal shape is elongated ($b_s = 82.5 \mu\text{m}$) and very thin ($a_s = 12.5 \mu\text{m}$) with a strut shape exponent of $n = 2.6$. The resulting partial scores are: $\bar{T}_m = 0.03$, $\bar{T}_e = 0.01$, $\bar{T}_e = 0.06$ and $J_{\text{FDI}} = 0.12$. If we compare these results to the slow-release P-DES strut design optimizations (Fig. 4.8 A and Fig. 4.9 A), we see immediately that the strut shape is much more streamlined (yielding a reduced J_{FDI}) and that this optimal strut height a_s corresponds to the low strut height a_s that was obtained for the setup with entirely denuded endothelium.

Since paclitaxel in this case is released within hours after stent implantation, the former strut height a_s restriction, which prevented prolonged exposure of the endothelial surface to

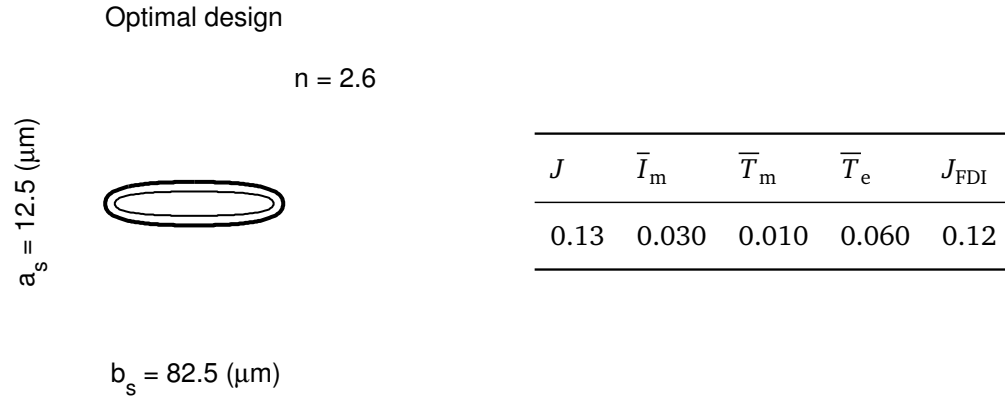


Figure 5.1: Optimal fast-release P-DES strut design for $d_c = 0.5$ and a model configuration that assumes the endothelium is denuded in the stented portion of the vessel but intact otherwise. The table provides the associated total cost function score J and its contributing partial scores \bar{I}_m , \bar{T}_m , \bar{T}_e , and J_{FDI} .

adverse concentrations, is no longer the dominant effect. Similarly, the advantage of a high strut shape exponent n on the inefficacy score obtained for slow-release DES is reduced and the flow-related objective dominates the final outcome of the optimization. We note at this point that these results are rather preliminary and require further analysis.

As mentioned in the discussion of Chapter 4, the idea of a DES with different shapes on the luminal and abluminal sides merits further investigation. The idea is that the fluid-dynamical considerations are the most relevant for the luminal side of the stent strut, while drug-related considerations are the most important on the abluminal side of the stent. The resulting strut shape could potentially yield an overall optimal design that is superior to any of the designs that we were able to identify in this dissertation. Such an optimization can be realized by choosing a different set of design variables in (Eq. (4.1)). This increases, however, the number of design variables and thus the run-time of the optimization.

Stent malapposition is a complication of stenting where some stent struts (typically at the end of a stent) are either poorly embedded in the arterial wall or even protrude entirely into the bloodstream [74, 93, 116]. Malapposition can arise either as an immediate result of the surgery or develop over time [126], a process that is not well understood and that is more prevalent with DES [36, 108]. This complication can be related to delayed endothelial recovery and late stent thrombosis [35]. It is thus of interest to investigate how malapposed stent struts affect the optimization of DES and if it might be possible to devise stent designs whose performance is to some degree insensitive to malapposition.

Throughout this thesis we assumed an idealized strut embedment of 50% and the sensitivity estimation of Chapter 4 showed (with the exception of P-DES with a top-coat, Fig. 4.5) no significant effect of the strut embedment p_{st} on the drug-related part of the cost function J_{ETH} in the range of 20 – 80% embedment. However, the flow-related part of the cost function J_{FDI} is more sensitive to strut embedment p_{st} than to any other parameter considered. One manner to further investigate this issue is to perform optimizations with a setup where the most distal stent strut is completely exposed to the bloodstream whereas the remaining stent struts are embedded normally.

Another useful configuration might be a setup where one strut is fully embedded, one is half embedded, and the last strut is not embedded. The endothelium would have to be denuded in this case to assure a homogeneous convection field in the arterial wall. Moreover, to investigate

the effect of fluid mechanical interactions among the struts on the optimization, the order of which struts are embedded and which are not needs to be varied. We performed preliminary studies (results not shown) investigating the fluid mechanics of unembedded stent struts. The results indicated that the flow disturbance index as defined in this dissertation (Eq. 4.5) might not be a sufficient indicator to quantify the severity of the flow disturbance of unembedded stent struts. Rather, the flow disturbance index should be extended to also account for the length of the flow recirculation zone downstream of the stent.

Last, to complete the investigation of sirolimus-eluting stents (S-DES), it is necessary to perform a drug release optimization where the therapeutic window of sirolimus spans the maximum possible range (from the low efficacy concentration threshold of paclitaxel $c_{\text{eff}} = 1 \cdot 10^{-5} \text{ mol cm}^{-3}$ to the high toxic concentration threshold of sirolimus $c_{\text{tox}} = 0.73 \text{ mol cm}^{-3}$). These results will clarify whether low-dose or high-dose S-DES yield an overall optimal drug delivery strategy.

5.1.2 Expanding the cost function

The second direction proposed as a follow-up to this work consists of resolving specific shortcomings of the cost function and extending its objectives. When we look at the contour plots of the cost function that are obtained for the drug release kinetics optimizations of Chapter 3, we can see that the optimal designs are often very close to non-optimal regions of the design space. We initially intended to alleviate this issue by introducing the homogeneity score \bar{H}_m . The contour plots also reveal that the non-optimal designs neighboring the optimal designs are non-optimal because of their endothelial toxicity score \bar{T}_e . One problem is that the homogeneity score \bar{H}_m only “buffers” the toxicity in the media and not at the endothelial surface. Thus, we suggest that future efforts add a homogeneity score of the endothelium to the cost function.

An important motivation for this work is the unresolved problem of late stent thrombosis. The cost function we have developed does not explicitly account for this issue. More specifically, there is no score in the present cost function that measures the risk of thrombosis for a particular stent design. Future models stand to benefit from adding such a term to the cost function. We currently do not have a concrete idea for what this metric should look like; however, there are at least two possibilities from which it could be derived. The first possibility is based on recent work [135] that has shown that fluid mechanical shear stress gradients can induce thrombosis independently of any biochemical considerations. Thus, a possible metric might be based on the magnitude of wall shear stress gradients.

The second possibility is to use numerical models similar to those described by [52, 65, 113] to simulate the formation and progression of thrombosis and to use these results to obtain a thrombosis score that can be added to the cost function. The thrombosis simulation could at first be performed independently from the drug transport simulation with subsequent coupling to model active thrombus growth. It is of course expected that the coupling will significantly increase simulation time.

A shortcoming of the stent strut shape optimization performed in Chapter 4 is that the size (in particular the strut width) of optimal designs is not feasible for clinical practice. This is due to the strong emphasis we have placed on optimizing drug transport from these struts. A possibility to alleviate this problem, mentioned in the discussion of Chapter 4, is to account for mechanical stresses in the stent as well as in the arterial wall in the cost function, which would potentially drive the strut designs to smaller struts. Motivated by the fact that stent struts should be small in order to minimize injury of the vessel wall at implantation [27, 48],

we also suggest including the notion of stent porosity ϵ_{stent} [111] in future versions of the cost function. This parameter measures the radially projected surface of the stent struts compared to the total radially projected surface of a stent, i.e. for a stent with total length l_s and a strut diameter d_s that is comprised of a series of n_s rings the porosity is calculated as:

$$\epsilon_{\text{stent}} = 1 - \frac{(n_s - 1) d_s}{l_s}. \quad (5.1)$$

5.1.3 Improved representation of the arterial wall

The two most restrictive simplifying assumptions of the computational model used in this thesis are steady flow conditions and a 2D axisymmetric geometry. Arterial geometry is three-dimensional and blood circulation is unsteady and both phenomena play an important role for stent design [100, 189]. We thus recommend extending the current computational model to 3D and investigating the effect of unsteady flow on the optimization results.

Last but not least, we showed in this dissertation how important drug transport kinetics are for the design of optimal DES and how crucial accurate modeling of the arterial wall is to correctly predicting drug transport. The computational model used in this work accounted for the media and the intima as two separate layers; however, the media itself has a layered substructure [136, 199] which can impact the transport of the drug. We thus suggest investigating yet more realistic models of the media [78, 103]. Given the difference of the arterial wall composition in different parts of the blood circulation, a more accurate and modular model of the arterial wall can pave the way for lesion-specific and location-specific DES optimization.

A.1 From the Brinkman equation to Darcy's Law

Fluid flow in the porous layers of the arterial wall can be described by the standard Darcy-Brinkman equation

$$\nabla p = -\frac{\mu_p}{P_D \text{Re}_0} \mathbf{u} + \frac{\mu_p^*}{\text{Re}_0} \Delta \mathbf{u} . \quad (\text{A.1})$$

An order-of-magnitude analysis on the Brinkman equation reveals that the viscous term only plays a significant role when $\tilde{L}^2 \sim \tilde{P}_D$. Thus, the effect of the viscous term is limited to a boundary layer which is an order of magnitude thinner than the endothelium. Consequently, for both layers the governing equation is simplified to Darcy's original formulation:

$$\nabla p = -\frac{\mu_p}{P_D \text{Re}_0} \mathbf{u} . \quad (\text{A.2})$$

A.2 Derivation of the weighted concentration

The local average fluid concentration $\bar{c}_{\alpha,j}$ as required by the Kedem-Katchalsky matching boundary conditions is calculated from the integral of the solution of the attributed differential equation for the concentration distribution in one dimension [106]:

$$\bar{c}_{\alpha,j} = \frac{c_{\alpha,j-1} e^{\text{Pe}_j^*} - c_{\alpha,j+1}}{e^{\text{Pe}_j^*} - 1} - \frac{c_{\alpha,j-1} - c_{\alpha,j+1}}{\text{Pe}_j^*} \quad (\text{A.3})$$

with

$$\text{Pe}_j^* = \frac{s_j J_{V,j}}{P_j} . \quad (\text{A.4})$$

Given strictly radial transport from domain $j-1$ to $j+1$, this expression allows an approximate evaluation of the average concentration in the respective "layer" j . When the exponential function is expanded to third order, it becomes obvious that this expression reflects the weighted average concentration of the layer:

$$\bar{c}_{\alpha,j} = \frac{1}{2} (c_{\alpha,j-1} + c_{\alpha,j+1}) + \frac{\text{Pe}_j^*}{12} (c_{\alpha,j-1} - c_{\alpha,j+1}) . \quad (\text{A.5})$$

A.3 Including reaction at the endothelial surface

Like smooth muscle cells, endothelial cells interact with the drugs eluted from the stent surface. Thus, we wish to include this interaction in the boundary condition at the endothelium via a concentration-dependent partition coefficient. The Kedem-Katchalsky equation is derived assuming steady state conditions [106]. Assuming $\frac{\partial b}{\partial t} = 0$ for the reaction equation (Eq. (2.10)) yields

$$b = \frac{c}{c + (f_{cb}B_p)^{-1}}. \quad (\text{A.6})$$

Reintroducing this expression into the transport equation of the arterial wall (Eq. (2.7)) leads to the concentration-dependent partition coefficient:

$$k_p(c) = \frac{1}{B_p^{-1} + 2f_{cb}c + B_p(f_{cb}c)^2}. \quad (\text{A.7})$$

Assuming an instantaneous reaction of the drug on the surface of ECs, the intrinsic fluid concentration used in the Kedem-Katchalsky equation is now:

$$c_{\alpha, e\pm 1} = \frac{c_{e\pm 1}}{\varepsilon_{e\pm 1} (k_p(c_{e\pm 1}) + 1)}. \quad (\text{A.8})$$

A.4 Governing equation for the equilibrium case

Assuming constant equilibrium between bound and free drug concentration (Eq. (2.9)), the governing equation (Eq. (2.7)) reduces to:

$$\frac{\partial c_{T,j}}{\partial t} + \frac{1}{\kappa} \nabla \left(\Lambda_j P e_0 \vec{u}_j c_{T,j} - \mathbf{D}_j \nabla c_{T,j} \right) = 0, \quad (\text{A.9})$$

where $c_{T,j}$ represents the total drug concentration, the sum of the free concentration c_j and the bound concentration b : $c_{T,j} = b + c_j = \kappa c_j$.

A.5 Remaining drug-dependent parameters of the model

Except for the lag coefficient Λ_j , we followed in our derivation of the remaining model parameters the description of [55]. The lag coefficient Λ_j of the convective transport term which results from averaging can be calculated as:

$$\Lambda_j = \frac{\gamma_j}{\varepsilon_j}. \quad (\text{A.10})$$

where $\gamma_j \leq 1$ is the hindrance coefficient (in layer j) accounting for the frictional loss occurring during the transport of the drug through porous media. By means of fiber matrix theory, Curry [39] initially derived an expression for the hindrance coefficient

$$\gamma_{f,j} = 1 - (1 - \Phi_{f,j})^2 = (2 - \Phi_{f,j}) \Phi_{f,j}, \quad (\text{A.11})$$

where the reduction coefficient is computed by

$$\Phi_{f,j} = \exp \left(- (1 - \varepsilon_{f,j}) \left(\frac{2\tilde{r}_{\text{mol}}}{\tilde{r}_f} + \frac{\tilde{r}_{\text{mol}}^2}{\tilde{r}_f^2} \right) \right). \quad (\text{A.12})$$

With a mean fiber radius of $\tilde{r}_f = 3.2$ nm [55], the values for the SES and media can be calculated.

A.6 Diffusivity of sirolimus

No experimental data on the diffusivity of sirolimus in blood or blood plasma is available to the authors. Approximating sirolimus and paclitaxel as spheres, we estimate the average radius of sirolimus rescaling the radius of paclitaxel as a function of the molecular weight:

$$\tilde{r}_{\text{mol}} = \left(\frac{3\tilde{M}}{4\pi\tilde{\rho}N_A} \right)^{\frac{1}{3}}, \quad (\text{A.13})$$

yielding

$$\tilde{r}_{\text{mol}}^{\text{SIR}} = \left(\frac{\tilde{M}_{\text{SIR}}}{\tilde{M}_{\text{PAX}}} \right)^{\frac{1}{3}} \tilde{r}_{\text{mol}}^{\text{PAX}} = 1.23 \cdot 10^{-9} \text{ m}. \quad (\text{A.14})$$

This result, combined with the Stokes-Einstein equation and the free plasma diffusivity of paclitaxel, then results in the adjusted diffusivity for sirolimus.

Bibliography

- [1] Abizaid A (2007) Sirolimus-eluting coronary stents: a review. *Vascular Health and Risk Management* 3(2):191–201
- [2] Abramson MA, Audet C (2006) Convergence of mesh adaptive direct search to second-order stationary points. *SIAM Journal on Optimization* 17(2):606–619
- [3] Acharya G, Park K (2006) Mechanisms of controlled drug release from drug-eluting stents. *Advanced Drug Delivery Reviews* 58(3):387–401
- [4] Ai L, Vafai K (2006) A coupling model for macromolecule transport in a stenosed arterial wall. *International Journal of Heat and Mass Transfer* 49(9-10):1568–1591
- [5] AIAA (1998) AIAA Guide for the Verification and Validation of Computational Fluid Dynamics Simulations. American Institute of Aeronautics & Astronautics
- [6] Alfonso F, Pérez-Vizcayno MJ (2013) Drug-eluting balloons for restenosis after stent implantation. *The Lancet* 381(9865):431–433
- [7] Aragon J, Kar S, Tio F, Trauthen B, Parisky A, Watanabe C, Jamali A, Eigler N, Serruys PW, Litvack F (2005) The effect of variable release kinetics on paclitaxel efficacy from a drug eluting stent in a porcine model. *EuroIntervention* 1(2):228–235
- [8] Asakura T, Karino T (1990) Flow patterns and spatial distribution of atherosclerotic lesions in human coronary arteries. *Circulation Research* 66(4):1045–1066
- [9] Atherton MA, Bates RA (2004) Robust optimization of cardiovascular stents: a comparison of methods. *Engineering Optimization* 36(2):207–217
- [10] Audet C, Dennis Jr JE (2007) Mesh adaptive direct search algorithms for constrained optimization. *SIAM Journal on optimization* 17(1):188–217
- [11] Balakrishnan B, Tzafiriri AR, Seifert P, Groothuis A, Rogers C, Edelman ER (2005) Strut position, blood flow, and drug deposition - implications for single and overlapping drug-eluting stents. *Circulation* 111(22):2958–2965
- [12] Balakrishnan B, Dooley JF, Kopia G, Edelman ER (2007) Intravascular drug release kinetics dictate arterial drug deposition, retention, and distribution. *Journal of Controlled Release* 123(2):100–108
- [13] Barakat A, Lieu D (2003) Differential responsiveness of vascular endothelial cells to different types of fluid mechanical shear stress. *Cell Biochemistry and Biophysics* 38(3):323–343

- [14] Barakat AI, Karino T, Colton CK (1997) Microcinematographic studies of flow patterns in the excised rabbit aorta and its major branches. *Biorheology* 34(3):195–221
- [15] Barakat AI, Leaver EV, Pappone PA, Davies PF (1999) A flow-activated chloride-selective membrane current in vascular endothelial cells. *Circulation Research* 85(9):820–828
- [16] Belitz P (2011) Applications on multi-dimensional sphere packings: Derivative-free optimization. PhD thesis, University of California at San Diego
- [17] Belitz P, Bewley T (2012) New horizons in sphere-packing theory, part II: lattice-based derivative-free optimization via global surrogates. *Journal of Global Optimization* pp 1–31
- [18] Berry JL, Santamarina A, Moore JE, Roychowdhury S, Routh WD (2000) Experimental and computational flow evaluation of coronary stents. *Annals of Biomedical Engineering* 28(4):386–398
- [19] van Beusekom HM, Saia F, Zindler JD, Lemos PA, Swager-ten Hoor SL, van Leeuwen MA, de Feijter PJ, Serruys PW, van der Giessen WJ (2007) Drug-eluting stents show delayed healing: paclitaxel more pronounced than sirolimus. *European Heart Journal* 28(8):974–979
- [20] Birkmeier KA, Kastrati A, Byrne RA, Holle H, Schulz S, Tiroch K, Kufner S, Massberg S, Laugwitz KL, Schömig A, Mehilli J (2011) Five-year clinical outcomes of sirolimus-eluting versus paclitaxel-eluting stents in high-risk patients. *Catheterization and Cardiovascular Interventions* 77(4):494–501
- [21] Bloom DA, Clayman RV, McDougal E (1999) Stents and related terms: a brief history. *Urology* 54(4):767–771
- [22] Boden WE, O'Rourke RA, Teo KK, Hartigan PM, Maron DJ, Kostuk WJ, Knudtson M, Dada M, Casperson P, Harris CL, Chaitman BR, Shaw L, Gosselin G, Nawaz S, Title LM, Gau G, Blaustein AS, Booth DC, Bates ER, Spertus JA, Berman DS, Mancini GJ, Weintraub WS (2007) Optimal medical therapy with or without PCI for stable coronary disease. *New England Journal of Medicine* 356(15):1503–1516
- [23] Booker AJ, Dennis JE, Frank PD, Serafini DB, Torczon V, Trosset MW (1999) A rigorous framework for optimization of expensive functions by surrogates. *Structural Optimization* 17(1):1–13
- [24] Borghi A, Foa E, Balossino R, Migliavacca F, Dubini G (2008) Modelling drug elution from stents: effects of reversible binding in the vascular wall and degradable polymeric matrix. *Computer Methods in Biomechanics and Biomedical Engineering* 11(4):367–377
- [25] Brent RP (1972) Algorithms for minimization without derivatives. Prentice-Hall series in automatic computation, Prentice-Hall
- [26] Buchanan GL, Basavarajaiah S, Chieffo A (2012) Stent thrombosis: Incidence, predictors and new technologies. *Thrombosis* 2012:1–12

- [27] Butany J, Carmichael K, Leong SW, Collins MJ (2005) Coronary artery stents: identification and evaluation. *Journal of Clinical Pathology* 58(8):795–804
- [28] Caro C (2009) Discovery of the role of wall shear in atherosclerosis. *Arteriosclerosis, Thrombosis, and Vascular Biology* 29(2):158–161
- [29] Caro CG, Fitz-Gerald JM, Schroter RC (1969) Arterial wall shear and distribution of early atheroma in man. *Nature* 223(5211):1159–1161
- [30] Caro CG, Fitz-Gerald JM, Schroter RC (1971) Atheroma and arterial wall shear. observation, correlation and proposal of a shear dependent mass transfer mechanism for atherogenesis. *Proceedings of the Royal Society of London Series B, Containing papers of a Biological character Royal Society (Great Britain)* 177(46):109–159
- [31] Charonko J, Karri S, Schmiegl J, Prabhu S, Vlachos P (2009) In vitro, time-resolved PIV comparison of the effect of stent design on wall shear stress. *Annals of Biomedical Engineering* 37(7):1310–1321
- [32] Chien S (2007) Mechanotransduction and endothelial cell homeostasis: the wisdom of the cell. *American Journal of Physiology - Heart and Circulatory Physiology* 292(3):H1209–H1224
- [33] Chiu JJ, Chien S (2011) Effects of disturbed flow on vascular endothelium: Pathophysiological basis and clinical perspectives. *Physiological Reviews* 91(1):327–387
- [34] Colombo A, Gerber RT (2008) Should dual antiplatelet therapy after drug-eluting stents be continued for more than 1 year?: Dual antiplatelet therapy after drug-eluting stents should not be continued for more than 1 year and preferably indefinitely. *Circulation: Cardiovascular Interventions* 1(3):226–232
- [35] Cook S, Wenaweser P, Togni M, Billinger M, Morger C, Seiler C, Vogel R, Hess O, Meier B, Windecker S (2007) Incomplete stent apposition and very late stent thrombosis after drug-eluting stent implantation. *Circulation* 115(18):2426–2434
- [36] Cook S, Eshtehardi P, Kalesan B, Räber L, Wenaweser P, Togni M, Moschovitis A, Vogel R, Seiler C, Eberli FR, Lüscher T, Meier B, Jüni P, Windecker S (2012) Impact of incomplete stent apposition on long-term clinical outcome after drug-eluting stent implantation. *European Heart Journal* 33(11):1334–1343
- [37] Cortese B, Sgueglia GA, Granada JF (2013) Paclitaxel coated balloons, the time for awareness has come. *International Journal of Cardiology* 164(1):1–2
- [38] Creel CJ, Lovich MA, Edelman ER (2000) Arterial paclitaxel distribution and deposition. *Circulation Research* 86(8):879–884
- [39] Curry FRE (1984) Mechanics and thermodynamics of transcapillary exchange. In: Renkin E, Michel C (eds) *The Cardiovascular System. Microcirculation*, no. 4 in *Handbook of Physiology*, American Physiological Society, pp 309–374

- [40] Daemen J, Wenaweser P, Tsuchida K, Abrecht L, Vaina S, Morger C, Kukreja N, Jüni P, Sianos G, Hellige G, van Domburg RT, Hess OM, Boersma E, Meier B, Windecker S, Serruys PW (2007) Early and late coronary stent thrombosis of sirolimus-eluting and paclitaxel-eluting stents in routine clinical practice: data from a large two-institutional cohort study. *The Lancet* 369(9562):667–678
- [41] Davies PF (1995) Flow-mediated endothelial mechanotransduction. *Physiological Reviews* 75(3):519–560
- [42] Davies PF (2009) Hemodynamic shear stress and the endothelium in cardiovascular pathophysiology. *Nature Clinical Practice Cardiovascular Medicine* 6(1):16–26
- [43] Dewey J C F, Bussolari SR, Gimbrone J M A, Davies PF (1981) The dynamic response of vascular endothelial cells to fluid shear stress. *Journal of Biomechanical Engineering* 103(3):177–185
- [44] Duraiswamy N, Schoephoerster RT, Moreno MR, Moore JE (2007) Stented artery flow patterns and their effects on the artery wall. *Annual Review of Fluid Mechanics* 39(1):357–382
- [45] Eskin S, Ives C, McIntire L, Navarro L (1984) Response of cultured endothelial cells to steady flow. *Microvascular Research* 28(1):87–94
- [46] Ezzati M, Vander Hoorn S, Lawes CM, Leach R, James WPT, Lopez AD, Rodgers A, Murray CJ (2005) Rethinking the “diseases of affluence” paradigm: global patterns of nutritional risks in relation to economic development. *PLoS Medicine* 2(5):e133
- [47] Falk E (2006) Pathogenesis of atherosclerosis. *Journal of the American College of Cardiology* 47(8s1):C7–C12
- [48] Farb A, Sangiorgi G, Carter AJ, Walley VM, Edwards WD, Schwartz RS, Virmani R (1999) Pathology of acute and chronic coronary stenting in humans. *Circulation* 99(1):44–52
- [49] Farb A, Heller PF, Shroff S, Cheng L, Kolodgie FD, Carter AJ, Scott DS, Froehlich J, Virmani R (2001) Pathological analysis of local delivery of paclitaxel via a polymer-coated stent. *Circulation* 104(4):473–479
- [50] Farhan S, Hemetsberger R, Matiasek J, Strehblow C, Pavo N, Khorsand A, Petneházy O, Petrásí Z, Kaider A, Glogar D, Huber K, Gyöngyösi M (2009) Implantation of paclitaxel-eluting stent impairs the vascular compliance of arteries in porcine coronary stenting model. *Atherosclerosis* 202(1):144–151
- [51] Feenstra PH, Taylor CA (2009) Drug transport in artery walls: A sequential porohyperelastic-transport approach. *Computer Methods in Biomechanics and Biomedical Engineering* 12(3):263–276
- [52] Filipovic N, Kojic M, Tsuda A (2008) Modelling thrombosis using dissipative particle dynamics method. *Philosophical Transactions of the Royal Society A: Mathematical, Physical and Engineering Sciences* 366(1879):3265–3279

- [53] Finn AV, Joner M, Nakazawa G, Kolodgie F, Newell J, John MC, Gold HK, Virmani R (2007) Pathological correlates of late drug-eluting stent thrombosis. *Circulation* 115(18):2435–2441
- [54] Finn AV, Nakazawa G, Joner M, Kolodgie FD, Mont EK, Gold HK, Virmani R (2007) Vascular responses to drug eluting stents: Importance of delayed healing. *Arteriosclerosis, Thrombosis, and Vascular Biology* 27(7):1500–1510
- [55] Formaggia L, Quarteroni A, Veneziani A (eds) (2009) *Cardiovascular Mathematics*. Springer Milan
- [56] Forrester AIJ, Sóbester A, Keane AJ (2008) *Engineering design via surrogate modelling a practical guide*. J. Wiley
- [57] Frey D, Billinger M, Meier P, Beslac O, Grossenbacher R, Hänni B, Hess OM (2008) Endothelialization of sirolimus-eluting stents with slow and extended drug release in the porcine overstretch model. *The Journal of Invasive Cardiology* 20(12):631–634
- [58] Fry DL (1968) Acute vascular endothelial changes associated with increased blood velocity gradients. *Circulation Research* 22(2):165–197
- [59] Fukuda D, Aikawa M (2010) Intimal smooth muscle cells: The context-dependent origin. *Circulation* 122(20):2005–2008
- [60] Garg S, Serruys PW (2010) Coronary stents: Current status. *Journal of the American College of Cardiology* 56(10, Supplement 1):S1–S42
- [61] Garg S, Serruys PW (2010) Coronary stents: Looking forward. *Journal of the American College of Cardiology* 56(10, Supplement 1):S43–S78
- [62] Garg S, Magro M, Serruys P (2011) 6.627 – drug-eluting stents. In: Ducheyne P (ed) *Comprehensive Biomaterials*, Elsevier, pp 427–448
- [63] Gielis J (2003) A generic geometric transformation that unifies a wide range of natural and abstract shapes. *American Journal of Botany* 90(3):333–338
- [64] Gojova A, Barakat AI (2005) Vascular endothelial wound closure under shear stress: role of membrane fluidity and flow-sensitive ion channels. *Journal of Applied Physiology* 98(6):2355–2362
- [65] Goodman PD, Barlow ET, Crapo PM, Mohammad SF, Solen KA (2005) Computational model of device-induced thrombosis and thromboembolism. *Annals of Biomedical Engineering* 33(6):780–797
- [66] Gray WA, Granada JF (2010) Drug-coated balloons for the prevention of vascular restenosis. *Circulation* 121(24):2672–2680
- [67] Grines CL, Bonow RO, Casey DE, Gardner TJ, Lockhart PB, Moliterno DJ, O’Gara P, Whitlow P (2007) Prevention of premature discontinuation of dual antiplatelet therapy in patients with coronary artery stents. *Circulation* 115(6):813–818

- [68] Guagliumi G, Ikejima H, Sirbu V, Bezerra H, Musumeci G, Lortkipanidze N, Fiocca L, Tahara S, Vassileva A, Matiashvili A, Valsecchi O, Costa M (2011) Impact of drug release kinetics on vascular response to different zotarolimus-eluting stents implanted in patients with long coronary stenoses: The LongOCT study (optical coherence tomography in long lesions). *JACC: Cardiovascular Interventions* 4(7):778–785
- [69] Guagliumi G, Sirbu V, Musumeci G, Gerber R, Biondi-Zoccai G, Ikejima H, Ladich E, Lortkipanidze N, Matiashvili A, Valsecchi O, Virmani R, Stone GW (2012) Examination of the in vivo mechanisms of late drug-eluting stent thrombosis: Findings from optical coherence tomography and intravascular ultrasound imaging. *JACC: Cardiovascular Interventions* 5(1):12–20
- [70] Gundert TJ, Marsden AL, Yang W, John F LaDisa J (2012) Optimization of cardiovascular stent design using computational fluid dynamics. *Journal of Biomechanical Engineering* 134(1):011,002
- [71] Gundert TJ, Marsden AL, Yang W, Marks DS, LaDisa J (2012) Identification of hemodynamically optimal coronary stent designs based on vessel caliber. *IEEE Transactions on Biomedical Engineering* 59(7):1992–2002
- [72] Hahn C, Schwartz MA (2009) Mechanotransduction in vascular physiology and atherogenesis. *Nature Reviews Molecular Cell Biology* 10(1):53–62
- [73] Hara H, Nakamura M, Palmaz JC, Schwartz RS (2006) Role of stent design and coatings on restenosis and thrombosis. *Advanced Drug Delivery Reviews* 58(3):377–386
- [74] Hassan AK, Bergheanu SC, Stijnen T, van der Hoeven BL, Snoep JD, Plevier JW, Schali J MJ, Wouter Jukema J (2010) Late stent malapposition risk is higher after drug-eluting stent compared with bare-metal stent implantation and associates with late stent thrombosis. *European Heart Journal* 31(10):1172–1180
- [75] Helmlinger G, Geiger RV, Schreck S, Nerem RM (1991) Effects of pulsatile flow on cultured vascular endothelial cell morphology. *Journal of Biomechanical Engineering* 113(2):123–131
- [76] Hilder T, Hill J (2008) Probability of encapsulation of paclitaxel and doxorubicin into carbon nanotubes. *Micro & Nano Letters* 3(2):41–49
- [77] Hindmarsh AC, Brown PN (2005) SUNDIALS: suite of nonlinear and Differential/Algebraic equation solvers
- [78] Hollander Y, Durban D, Lu X, Kassab GS, Lanir Y (2011) Experimentally validated micro structural 3D constitutive model of coronary arterial media. *Journal of Biomechanical Engineering* 133(3):031,007
- [79] Huang Y, Rumschitzki D, Chien S, Weinbaum S (1994) A fiber matrix model for the growth of macromolecular leakage spots in the arterial intima. *Journal of Biomechanical Engineering* 116(4):430–445
- [80] Hwang CW, Edelman ER (2002) Arterial ultrastructure influences transport of locally delivered drugs. *Circulation Research* 90(7):826–832

- [81] Hwang CW, Wu D, Edelman ER (2001) Physiological transport forces govern drug distribution for stent-based delivery. *Circulation* 104(5):600–605
- [82] Hwang CW, Wu D, Edelman ER (2003) Impact of transport and drug properties on the local pharmacology of drug-eluting stents. *Acute Cardiac Care* 5(1):7–12
- [83] Inoue K (2012) Pathological perspective of drug-eluting stent thrombosis. *Thrombosis* 2012:1–8
- [84] Joner M, Finn AV, Farb A, Mont EK, Kolodgie FD, Ladich E, Kutys R, Skorija K, Gold HK, Virmani R (2006) Pathology of drug-eluting stents in humans: Delayed healing and late thrombotic risk. *Journal of the American College of Cardiology* 48(1):193–202
- [85] Joner M, Nakazawa G, Finn AV, Quee SC, Coleman L, Acampado E, Wilson PS, Skorija K, Cheng Q, Xu X, Gold HK, Kolodgie FD, Virmani R (2008) Endothelial cell recovery between comparator polymer-based drug-eluting stents. *Journal of the American College of Cardiology* 52(5):333–342
- [86] Jones DR (2001) A taxonomy of global optimization methods based on response surfaces. *Journal of Global Optimization* 21(4):345–383
- [87] Kamath KR, Barry JJ, Miller KM (2006) The taxus(TM) drug-eluting stent: A new paradigm in controlled drug delivery. *Advanced Drug Delivery Reviews* 58(3):412–436
- [88] Kandzari DE, Angiolillo DJ, Price MJ, Teirstein PS (2009) Identifying the “Optimal” duration of dual antiplatelet therapy after drug-eluting stent revascularization. *JACC: Cardiovascular Interventions* 2(12):1279–1285
- [89] Karner G, Perktold K, Zehentner HP (2001) Computational modeling of macromolecule transport in the arterial wall. *Computer Methods in Biomechanics and Biomedical Engineering* 4(6):491–504
- [90] Kaul U, Mansoor AH (2012) Choice of drug-eluting stent – evidence-based or empirical. *Journal of Indian College of Cardiology* 2(1):22–28
- [91] Kedem O, Katchalsky A (1958) Thermodynamic analysis of the permeability of biological membranes to non-electrolytes. *Biochimica et Biophysica Acta* 27:229–246
- [92] Khakpour M, Vafai K (2008) A comprehensive analytical solution of macromolecular transport within an artery. *International Journal of Heat and Mass Transfer* 51(11-12):2905–2913
- [93] Kim BK, Hong MK, Shin DH, Kim JS, Ko YG, Choi D, Jang Y (2012) Relationship between stent malapposition and incomplete neointimal coverage after drug-eluting stent implantation. *Journal of Interventional Cardiology* 25(3):270–277
- [94] Klugherz BD, Llanos G, Lieuallen W, Kopia GA, Papandreou G, Narayan P, Sasseen B, Adelman SJ, Falotico R, Wilensky RL (2002) Twenty-eight-day efficacy and pharmacokinetics of the sirolimus-eluting stent. *Coronary Artery Disease* 13(3):183–188, PMID: 12131023

- [95] Kolda TG, Lewis RM, Torczon V (2003) Optimization by direct search: New perspectives on some classical and modern methods. *SIAM Review* 45(3):385–482
- [96] Koskinas KC, Chatzizisis YS, Antoniadis AP, Giannoglou GD (2012) Role of endothelial shear stress in stent restenosis and thrombosis: Pathophysiologic mechanisms and implications for clinical translation. *Journal of the American College of Cardiology* 59(15):1337–1349
- [97] Krige D (1951) A statistical approach to some basic mine valuation problems on the witwatersrand. *Journal of the Chemical, Metallurgical and Mining Society of South Africa* 52(6):119–139
- [98] Ku DN, Giddens DP, Zarins CK, Glagov S (1985) Pulsatile flow and atherosclerosis in the human carotid bifurcation. positive correlation between plaque location and low oscillating shear stress. *Arteriosclerosis, Thrombosis, and Vascular Biology* 5(3):293–302
- [99] LaDisa JF (2004) Stent design properties and deployment ratio influence indexes of wall shear stress: a three-dimensional computational fluid dynamics investigation within a normal artery. *Journal of Applied Physiology* 97(1):424–430
- [100] LaDisa JF, Olson LE, Hettrick DA, Warltier DC, Kersten JR, Pagel PS (2005) Axial stent strut angle influences wall shear stress after stent implantation: analysis using 3D computational fluid dynamics models of stent foreshortening. *BioMedical Engineering OnLine* 4:59
- [101] Lally C, Kelly DJ, Prendergast PJ (2006) Stents. *Wiley Encyclopedia of Biomedical Engineering*
- [102] Lao LL, Venkatraman SS (2008) Adjustable paclitaxel release kinetics and its efficacy to inhibit smooth muscle cells proliferation. *Journal of Controlled Release* 130(1):9–14
- [103] Lee K, Saidel GM, Penn MS (2005) Macromolecular transport in the arterial wall: alternative models for estimating barriers. *Annals of Biomedical Engineering* 33(11):1491–1503
- [104] Lei L, Guo SR, Chen WL, Rong HJ, Lu F (2011) Stents as a platform for drug delivery. *Expert Opinion on Drug Delivery* 8(6):813–831
- [105] Levin AD, Vukmirovic N, Hwang CW, Edelman ER (2004) Specific binding to intracellular proteins determines arterial transport properties for rapamycin and paclitaxel. *Proceedings of the National Academy of Sciences of the United States of America* 101(25):9463–9467
- [106] Levitt DG (1975) General continuum analysis of transport through pores: I. proof of Onsager's reciprocity postulate for uniform pore. *Biophysical Journal* 15(6):533–551
- [107] Li H, Zhang Lj, Chen Bh, Zhou X, Su K, Shi Wt, Wu Jz, Yu H, Wei L (2010) Inhibitory effect of paclitaxel on endothelial cell adhesion and migration. *Pharmacology* 85(3):136–145

- [108] Li S, Wang Y, Gai L, Yang T, Liu H, Wang Z, Bai Q, Xu X, Chen Y (2013) Evaluation of neointimal coverage and apposition with various drug-eluting stents over 12 months after implantation by optical coherence tomography. *International Journal of Cardiology* 162(3):166–171
- [109] Libby P (2002) Inflammation in atherosclerosis. *Nature* 420(6917):868–874
- [110] Libby P, Ridker PM, Hansson GK (2011) Progress and challenges in translating the biology of atherosclerosis. *Nature* 473(7347):317–325
- [111] Liou TM, Li YC (2008) Effects of stent porosity on hemodynamics in a sidewall aneurysm model. *Journal of Biomechanics* 41(6):1174–1183
- [112] Liuzzo JP, Ambrose JA, Coppola JT (2005) Sirolimus- and taxol-eluting stents differ towards intimal hyperplasia and re-endothelialization. *The Journal of Invasive Cardiology* 17(9):497–502
- [113] Longest PW, Kleinstreuer C (2003) Comparison of blood particle deposition models for non-parallel flow domains. *Journal of Biomechanics* 36(3):421–430
- [114] Lovich MA, Creel C, Hong K, Hwang CW, Edelman ER (2001) Carrier proteins determine local pharmacokinetics and arterial distribution of paclitaxel. *Journal of Pharmaceutical Sciences* 90(9):1324–1335
- [115] Lum RM, Wiley LM, Barakat AI (2000) Influence of different forms of fluid shear stress on vascular endothelial TGF-beta1 mRNA expression. *International Journal of Molecular Medicine* 5(6):635–641
- [116] Lüscher TF, Steffel J, Eberli FR, Joner M, Nakazawa G, Tanner FC, Virmani R (2007) Drug-eluting stent and coronary thrombosis: Biological mechanisms and clinical implications. *Circulation* 115(8):1051–1058
- [117] Lusis AJ (2000) Atherosclerosis. *Nature* 407(6801):233–241
- [118] Marsden AL, Wang M, Dennis JE, Moin P (2004) Optimal aeroacoustic shape design using the surrogate management framework. *Optimization and Engineering* 5(2):235–262
- [119] Marsden AL, Wang M, Dennis JE, Moin P (2007) Trailing-edge noise reduction using derivative-free optimization and large-eddy simulation. *Journal of Fluid Mechanics* 572:13
- [120] Marsden AL, Feinstein JA, Taylor CA (2008) A computational framework for derivative-free optimization of cardiovascular geometries. *Computer Methods in Applied Mechanics and Engineering* 197(21-24):1890–1905
- [121] Marx SO, Totary-Jain H, Marks AR (2011) Vascular smooth muscle cell proliferation in restenosis. *Circulation: Cardiovascular Interventions* 4(1):104–111
- [122] Matheron G (1963) Principles of geostatistics. *Economic Geology* 58(8):1246–1266

- [123] Matter CM, Rozenberg I, Jaschko A, Greutert H, Kurz DJ, Wnendt S, Kuttler B, Joch H, Grünenfelder J, Zünd G, Tanner FC, Lüscher TF (2006) Effects of tacrolimus or sirolimus on proliferation of vascular smooth muscle and endothelial cells. *Journal of Cardiovascular Pharmacology* 48(6):286–292
- [124] McGinty S, McKee S, Wadsworth RM, McCormick C (2011) Modelling drug-eluting stents. *Mathematical Medicine and Biology* 28(1):1–29
- [125] Migliavacca F, Gervaso F, Prosi M, Zunino P, Minisini S, Formaggia L, Dubini G (2007) Expansion and drug elution model of a coronary stent. *Computer Methods in Biomechanics and Biomedical Engineering* 10(1):63–73
- [126] Mintz GS (2007) What to do about late incomplete stent apposition? *Circulation* 115(18):2379–2381
- [127] Mongrain R, Brunette J, Faik I, Bulman-Feleming N, Nguyen T (2005) Numerical modeling of coronary drug eluting stents. In: Suri J (ed) *Plaque imaging : pixel to molecular level*, IOS Press, pp 443–458
- [128] Mongrain R, Faik I, Leask RL, Rodes-Cabau J, Larose E, Bertrand OF (2007) Effects of diffusion coefficients and struts apposition using numerical simulations for drug eluting coronary stents. *Journal of Biomechanical Engineering* 129(5):733–742
- [129] Morris MD (1991) Factorial sampling plans for preliminary computational experiments. *Technometrics* 33(2):161–174
- [130] Mueller RL, Sanborn TA (1995) The history of interventional cardiology: cardiac catheterization, angioplasty, and related interventions. *American Heart Journal* 129(1):146–172
- [131] Nakazawa G, Vorpahl M, Finn AV, Narula J, Virmani R (2009) One step forward and two steps back with drug-eluting-stents: From preventing restenosis to causing late thrombosis and nouveau atherosclerosis. *JACC: Cardiovascular Imaging* 2(5):625–628
- [132] Nakazawa G, Nakano M, Otsuka F, Wilcox JN, Melder R, Pruitt S, Kolodgie FD, Virmani R (2011) Evaluation of polymer-based comparator drug-eluting stents using a rabbit model of iliac artery atherosclerosis / clinical perspective. *Circulation: Cardiovascular Interventions* 4(1):38–46
- [133] Nerem RM (1992) Vascular fluid mechanics, the arterial wall, and atherosclerosis. *Journal of Biomechanical Engineering* 114(3):274–282
- [134] Nerem RM, Levesque MJ, Cornhill JF (1981) Vascular endothelial morphology as an indicator of the pattern of blood flow. *Journal of Biomechanical Engineering* 103(3):172–176
- [135] Nesbitt WS, Westein E, Tovar-Lopez FJ, Tolouei E, Mitchell A, Fu J, Carberry J, Fouras A, Jackson SP (2009) A shear gradient-dependent platelet aggregation mechanism drives thrombus formation. *Nature Medicine* 15(6):665–673

- [136] O'Connell MK, Murthy S, Phan S, Xu C, Buchanan J, Spilker R, Dalman RL, Zarins CK, Denk W, Taylor CA (2008) The three-dimensional micro- and nanostructure of the aortic medial lamellar unit measured using 3D confocal and electron microscopy imaging. *Matrix Biology* 27(3):171–181
- [137] Ormiston JA, Serruys PW (2009) Bioabsorbable coronary stents. *Circulation: Cardiovascular Interventions* 2(3):255–260
- [138] Pan CJ, Tang JJ, Weng YJ, Wang J, Huang N (2009) Preparation and in vitro release profiles of drug-eluting controlled biodegradable polymer coating stents. *Colloids and Surfaces B: Biointerfaces* 73(2):199–206
- [139] Pant S, Bressloff NW, Forrester AIJ, Curzen N (2010) The influence of strut-connectors in stented vessels: a comparison of pulsatile flow through five coronary stents. *Annals of Biomedical Engineering* 38(5):1893–1907
- [140] Pant S, Limbert G, Curzen N, Bressloff N (2011) Multiobjective design optimisation of coronary stents. *Biomaterials* 32(31):7755–7773
- [141] Pant S, Bressloff N, Limbert G (2012) Geometry parameterization and multidisciplinary constrained optimization of coronary stents. *Biomechanics and Modeling in Mechanobiology* 11(1):61–82
- [142] Papafaklis MI, Chatzizisis YS, Naka KK, Giannoglou GD, Michalis LK (2012) Drug-eluting stent restenosis: Effect of drug type, release kinetics, hemodynamics and coating strategy. *Pharmacology & Therapeutics* 134(1):43–53
- [143] Park SJ, Park DW, Kim YH, Kang SJ, Lee SW, Lee CW, Han KH, Park SW, Yun SC, Lee SG, Rha SW, Seong IW, Jeong MH, Hur SH, Lee NH, Yoon J, Yang JY, Lee BK, Choi YJ, Chung WS, Lim DS, Cheong SS, Kim KS, Chae JK, Nah DY, Jeon DS, Seung KB, Jang JS, Park HS, Lee K (2010) Duration of dual antiplatelet therapy after implantation of drug-eluting stents. *New England Journal of Medicine* 362(15):1374–1382
- [144] Pendyala LK, Yin X, Li J, Chen JP, Chronos N, Hou D (2009) The first-generation drug-eluting stents and coronary endothelial dysfunction. *JACC: Cardiovascular Interventions* 2(12):1169–1177
- [145] Petersen JL, Barron JJ, Hammill BG, Cziraky MJ, Anstrom KJ, Wahl PM, Eisenstein EL, Krucoff MW, Califf RM, Schulman KA, Curtis LH (2010) Clopidogrel use and clinical events after drug-eluting stent implantation: Findings from the HealthCore integrated research database. *American Heart Journal* 159(3):462–470.e1
- [146] Pontrelli G, de Monte F (2010) A multi-layer porous wall model for coronary drug-eluting stents. *International Journal of Heat and Mass Transfer* 53(19-20):3629–3637
- [147] Poon M, Marx SO, Gallo R, Badimon JJ, Taubman MB, Marks AR (1996) Rapamycin inhibits vascular smooth muscle cell migration. *Journal of Clinical Investigation* 98(10):2277–2283

- [148] Prosi M, Zunino P, Perktold K, Quarteroni A (2005) Mathematical and numerical models for transfer of low-density lipoproteins through the arterial walls: a new methodology for the model set up with applications to the study of disturbed luminal flow. *Journal of Biomechanics* 38(4):903–917
- [149] Quosdorf D, Brede M, Leder A, Lootz D, Martin H, Schmitz KP (2011) Micro-particle-image-velocimetry zur bestimmung der geschwindigkeiten in einem koronargefäß mit stent. *tm - Technisches Messen* 78(5):239–245
- [150] R EE, Rogers C (1998) Pathobiologic responses to stenting. *The American Journal of Cardiology* 81(7, Supplement 1):4E–6E
- [151] Räber L, Wohlwend L, Wigger M, Togni M, Wandel S, Wenaweser P, Cook S, Moschovitis A, Vogel R, Kalesan B, Seiler C, Eberli F, Lüscher TF, Meier B, Jüni P, Windecker S (2011) Five-year clinical and angiographic outcomes of a randomized comparison of sirolimus-eluting and paclitaxel-eluting stents / clinical perspective. *Circulation* 123(24):2819–2828
- [152] Radeleff B, Lopez-Benitez R, Stampfl U, Stampfl S, Sommer C, Thierjung H, Berger I, Kauffmann G, Richter GM (2010) Paclitaxel-induced arterial wall toxicity and inflammation: Tissue uptake in various dose densities in a minipig model. *Journal of Vascular and Interventional Radiology* 21(8):1262–1270
- [153] Rao SS (2009) *Engineering optimization: theory and praxis*. Wiley
- [154] Ruygrok PN, Serruys PW (1996) Intracoronary stenting: From concept to custom. *Circulation* 94(5):882–890
- [155] Sacks J, Welch WJ, Mitchell TJ, Wynn HP (1989) Design and analysis of computer experiments. *Statistical Science* 4(4):409–423
- [156] Sakai S, Mizuno K, Yokoyama S, Tanabe J, Shinada T, Seimiya K, Takano M, Ohba T, Tomimura M, Uemura R, Imaizumi T (2003) Morphologic changes in infarct-related plaque after coronary stent placement: A serial angiography study. *Journal of the American College of Cardiology* 42(9):1558–1565
- [157] Sarno G, Lagerqvist B, Fröbert O, Nilsson J, Olivecrona G, Omerovic E, Saleh N, Venetanos D, James S (2012) Lower risk of stent thrombosis and restenosis with unrestricted use of ‘new-generation’ drug-eluting stents: a report from the nationwide swedish coronary angiography and angioplasty registry (SCAAR). *European Heart Journal* 33(5):606–613
- [158] Scheller B, Hehrlein C, Bocksch W, Rutsch W, Haghi D, Dietz U, Böhm M, Speck U (2006) Treatment of coronary in-stent restenosis with a paclitaxel-coated balloon catheter. *New England Journal of Medicine* 355(20):2113–2124
- [159] Schwartz CJ, Mitchell JR (1962) Observations on localization of arterial plaques. *Circulation Research* 11:63–73
- [160] Schwartz CJ, Valente AJ, Sprague EA, Kelley JL, Nerem RM (1991) The pathogenesis of atherosclerosis: an overview. *Clinical Cardiology* 14(S1):1–16

- [161] Schwartz SM, deBlois D, O'Brien ERM (1995) The intima: Soil for atherosclerosis and restenosis. *Circulation Research* 77(3):445–465
- [162] Seo T, Barakat AI (2009) The assessment of the performance of drug-eluting stent using computational fluid dynamics. *Korea-Australia Rheology Journal* 21(4):281–288
- [163] Seo T, Schachter LG, Barakat AI (2005) Computational study of fluid mechanical disturbance induced by endovascular stents. *Annals of Biomedical Engineering* 33(4):444–456
- [164] Serruys P (2002) *Handbook of coronary stents*, 4th edn. Taylor & Francis
- [165] Serruys PW, Sianos G, Abizaid A, Aoki J, den Heijer P, Bonnier H, Smits P, McClean D, Verheye S, Belardi J, Condado J, Pieper M, Gambone L, Bressers M, Symons J, Sousa E, Litvack F (2005) The effect of variable dose and release kinetics on neointimal hyperplasia using a novel paclitaxel-eluting stent platform: The paclitaxel in-stent controlled elution study (PISCES). *Journal of the American College of Cardiology* 46(2):253–260
- [166] Sibson R (1981) A brief description of natural neighbor interpolation (chapter 2). In: Barnett V (ed) *Interpreting multivariate data*, Wiley series in probability and mathematical statistics, Wiley, pp 21–36
- [167] Singh T, Cuomo L, Cohen M, Ahmad H, Aronow W (2013) Use of antiplatelet therapy after percutaneous coronary intervention with bare-metal stents and different types of drug-eluting stents. *Current Clinical Pharmacology* 8(1):59–66
- [168] Smits PC, Kedhi E, Roayaards KJ, Joesoef KS, Wassing J, Rademaker-Havinga TA, McFadden E (2011) 2-year follow-up of a randomized controlled trial of everolimus- and paclitaxel-eluting stents for coronary revascularization in daily practice. *Journal of the American College of Cardiology* 58(1):11–18
- [169] Spain DM (1966) Atherosclerosis. *Scientific American* 215(2):48–56
- [170] Spaulding C, Daemen J, Boersma E, Cutlip DE, Serruys PW (2007) A pooled analysis of data comparing sirolimus-eluting stents with bare-metal stents. *New England Journal of Medicine* 356(10):989–997
- [171] Srinivas K, Nakayama T, Ohta M, Obayashi S, Yamaguchi T (2008) Studies on design optimization of coronary stents. *Journal of Medical Devices* 2(1):011,004
- [172] Steigerwald K, Ballke S, Quee SC, Byrne RA, Vorpahl M, Vogeser M, Kolodgie F, Virmani R, Joner M (2012) Vascular healing in drug-eluting stents: differential drug-associated response of limus-eluting stents in a preclinical model of stent implantation. *EuroIntervention* 8(6):752–759
- [173] Stone GW, Moses JW, Ellis SG, Schofer J, Dawkins KD, Morice MC, Colombo A, Schampert E, Grube E, Kirtane AJ, Cutlip DE, Fahy M, Pocock SJ, Mehran R, Leon MB (2007) Safety and efficacy of sirolimus- and paclitaxel-eluting coronary stents. *New England Journal of Medicine* 356(10):998–1008

- [174] Stone GW, Rizvi A, Sudhir K, Newman W, Applegate RJ, Cannon LA, Maddux JT, Cutlip DE, Simonton CA, Sood P, Kereiakes DJ (2011) Randomized comparison of everolimus- and paclitaxel-eluting stents 2-year follow-up from the SPIRIT (clinical evaluation of the XIENCE v everolimus eluting coronary stent system) IV trial. *Journal of the American College of Cardiology* 58(1):19–25
- [175] Tesfamariam B (2008) Drug release kinetics from stent device-based delivery systems. *Journal of Cardiovascular Pharmacology* 51(2):118–125
- [176] Thompson RC, Allam AH, Lombardi GP, Wann LS, Sutherland ML, Sutherland JD, Soliman MAT, Frohlich B, Mininberg DT, Monge JM, Vallodolid CM, Cox SL, Abd el Maksoud G, Badr I, Miyamoto MI, el-Halim Nur el din A, Narula J, Finch CE, Thomas GS (2013) Atherosclerosis across 4000 years of human history: the horus study of four ancient populations. *The Lancet* 381(9873):1211–1222
- [177] Thomson JJ (1904) On the structure of the atom: an investigation of the stability and periods of oscillation of a number of corpuscles arranged at equal intervals around the circumference of a circle; with application of the results to the theory of atomic structure. *Philosophical Magazine Series 6* 7(39):237–265
- [178] Timmins L, Moreno M, Meyer C, Criscione J, Rachev A, Moore JE (2007) Stented artery biomechanics and device design optimization. *Medical and Biological Engineering and Computing* 45(5):505–513
- [179] Tzafiriri AR, Levin AD, Edelman ER (2009) Diffusion-limited binding explains binary dose response for local arterial and tumour drug delivery. *Cell Proliferation* 42(3):348–363
- [180] Tzafiriri AR, Vukmirovic N, Kolachalama VB, Astafieva I, Edelman ER (2010) Lesion complexity determines arterial drug distribution after local drug delivery. *Journal of Controlled Release* 142(3):332–338
- [181] Tzafiriri AR, Groothuis A, Price GS, Edelman ER (2012) Stent elution rate determines drug deposition and receptor-mediated effects. *Journal of Controlled Release* 161(3):918–926
- [182] Ueda Y, Nanto S, Komamura K, Kodama K (1994) Neointimal coverage of stents in human coronary arteries observed by angioscopy. *Journal of the American College of Cardiology* 23(2):341–346
- [183] Vairo G, Cioffi M, Cottone R, Dubini G, Migliavacca F (2010) Drug release from coronary eluting stents: A multidomain approach. *Journal of Biomechanics* 43(8):1580–1589
- [184] Valgimigli M, Campo G, Monti M, Vranckx P, Percoco G, Tumscitz C, Castriota F, Colombo F, Tebaldi M, Fucà G, Kubbajeh M, Cangiano E, Minarelli M, Scalone A, Cavazza C, Frangione A, Borghesi M, Marchesini J, Parrinello G, Ferrari R (2012) Short- versus long-term duration of dual-antiplatelet therapy after coronary stenting: A randomized multicenter trial. *Circulation* 125(16):2015–2026
- [185] Venkatraman S, Boey F (2007) Release profiles in drug-eluting stents: Issues and uncertainties. *Journal of Controlled Release* 120(3):149–160

- [186] Vergara C, Zunino P (2008) Multiscale boundary conditions for drug release from cardiovascular stents. *Multiscale Modeling & Simulation* 7(2):565–588
- [187] Wang XT, Venkatraman S, Boey F, Loo SC, Tan LP (2007) Effects of controlled-released sirolimus from polymer matrices on human coronary artery smooth muscle cells. *Journal of Biomaterials Science, Polymer Edition* 18(11):1401–1414
- [188] Weinbaum S, Tzeghai G, Ganatos P, Pfeffer R, Chien S (1985) Effect of cell turnover and leaky junctions on arterial macromolecular transport. *American Journal of Physiology – Heart and Circulatory Physiology* 248(6):H945–H960
- [189] Wentzel JJ, Whelan DM, Giessen WJvd, Beusekom HMMv, Andhyiswara I, Serruys PW, Slager CJ, Krams R (2000) Coronary stent implantation changes 3-d vessel geometry and 3-d shear stress distribution. *Journal of Biomechanics* 33(10):1287–1295
- [190] Wessely R, Schomig A, Kastrati A (2006) Sirolimus and paclitaxel on polymer-based drug-eluting stents: Similar but different. *Journal of the American College of Cardiology* 47(4):708–714
- [191] Wessely R, Blaich B, Belaiba RS, Merl S, Görlach A, Kastrati A, Schömig A (2007) Comparative characterization of cellular and molecular anti-restenotic profiles of paclitaxel and sirolimus. implications for local drug delivery. *Thrombosis and Haemostasis* 97(6):1003–1012
- [192] Whitaker S (1986) Transient diffusion, adsorption and reaction in porous catalysts: The reaction controlled, quasi-steady catalytic surface. *Chemical Engineering Science* 41(12):3015–3022
- [193] Whitaker S (2010) *The Method of Volume Averaging*. Kluwer Academic Publishers
- [194] Witzendichler B (2012) Dual antiplatelet therapy after drug-eluting stent implantation. *Journal of the American College of Cardiology* 60(15):1349–1351
- [195] World Health Organisation (2008) WHO | the top 10 causes of death. <http://who.int/mediacentre/factsheets/fs310/en/> Accessed: 2013-04-06
- [196] Wu W, Petrini L, Gastaldi D, Villa T, Vedani M, Lesma E, Previtali B, Migliavacca F (2010) Finite element shape optimization for biodegradable magnesium alloy stents. *Annals of Biomedical Engineering* 38(9):2829–2840
- [197] Yang N, Vafai K (2006) Modeling of low-density lipoprotein (LDL) transport in the artery—effects of hypertension. *International Journal of Heat and Mass Transfer* 49(5-6):850–867
- [198] Yang W, Feinstein JA, Marsden AL (2010) Constrained optimization of an idealized y-shaped baffle for the fontan surgery at rest and exercise. *Computer Methods in Applied Mechanics and Engineering* 199(33-36):2135–2149
- [199] Zoumi A, Lu X, Kassab GS, Tromberg BJ (2004) Imaging coronary artery microstructure using second-harmonic and two-photon fluorescence microscopy. *Biophysical Journal* 87(4):2778–2786

- [200] Zunino P (2004) Multidimensional pharmacokinetic models applied to the design of drug-eluting stents. *Cardiovascular Engineering* 4(2):181–191
- [201] Zunino P, D'Angelo C, Petrini L, Vergara C, Capelli C, Migliavacca F (2009) Numerical simulation of drug eluting coronary stents: Mechanics, fluid dynamics and drug release. *Computer Methods in Applied Mechanics and Engineering* 198(45-46):3633–3644